Pontifícia Universidade Católica
do Rio de Janeiro

Julio Acosta Rams

Electromagnetic Wave Propagation in Biaxially Anisotropic Media with Azimuthal Symmetry for Modeling Wireless Telemetry in Deep Oil Well

Dissertação de Mestrado

Dissertation presented to the Programa de Pós–graduação em Engenharia Elétrica da PUC-Rio in partial fulfillment of the requirements for the degree of Mestre em Engenharia Elétrica.

Advisor : Prof. Gláucio Lima Siqueira
Co-advisor: Prof. Guilherme Simon da Rosa

Rio de Janeiro
July 2019

Pontifícia Universidade Católica
do Rio de Janeiro

Julio Acosta Rams

Electromagnetic Wave Propagation in Biaxially Anisotropic Media with Azimuthal Symmetry for Modeling Wireless Telemetry in Deep Oil Well

Dissertation presented to the Programa de Pós–graduação em Engenharia Elétrica da PUC-Rio in partial fulfillment of the requirements for the degree of Mestre em Engenharia Elétrica. Approved by the Examination Committee.

Prof. Guilherme Simon da Rosa
Co-advisor
Departamento de Engenharia Elétrica – PUC-Rio

Prof. José Ricardo Bergmann
Centro de Estudos em Telecomunicações – PUC-Rio

Prof. Flavio José Vieira Hasselmann
Centro de Estudos em Telecomunicações – PUC-Rio

Prof.ª Leni Joaquim de Matos
UFF

Rio de Janeiro, July 16th, 2019

Julio Acosta Rams

Received the B.S degree in Telecommunications and Electronic Engineering from the Technology University of Havana "Jose A. Echeverria", Cuba, in 2016.

Bibliographic data

Acosta Rams, Julio

Electromagnetic Wave Propagation in Biaxially Anisotropic Media with Azimuthal Symmetry for Modeling Wireless Telemetry in Deep Oil Well / Julio Acosta Rams; advisor: Gláucio Lima Siqueira; co-advisor: Guilherme Simon da Rosa. – Rio de janeiro: PUC-Rio , Departamento de Engenharia Elétrica, 2019.

v., 131 f: il. color. ; 30 cm

Dissertação (mestrado) - Pontifícia Universidade Católica do Rio de Janeiro, Departamento de Engenharia Elétrica.

Inclui bibliografia

1. Engenharia Elétrica – Teses. 2. Telemetria sem fio;. 3. Prospecção de Petróleo;. 4. Formulação Semi-Analítica;. 5. Meios Anisotrópicos Estratificados;. 6. Ondas de superfície.. I. Lima Siqueira, Gláucio. II. S. da Rosa, Guilherme. III. Pontifícia Universidade Católica do Rio de Janeiro. Departamento de Engenharia Elétrica. IV. Título.

CDD: 621.3

Acknowledgments

First of all, I would like to thank my parents for all the dedication, support, love..., and despite being far away they are always present.

I want to thank Carina for all her love and patience. Without you nothing would be the same. Thanks for every single piece of our history.

I am so grateful to my advisor, Professor Gláucio Lima Siqueira, for all the support, guidance, trust, and specially for bring me to the electromagnetic world.

I want to thank my co-advisor, Professor Guilherme S. da Rosa. This work would not have been possible without his continuous support. I am very grateful for the opportunity to work with him.

I want to thank my friends Dayrene and Adrian for all the shared moments and all the support, specially in the last months. Thanks for being there for me. More than friends, they became family.

I want to thank my colleagues and friends from CETUC for make me feel at home, specially to Randy, Leonardo, Dailys, Yuneisy, José Bruno, Yoiz, Johnes, and Marcelo Balisteri.

Also, I want to thank my family-in-law for all the support, care and unconditional help.

Finally, I want to thank Jorge Raul, Yaimara and Kirenia, who opened the door of their home and made me part of their family.

I am truly thankful to Pontifical Catholic University of Rio de Janeiro and CETUC for giving me the opportunity of start building a future.

This work was supported in part by the Brazilian Agency CNPq under Grant 162410/2017-4, in part by the Brazilian Agency FAPERJ under grant E-26/202.422/2018, and in part by the Petrobras under grant provided by the project TCBR-477.

Abstract

Acosta Rams, Julio; Lima Siqueira, Gláucio (Advisor); S. da Rosa, Guilherme (Co-Advisor). **Electromagnetic Wave Propagation in Biaxially Anisotropic Media with Azimuthal Symmetry for Modeling Wireless Telemetry in Deep Oil Well**. Rio de Janeiro, 2019. 131p. Dissertação de Mestrado – Departamento de Engenharia Elétrica, Pontifícia Universidade Católica do Rio de Janeiro.

Electromagnetic telemetry systems through complex geological formations have been increasingly investigated in the last decade due to important engineering applications for the oil and gas industry exploration. Many brute-force computational electromagnetic techniques have been used for modeling this scenario. However, they require a tricky treatment of the large conductivity contrasts present in the soil formations. Also, high-cost computational resources are required for the discretization process and the low-frequency instabilities become critical for such large-scale problems. This research presents a semi-analytic formulation for analyzing the electromagnetic field propagation in a biaxially anisotropic and lossy stratified media. The proposed solution employs a novel spectral domain approach where a Hankel-based integral transform is introduced for modeling wave propagation due to azimuthally symmetric current loop sources. The proposed method is employed for analyzing geophysical scenarios analogous to those of the Brazilian Pre-Salt, where high conductivity carbonate rocks are prevalent. Also, the effect of the pre and post-salt formations on the electromagnetic fields and its interaction with the metallic casing of an oil well is then computed for both isotropic and anisotropic environments. It is presented a series of validation results which show that the proposed technique is numerically stable, robust and computationally efficient for modeling several representative problems of wireless oil well telemetry.

Keywords

Wireless Telemetry; Well-logging; Semi-Analytic Formulation; Anisotropic Stratified Media; Surface waves.

Resumo

Acosta Rams, Julio; Lima Siqueira, Gláucio; S. da Rosa, Guilherme. **Propagação de Ondas Eletromagnéticas em Meios com Anisotropia Biaxial e Simetria Azimutal para Modelagem de Telemetria Sem Fio em Poços de Petróleo**. Rio de Janeiro, 2019. 131p. Dissertação de Mestrado – Departamento de Engenharia Elétrica, Pontifícia Universidade Católica do Rio de Janeiro.

Os sistemas eletromagnéticos de telemetria através de formações geológicas têm sido cada vez mais estudados na última década devido às importantes aplicações de engenharia para a indústria de exploração de óleo e gás. Várias técnicas computacionais puramente numéricas têm sido utilizadas para modelar esses cenários. No entanto, elas exigem um tratamento ardiloso para às bruscas mudanças na condutividade elétrica presente nas formações geológicas. Além disso, o custo computacional necessário para o processo de discretização é muito grande, e as instabilidades em baixas frequências se tornam críticas para problemas em que largas escalas estão envolvidas. Esta pesquisa apresenta uma formulação semianalítica para analisar a propagação dos campos eletromagnéticos em um meio estratificado, dissipativo, e com anisotropia biaxial. A solução proposta emprega uma nova abordagem no domínio espectral onde uma integral baseada na transformada de Hankel é apresentada para modelar a propagação de ondas devido a fontes de corrente do tipo anel com simetria azimutal. O método proposto é empregado para a análise de cenários geofísicos análogos aos do Pré-Sal brasileiro, onde rochas carbonáticas de alta condutividade são predominantes. Além disso, o efeito das formações do pré e pós-sal nos campos eletromagnéticos e sua interação com o tubo metálico que reveste o poço de petróleo é então computado para ambientes isotrópicos e anisotrópicos. É apresentada uma série de resultados de validação que mostram que a técnica proposta é numericamente estável, robusta e computacionalmente eficiente para modelar vários problemas representativos de telemetria sem fio em poços de petróleo.

Palavras-chave

Telemetria sem fio; Prospecção de Petróleo; Formulação Semi-Analítica; Meios Anisotrópicos Estratificados; Ondas de superfície.

Table of contents

List of figures

List of tables

List of Abreviations

2D and 3D	The two- and three-dimensional spaces, respectively.
ANP	Brazilian National Agency for Petroleum, Natural Gas and Biofuels
BC	Boundary Conditions
bps	Bits-per-second
CEM	Computational Electromagnetics
EM	Electromagnetic
EMF	Electromagnetic Motive Force
FDM	Finite Difference Method
FDTD	Finite Difference Method in Time Domain
FEM	Finite Element Method
IE	Integral Equation
LAD	Logging After Drilling
LHS	The left-hand side of an equation
LWD	Logging While Drilling
MOM	Method of Moment
MWD	Measuring While Drilling
NMM	Numerical Matching Method
PDE	Partial Differential Equation
PEC	Perfect Electrical Conductor
RF	Radio Frequency
RHS	The right-hand side of an equation
SCTL	Single Conductor Transmission Line
TBC	Transition Boundary Condition
TE	Transversal Electric
TM	Transversal Magnetic
TTE	Through the Earth

1
Introduction

1.1
General Introduction

According to the Brazilian National Agency for Petroleum, Natural Gas and Biofuels (ANP), in the next few years the Pre-Salt exploration will have a potential US$ 334 billion revenue by year, boosting Brazil to be in the top-five petroleum players in the world [1, 2]. This will demand hundreds of new exploration wells, and as in any large-scale problem, cost-efficient solutions should be explored in order to reduce the total budget. Consequently, the exploitation of the Brazilian Pre-Salt layer has driven the research for efficient processes related to the well completion and monitoring.

In general, an oil well can be categorized into two different phases: before and after the drilling completion. In the first phase, real-time measurement while drilling (MWD) and logging while drilling (LWD) tools allows steering the drilling direction according to the response of several sensors placed near the drilling bit, while measuring the physical properties of the formation surrounding the well being drilled. Besides historically based on wireline technology, wireless MWD and LWD sensors are today becoming prevalent in the industry, and the most commonly employed measurements include neutron porosity via X-ray, compressional and shear slowness via acoustic waves, electrical resistivity via electromagnetic fields, among others [3].

Subsequently to the drilling completion, in the second phase, the major problem of an oil well relies on monitoring its integrity and the safety operation. There are several downhole sensors and valves that enable to detect anomalies in the integrity of the producing well. In Fig. 1.1, a typical oil well is presented, where a telemetry system is required for the transmission of the downhole sensors logging data to the surface.

The transmission of logging signals of such sensors along an oil well can be achieved by using electrical cables or optical fibers connecting the earth's surface to the downhole instrumentation [4]. However, the high cost of cabling, the possibility of cable tangling, breaking or not making adequate electrical contact, cause that the transmission of signals along with the oil wells, using

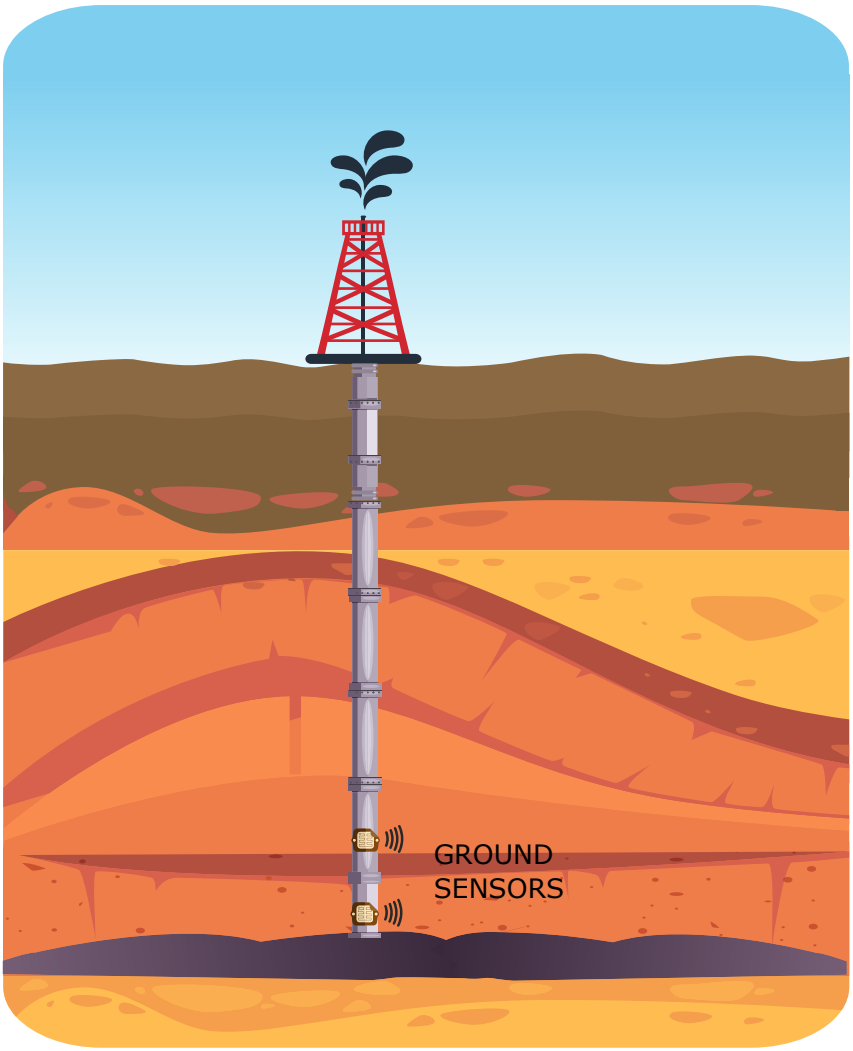

Figure 1.1: Sectional view of an oil well.

electrical cables or optical fibers, may not be a viable alternative [5]. The wireless telemetry systems can overcome these problems. In this context, the problem addressed in this dissertation is focused on computational electromagnetic solutions for wireless telemetry in oil field scenarios.

Numerous types of wireless telemetry methods are used in practice today. The most prevalent approach is based on mud pulse propagation [6], which utilizes a valve to adjust the mud pressure so that it can represent different digital bits to send logging data up to the surface. The data rate of this kind of system is limited by the nature of the mechanical (or seismic) waves and the sources to generate them, nevertheless, the most commonly used solutions reach up to 15 bits-per-second (bps) [5]. Compared with the majority of the wireless communication systems that people use nowadays, this data rate is way too low, but, due to severe attenuation that a seismic wave suffer in typical geophysical environments, such rate borders the maximum limit that can be achieved [3]. Such data rates, however, should increase for allowing real-time

telemetry systems for deep oil well (along up to 4 km) as those of the Brazilian Pre-Salt.

Several companies provide electromagnetic (EM) or acoustic telemetry systems by using a low-frequency electric source or sonic source as downhole wireless transmitters [5]. These systems have advantages and drawbacks in different environments, and the solutions that provide the better performance is influenced by the well depth, formation geometry and media properties, transmission/reception structure, among other parameters. It is important to emphasize that the most critical modeling parameters in electromagnetic telemetry are the constitutive characteristics of the soil formation surrounding the well. The geometry of a well can be approximated as a horizontally layered media composed of several layers along the axial direction. The rocks in the formation are predominantly anisotropic, where a uniaxial transverse isotropic media is a suitable model. However, the overall purpose of this study is to evaluate the impact of the well environment on electromagnetic wave propagation of time-harmonic fields, for which a biaxial anisotropic model is employed.

In free-space, gigabits per second can be transmitted over several kilometers by using microwave frequencies. As the media becomes lossy (e.g., due to the dissipative characteristics of the formation), the electromagnetic wave propagation at such high frequencies becomes unfeasible. As an alternative, low-frequency time-harmonic fields can be used in a short hop electromagnetic telemetry when mechanical wave propagation is impracticable.

Due to the high-cost measurements required for modeling a wireless telemetry system in an actual oil well, the practical applicability of such communication channels should first be assessed in a simulation environment. The electromagnetic wave propagation characteristics in these complex media can be analyzed by using many computational electromagnetic (CEM) techniques. Typically, a CEM solution can be employed for approximating Maxwell's equations when an analytical approach is not available.

The simulation of an oil well using wireless telemetry requires a spatial domain with several kilometers of length (along with the three spatial directions). The accurate analysis of this kind of problem via commercial CEM software requires a giant amount of computing resources for the discretization process and it usually takes a long computational time to provide any useful result. In other words, this process is computationally slow, has a strong dependence on its grid size and is computationally expensive in terms of processing time.

1.2 Objectives of the Dissertation

Two main issues must be considered when modeling the electromagnetic wave propagation for oil well telemetry problems: the antenna losses (that measures how such radiators couple its power with the media) and the radio frequency (RF) attenuation. Despite the characteristics of the antenna play an important role in the overall attenuation of the fields (as a consequence of the terminal antenna impedance mismatching and mainly due to the polarizations effects), the propagation of waves through several kilometers into a complex downhole formation, as depicted in Fig. 1.1, makes the RF attenuation the main concern for such telemetry problems. There exist some recent research on the losses of the antennas that can be found in [7], but one will assume herein such antenna issues can be properly addressed via some kind of near-zone simulations as well as via proper representative measurements.

The main purpose of this research is to provide an accurate, robust and stable semi-analytical solution for solving electromagnetic wave propagation for oil well wireless telemetry. This method has clear physical and mathematical meaning in each solution step.

The scope of this work includes the analysis of the electromagnetic wave propagation due to azimuthally symmetric sources in biaxial anisotropic media with axial stratifications. It is also analyzed the propagation of the radiated electromagnetic fields via two different mechanisms: along the soil formation (through the earth (TTE) communication) and by surface guided waves alongside to metallic structures embedded in the soil.

A series of illustrative examples and representative problems of wireless telemetry in deep wells will be analyzed herein. Numerical results obtained with the proposed semi-analytical solution will be validated against a finite element method (FEM) solver (provided by the COMSOL Multiphysics), and its computational cost, stability, and accuracy will then be verified.

It is important to remark that the modeling of realistic antennas is out of the scope of this work. Some conclusions about the polarization of the antennas, however, will be established herein in order to improve the communication link quality based on the geometry of the oil well environment.

1.3 Major Research Contributions

To the best of the authors' knowledge, the presented study in this work is relevant both in technological as well as in academic aspects for modeling telemetry systems employed by the petroleum industry. In special, to the

imminent demands for the exploration progress of the Brazilian Pre-Salt Layer. Accordingly, the following topics correspond to the authors' original scientific contributions:

- The development of a novel spectral domain approach where a Hankel-based integral transform is introduced.
- The study and development of a semi-analytical formulation for analyzing the electromagnetic field propagation along a metallic cylindrical rod immersed in a biaxially anisotropic and lossy media composed of horizontal stratifications.
- A numerically stable and robust method for accounting the finite electrical conductivity of metallic cylinders embedded in a biaxially anisotropic medium.

1.4 Organization of the Dissertation

This dissertation is organized as follows. In Chapter 2 the state of-art-of of well logging tools is presented. Two logging techniques are described, and some possibilities for telemetry systems are also presented. Then, an electromagnetic characterization of downhole formations is performed, highlighting the conductivity of the media and its influence for telemetry systems. At the end of this chapter, some analytical and computational methods in electromagnetism are described and compared.

In Chapter 3, is introduced the mathematical formulation for the complete electric and magnetic field response of a uniform azimuthally symmetric current loop source in a biaxially anisotropic media via a spectral domain solution. It is also addressed the propagation of electromagnetic signals along the surface of a cylinder metal rod. Simulation results to evaluate the performance of the proposed technique are provided.

In Chapter 4, the effects of axial stratifications in the downhole formation are discussed. The mathematical formulation of the electromagnetic field responses assessing the multiple reflections of the waves is presented as well. Some numerical results are presented in order to verify the accuracy and efficiency of the proposed solution.

In Chapter 5, an impedance boundary condition to model the losses of the cylinder metallic rod for surface wave propagation is considered. It is proposed the mathematical formulation to modeling the impedance boundary condition, and some simulations are performed to validate the proposed solution.

Finally, Chapter 6 summarizes the most important results achieved in this work, and future directions for this research topic are also pointed out.

2
Oil Well Wireless Telemetry Systems and Techniques

2.1
Introduction

Well logging is the field in petrophysical exploration that has the purpose of locate oil and gas in a soil formation by means of a borehole. The results of the logging process give petrophysicists a quantitative measure of the formation parameters (resistivity, wave velocity, etc.) so that the production rate, formation quality, depth of production zone, and productivity can be evaluated [3].

In this chapter is presented the state-of-art of well logging tools, drilling techniques and some configurations for telemetry systems. It is described the electromagnetic characteristics of the downhole formation and the effects of the conductivity on the electromagnetic wave propagation. Finally, some analytical and computational methods in electromagnetism are described and compared.

2.2
Oil Well Logging Tools

Several numerical methods used in logging for the electrical, electromagnetic, acoustic, and seismic characterization have been researched and reported in literature [8–14]. When the measurement equipment is directly attached to a drilling bit, the measurement is performed during the drilling. This direct measurement method is called logging while drilling (LWD). On the other hand, when the logging is performed after the drilling activity in a borehole, the method is named logging after drilling (LAD), where wireline tools are use generally [3].

The first LAD mechanisms were attached into the logging tools by a multiple-conductor wireline. Once the well was drilled, the logging tools were sent down into the open borehole, and the measurements are performed while being pulled upward. The logging data were either stored in the memory of the tools and retrieved on the surface, or alternatively, they were directly transmitted up through the wireline. Nevertheless, for highly deviated or horizontal boreholes, it may be difficult for the tools to enter by gravity

to perform the measurements. Furthermore, sometimes the tools must be pumped into the wellbore to obtain the measurements, which makes the logging procedure extremely time-consuming [3].

LWD solved this problem by integrating the measure tool to the drill pipe, and conduct continuous measurements while the drilling proceeds. Data are still recorded to the memory for download afterwards, or the tools can send part of the information through a telemetry system, which communicates with the surface in real time.

Oil well wireless telemetry can be used for both, LWD and LAD, specially in unconventional drilling, allowing to transmit data in real time from downhole sensors to the surface while or after an oil well is being drilled. Those sensors generally provide information of the soil formation properties, as porosity and the electrical resistivity, and help operators to optimize the drilling path to improve production [13].

Wireless telemetry systems for oil well usually employ a low frequency time-varying magnetic field as a source for the excitation of electrical currents into the ground, by using the principle of magnetic induction. The energy source may be as well an electric field or changing magnetic field, while the data can also be either electric or magnetic field values.

In Fig. 2.1 is presented a typical vertical well production using wireless telemetry. Historically, the exploration of oil and gas involved the use of vertical wells as a result of directional drilling being a complicated and expensive technology. However vertical wells have limited angles that reduce its capacity to reach wider sections of the downhole. They can only have access to areas directly below reserves. Therefore, making a large production often requires the drilling of many vertical wells at various points along the formation [15].

Nowadays directional drilling is becoming more common. This technology allows controlling the direction and deviation of a wellbore to a predetermined underground target or location, letting wells to lay on along the formation at depth. This configuration allows that a single directional well has access to the same amount of oil that would have required multiple vertical wells [16].

In Fig. 2.2 is presented a directional well using the soil and rocks as a propagation medium for wireless telemetry. These systems provide trough the earth (TTE) telemetry, and they employ electromagnetic waves to establish a communication link between the underground sub-soil and the surface [17–22]. TTE systems generally employ magnetic induction at low frequency (below 30 kHz), and therefore, they provide a very low bandwidth. The main reason for the use of low frequencies is the presence of rocks, soil water, minerals, and other materials with non-negligible electrical conductivity in the underground

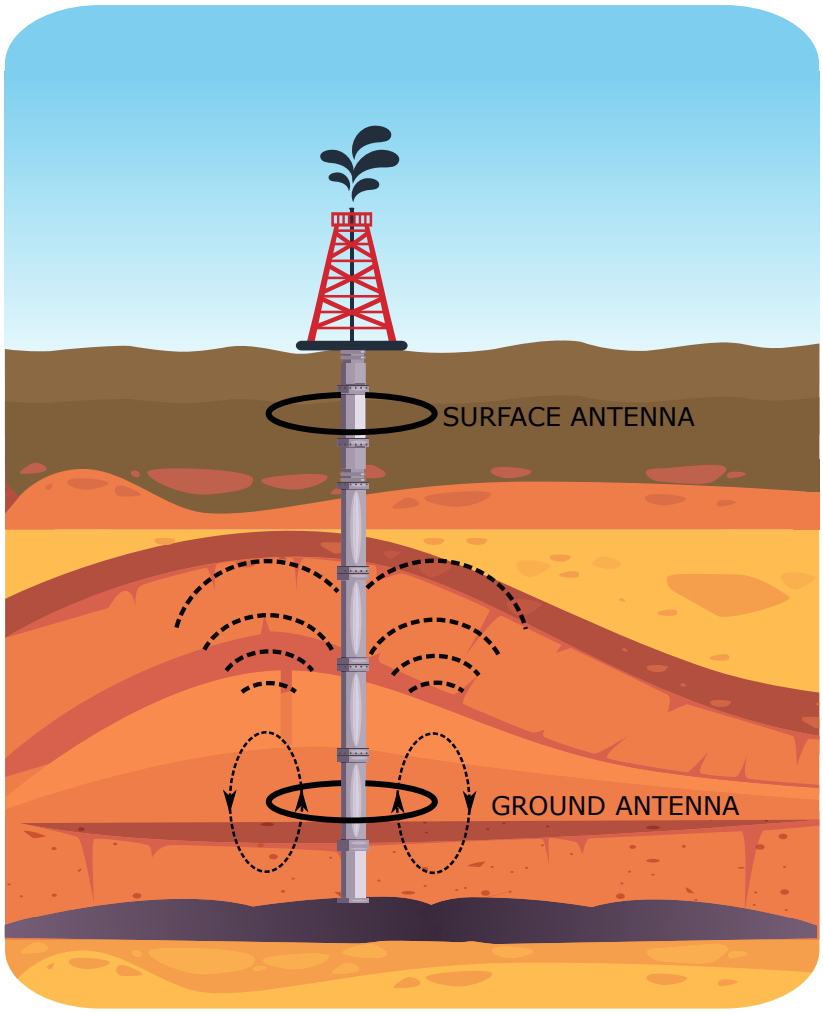

Figure 2.1: Sectional view of a vertical oil well using wireless telemetry.

formation, which results in a very deep attenuation. Despite TTE systems have been developed mainly for emergency communications in mines, they represent an alternative communication link when no other communications system can be used.

2.3 Previous Work on Electromagnetic Propagation for Oil Well

Electromagnetic field propagation in planar stratified media has been investigated for more than a century. This topic is a subject of interest of several areas, including geophysics, optics, remote sensing, as well as in microwave TTE propagation. The techniques developed for one area, however, are often applicable to others. Different algorithms and methods to model electromagnetic telemetry and determine the fields components along planar stratified media have been proposed in literature [23–30]. The author of [24] employed the Fourier-Bessel method to generalize the Sommerfeld [31] problem to the case of n-homogeneous layers.

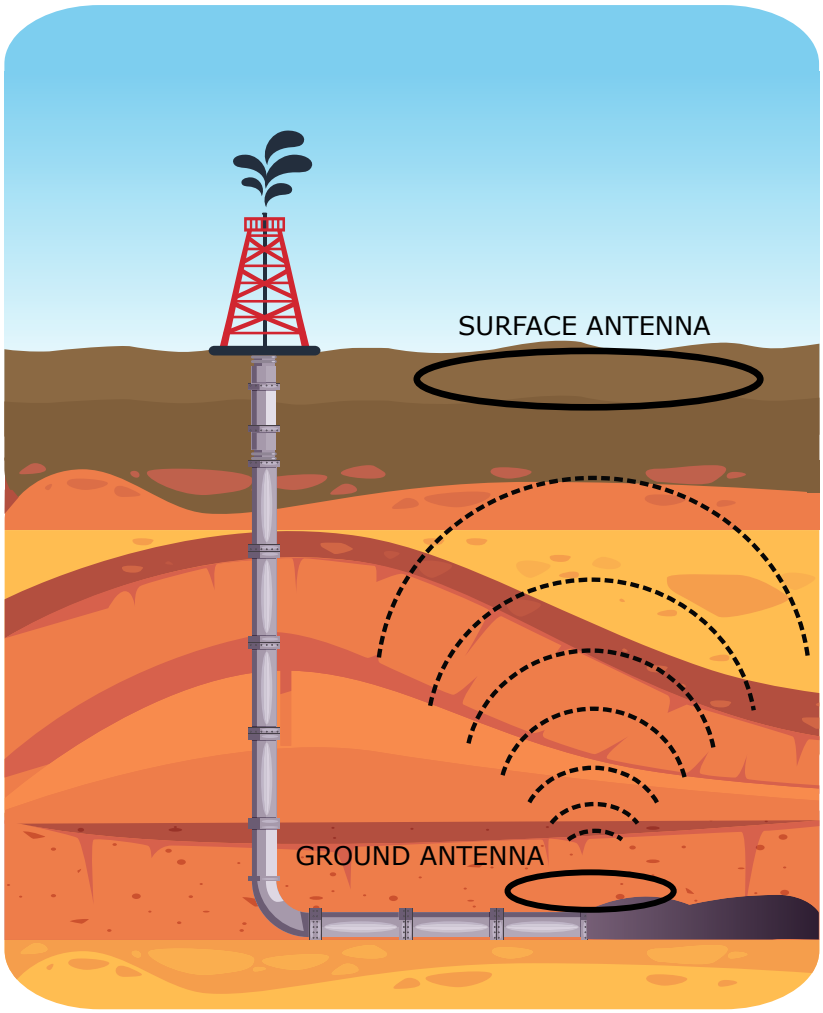

Figure 2.2: Sectional view of a horizontal/directional oil well using wireless telemetry.

A calculation of the diffraction of axisymmetric borehole waves by bed boundary discontinuities is presented in [32]. The approach consists of a discrete part as well as a continuum mode spectrum. In order to simplify the problem, it is proposed a systematic way to approximate the continuum modes by discrete ones.

In [33] is presented a generalized Hankel transform method to solve two-dimensional inhomogeneous environment. It is assessed the effect of horizontal geological beds on the propagation of electromagnetic waves through a cylinder in a geophysical probing environment. The solution proposed involves a generalized kind of Hankel integral transform, however, it shows convergence issues due overburden in the numerical integration.

Also, the response of different sources, such as point sources, electric and magnetic dipole, electric and magnetic current loop antennas, and toroidal coils, embedded in stratified media have been researched. In [34, Ch. 2] is proposed a pseudo-analytical technique to model line and point sources in an

axially-layered isotropic structure in terms of Fourier-type integrals. In [35] is considered the electromagnetic fields produced by a circular loop of uniform current for a homogeneous half-space model of the ground. The electromagnetic fields produced by dipole sources in planar-stratified environments with anisotropic layers is studied in [27,36,37]. Also, an analysis of the electromagnetic fields excited by a toroidal coil, which is coaxial with a circular metal rod is presented in [25].

Numerical matching methods (NMM) have also been reported for modeling electromagnetic telemetry systems of vertical and directional wells in both radial and axial layered anisotropic formations [13,38].

All these approaches are classified as semi-analytical, and have its advantages and limitations, but they are a good choice over the brute-force methods. A comparison between such methods will be presented in Section 2.5.

2.4 Electromagnetic Characteristics of Downhole Formations

Generally, downhole formations are composed of different types of materials, including rock, water, oil, gas, and others. Most soil and rock minerals are electrical insulators due to its very low electrical conductivity. This parameter characterize how easy the current flows through the material when an electrical force is applied. Nevertheless, some rocks may have sufficient quantities of conductive minerals such as magnetite, carbon, graphite, pyrite and pyrrhotite, that increase their overall conductivity [39].

Typical rocks of downhole formations are a mixture of rock frame and materials existing in its pore space and passages that are contained within the insulating matrix, where the conductivity of the rock is determined by the [40]:

1. Rock type.
2. The porosity and interconnecting passages of the rocks: number of pores, shape and size.
3. The degree of filling of the pores with the moisture content.
4. The nature of the fluid and metallic content of the solid matrix.
5. The concentration of dissolved electrolytes in the moisture content.

In general, most rocks that contain oil and gas are porous, like sandstone and carbonate. The pore spaces in rocks are where the oil and gas are stored.

It is important to highlight that the conductivity of a composite material such as a sediment rock is largely dependent on the conductivity of each component in the rock, either the pore space and the liquid or gas occupying

it. Hence the overall electromagnetic characteristics of mixed material can be better defined from the concepts of effective electric permittivity, magnetic permeability, and conductivity [39].

According to its electrical property, a medium can be isotropic, transverse isotropic (TI), biaxial anisotropic (or fully anisotropic). Many geologic formations exhibit fully anisotropy (i.e., the conductivity varies with direction), where all three principal conductivities are different [3].

From the petrophysicist's point of view, the important issue is not the conductivity of the rock itself, but the porosity, density, permeability, and contents of the rocks [3]. From the telecommunication engineer's point of view, the electrical conductivity σ of the subsoil is the main parameter to be analyzed, since the propagation of waves in these media is very sensitive to it. However, the wave propagation is also conditioned by the magnetic permeability and electrical permittivity of the rocks, and its relevance depends upon the frequency of the signal used for a given system.

The electrical conductivity of Earth's materials varies over many orders of magnitude. In Fig. 2.3 is presented a rough indication of the range of conductivity for rocks and mineral.

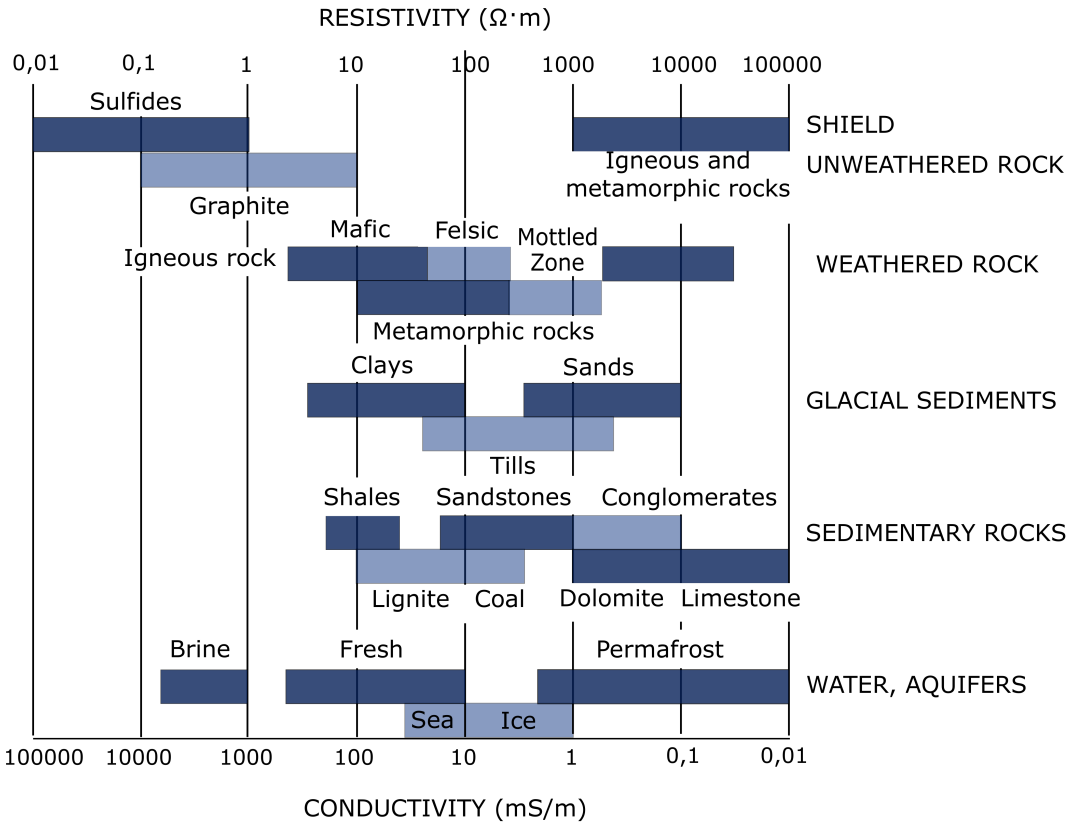

Figure 2.3: Range of conductivity (σ) and resistivity ($1/\sigma$) variations for terrestrial materials. (Adapted from [39])

2.5 Analytical, Semi-Analytical, and Numerical Computational Methods in Electromagnetism

There are two broad classes of solution that can be employed for boundary value problems: the analytical methods and computational or numerical methods. They provide solutions to Maxwell's equations by different forms, and depending on the characteristics of the problem, a method may be more adequate than the other. In Table 2.1 (reproduced from [3]) is presented a comparison between analytical, semi-analytical (hybrid), and numerical methods, bringing out their advantages and limitations.

Historically, analytical methods responded to the urge of engineers to solve mathematical problems without the use of computers. The most common analytical techniques include the method of separation of variables, orthogonal function expansion method, Green's function, method of images, analysis in spectral or Fourier domain, conformal mapping, and variational methods. Most of these methods are covered in [41–43]. The method of separation of variables is one of the most used and elegant analytical method, and is the one employed through this work in Chapters 3 and 4.

There are several problems that can be solved analytically, among them: the wave propagation in rectangular, circular, and elliptic waveguides; cavity resonance within rectangular, cylindrical, and spherical cavities; scattering by infinite planes, wedges, circular cylinders, and spheres; and static potential between infinite parallel plates. The solutions for these problems are biased towards analytical closed-form solutions of the wave equation, and generally are applicable to simple shape structures. However, most of the device geome-

	Analytical method	**Hybrid method**	**Numerical method**
Has analytical solution	Yes	Half	No
Can solve 1D problems	Yes	Yes	Yes
Can solve 2D problems	No	Yes	Yes
Can solve 3D problems	No	No	Yes
Speed	Very fast	Fast	Depends on grid size
Accuracy	Very accurate solution	Depend on each case	Approximate solution

Table 2.1: Comparison between analytical, hybrid, and numerical methods [3].

tries of engineering importance do not conform to these restrictions, which limit the range of analytical methods. For complex geometries, the problems may not be analytically solved, and computational numerical approximated techniques are required to overcome the incapacity of analytical methods to derive solutions to Maxwell's equations. Some examples of these complex electromagnetic problems are the modeling of complex waveguides, electromagnetic radiation, electromagnetic scattering, etc. The utilization of this approximation techniques increases the range of analytical methods at the cost of accuracy [42].

Commercial software packages such as COMSOL [44], HFSS (ANSYS) [45], and Maxwell (ANSYS) [46], are considered as effective numerical tools in electromagnetic system design and analysis. These softwares implement numerical techniques for finding approximate solutions for complex problems in one-dimension (1D), two-dimensions (2D), and three-dimensions (3D). There are several kinds of numerical method which are widely used in commercial softwares: finite element method (FEM), method of moment (MOM), finite difference method (FDM), and finite difference method in time domain (FDTD), among others. In general, all of these methods are capable of solving Maxwell's equations and can be used to solve logging and telemetry problems. Each numerical method has its own characteristics and are suitable for certain applications. A resume with some of the characteristics of the principal numerical methods when solving electromagnetic problems is presented in Table 2.2 (reproduced from [3]). In such table, PDE is a short for partial differential equation and IE is for integral equation.

Since logging and telemetry for deep oil wells problems are typically low frequency inhomogeneous volume-dominated problems, FEM and FDM are the more common methods. However, when the problem has a complex structure, the FEM can adjust better due its flexibility. These methods require the solution of a set of simultaneous equations, where several matrix operations are performed repeatedly to obtain the potential, field, or current distribution. The computer resources, such as RAM memory and CPU processing time, required to solve the mathematical operations determine the efficiency of the computational method employed [3].

For some simulations scenarios, these brute-force techniques can become prohibitive, and semi-analytical approaches may handle these inconveniences in a more efficient way. By this reason, the problem of electromagnetic telemetry will be modeled herein by using a semi-analytical method, presented in the following chapters.

Method	**FEM**	**FDM**	**FDTD**	**MOM**
Domain	Frequency	Frequency	Time	Frequency
Multifrequency	No	No	Yes	No
Is arbitrary grid	Yes	No	No	Yes
PDE or IE	PDE			IE
Surface or volume	Volume			Surface
High or low frequency	Both	Both	Prefer High	Both
Matrix system size	Large			Small
Matrix system density	Very sparse			Full
Best suited for	Inhomogeneous medium			Piecewise homogeneous medium
Best suited for	Volume dominated problem			Surface dominated problem

Table 2.2: Comparison between different numerical methods [3].

3
Electromagnetic Analysis

3.1
Introduction

Mostly wireless telemetry systems for underground formations use transmitter and receiver coils fed by current sources, which induce eddy current loops by generating magnetic field in the formations, as depicted in Fig. 3.1. These eddy current loops generate secondary magnetic field, that induce an electromagnetic motive force (EMF) in the receiver coil. This method for oil wells is based on two fundamental principles: Faraday's law of electromagnetic induction and Ampere's law for magnetic fields generated by electric currents.

In practice, the sources for induction telemetry systems operates at low frequency, which is justified due to the high attenuation that the fields suffer

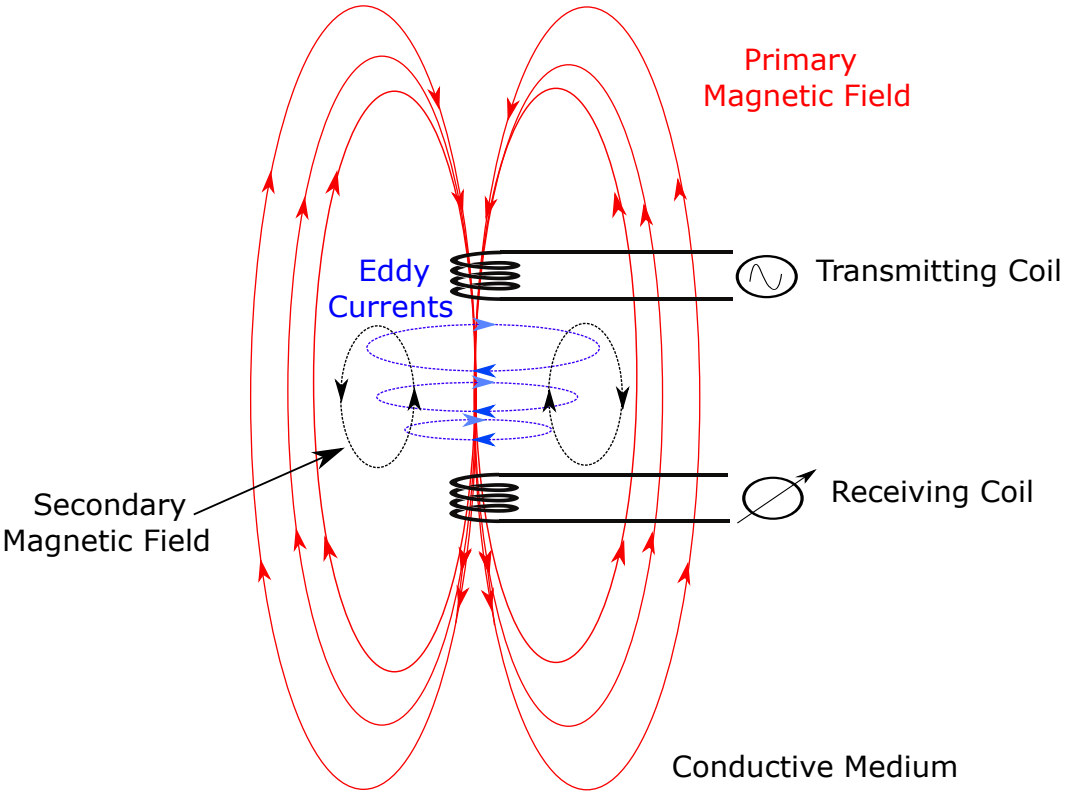

Figure 3.1: Induction wireless telemetry.

because of the conductivity of the media. When an EM wave enters the conducting layers of the Earth, it still propagates, but it travels much slower compared with free-space propagation, and attenuates rapidly as it propagates deeper. This attenuation increases with the frequency.

Another important parameter that conditions the strength of the electromagnetic field is the geometry of the source. For these systems, the type and size of the antennas are very limited by the available physical space, and they impact directly in the radiation characteristics for the low-frequency operation [47]. It is important to highlight that the modeling of the antennas is out of the scope of this dissertation. Consequently, in order to simplify the analytical-modeling of the source, a circular loop antenna will be employed as the excitation.

In this chapter it will be derive the electric and magnetic field response of a uniform azimuthally symmetric current loop source in a biaxially anisotropic media. The solution will be obtained from Maxwell's equations, where the inclusion of anisotropy makes the mathematical formulation quite complicated, but very useful and generic for geophysical problems. Some simplifications will be done in order to facilitate the modeling. The solution can be applied to the analysis of TTE propagation for directional well telemetry. It will be also analyzed the transmission of electromagnetic signals along the surface of a cylinder metallic rod, with application for vertical wells modeling. Even though numerical solutions can be applied, the analytical solutions are always advantageous in terms of computation speed and mainly because several physical and geometric interpretations can be derived.

3.2 Electromagnetic Field Theory

Throughout this work it will be adopted a notation similar to that used in [34], where the time dependence $e^{-i\omega t}$ is assumed and suppressed. Also, the problem at hand has a geometry with boundaries conformal with cylindrical coordinate (ρ, ϕ, z).

The Maxwell's equations in linear, homogeneous and dissipative

anisotropic media satisfy

$$\nabla \times \mathbf{E} = \bar{\bar{z}} \cdot \mathbf{H} - \mathbf{J}_m, \tag{3-1}$$

$$\nabla \times \mathbf{H} = -\bar{\bar{y}} \cdot \mathbf{E} + \mathbf{J}_e, \tag{3-2}$$

$$\nabla \cdot (\bar{\bar{\epsilon}} \cdot \mathbf{E}) = \rho_e, \tag{3-3}$$

$$\nabla \cdot (\bar{\bar{\mu}} \cdot \mathbf{H}) = \rho_m, \tag{3-4}$$

where $\mathbf{E}$ is the electric field in V/m, $\mathbf{H}$ is the magnetic field in A/m, $\mathbf{J}_e$ is the impressed electric current density in A/m^2 and $\mathbf{J}_m$ is the impressed magnetic current density in V/m^2, ρ_e is the electric charge density in C/m^3, and ρ_m is the magnetic charge density in Wb/m^3. The impeditivity and admitivity tensors are given by $\bar{\bar{z}} = i\omega\bar{\bar{\mu}}$ and $\bar{\bar{y}} = i\omega\bar{\bar{\epsilon}}$, and are expressed in terms of impedance per meter and admittance per meter, respectively. The media is characterized by the complex magnetic permeability and electric permittivity tensors

$$\bar{\bar{\mu}} = \begin{bmatrix} \mu_\rho & 0 & 0 \\ 0 & \mu_\phi & 0 \\ 0 & 0 & \mu_z \end{bmatrix} \quad \text{and} \quad \bar{\bar{\epsilon}} = \begin{bmatrix} \epsilon_\rho & 0 & 0 \\ 0 & \epsilon_\phi & 0 \\ 0 & 0 & \epsilon_z \end{bmatrix}, \tag{3-5}$$

respectively, where the complex permeability and permittivity are defined as

$$\begin{aligned} \mu_{\{\rho,\phi,z\}} &= \mu_0 \mu_{r\{\rho,\phi,z\}}, \quad \text{and} \\ \epsilon_{\{\rho,\phi,z\}} &= \epsilon_0 \epsilon_{r\{\rho,\phi,z\}} + \frac{i}{\omega}\sigma_{\{\rho,\phi,z\}}. \end{aligned} \tag{3-6}$$

In the above, the terms μ_{r_α}, ϵ_{r_α} and σ_α are the relative magnetic and dielectric constants, and the effective electrical conductivity of the medium in the α-direction, respectively. It can be noticed that imaginary part of the effective dielectric constant involves the effect of the conductivity σ. In the case of high frequency (megahertz to gigahertz) or non-conductive media, the real part plays the major role in the complex dielectric constant. Otherwise, when the frequency is low, the conductivity dominates.

The curl, vector and scalar Laplacian, divergence and gradient operator in cylindrical coordinates are defined as [48]

$$\nabla \times \mathbf{A} = (\frac{1}{\rho}\frac{\partial A_z}{\partial \phi} - \frac{\partial A_\phi}{\partial z})\,\hat{i}_\rho + (\frac{\partial A_\rho}{\partial z} - \frac{\partial A_z}{\partial \rho})\,\hat{i}_\phi + \frac{1}{\rho}(\frac{\partial(\rho A_\phi)}{\partial \rho} - \frac{\partial A_\rho}{\partial \phi})\,\hat{i}_z, \tag{3-7}$$

$$\nabla^2 \mathbf{A} = (\nabla^2 A_\rho - \frac{A_\rho}{\rho^2} - \frac{2}{\rho^2}\frac{\partial A_\phi}{\partial \phi})\,\hat{i}_\rho + (\nabla^2 A_\phi - \frac{A_\phi}{\rho^2} + \frac{2}{\rho^2}\frac{\partial A_\rho}{\partial \phi})\,\hat{i}_\phi + (\nabla^2 A_z)\,\hat{i}_z, \tag{3-8}$$

$$\nabla^2 f = \frac{1}{\rho}\frac{\partial}{\partial\rho}(\frac{\rho\partial f}{\partial\rho}) + \frac{1}{\rho^2}\frac{\partial^2 f}{\partial\phi^2} + \frac{\partial^2 f}{\partial z^2}, \tag{3-9}$$

$$\nabla\cdot\mathbf{A} = \frac{1}{\rho}\frac{\partial(\rho A_\rho)}{\partial\rho} + \frac{1}{\rho}\frac{\partial A\phi}{\partial\phi} + \frac{\partial A_z}{\partial z}, \tag{3-10}$$

$$\nabla f = \frac{\partial f}{\partial\rho}\,\hat{i}_\rho + \frac{1}{\rho}\frac{\partial f}{\partial\phi}\,\hat{i}_\phi + \frac{\partial f}{\partial z}\,\hat{i}_z. \tag{3-11}$$

Using the procedure described in [34], dot-multiplying (3-1) by $\bar{\bar{z}}^{-1}$ and then taking the curl of both sides, results in

$$\nabla\times\bar{\bar{z}}^{-1}\cdot\nabla\times\mathbf{E} = \nabla\times\mathbf{H} - \nabla\times\bar{\bar{z}}^{-1}\cdot\mathbf{J}_m. \tag{3-12}$$

Substituting (3-2) into the above it is obtained

$$\nabla\times\bar{\bar{z}}^{-1}\cdot\nabla\times\mathbf{E} = -\bar{\bar{y}}\cdot\mathbf{E} + \mathbf{J}_e - \nabla\times\bar{\bar{z}}^{-1}\cdot\mathbf{J}_m, \tag{3-13}$$

whose multiplication by $i\omega$ gives

$$\nabla\times\bar{\bar{\mu}}^{-1}\cdot\nabla\times\mathbf{E} - \omega^2\bar{\bar{\epsilon}}\cdot\mathbf{E} = i\omega\mathbf{J}_e - \nabla\times\bar{\bar{\mu}}^{-1}\cdot\mathbf{J}_m. \tag{3-14}$$

Similarly, (3-2) can be manipulated in order to derive

$$\nabla\times\bar{\bar{\epsilon}}^{-1}\cdot\nabla\times\mathbf{H} - \omega^2\bar{\bar{\mu}}\cdot\mathbf{H} = i\omega\mathbf{J}_m - \nabla\times\bar{\bar{\epsilon}}^{-1}\cdot\mathbf{J}_e. \tag{3-15}$$

The vector wave equations (3-14) and (3-15) determine the solution for the electromagnetic field impressed by the sources $\mathbf{J}_e$ and $\mathbf{J}_m$ in a homogeneous biaxial anisotropic media described by (3-5). It can be noticed that for both equations the electric and magnetic field are decoupled to each other, and they only depend of the electric or magnetic sources.

In the next section, it will be briefly presented some of the characteristics of the sources $\mathbf{J}_e$ and $\mathbf{J}_m$ that are commonly used for telemetry system through the soil formation.

3.3 Source Modeling

As it was presented previously, mostly used sources for EM telemetry in underground communications are coils, where circular loop current antennas are natural choices to be employed. It is well known, from the circuit theory, that coils are inductors. At low frequency, its impedance will be low, and therefore, such antennas are usually employed for applications at frequencies in the range of kilohertz to megahertz [3].

When a circular loop antenna is sourced by an electrical current, as in Fig. 3.2, it can be expressed by its electric current density as

$$\mathbf{J}_e = J_{e,\phi}\,\hat{i}_\phi, \tag{3-16}$$

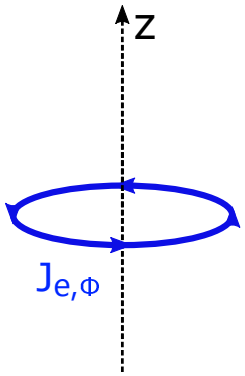

Figure 3.2: Electrical current loop antenna.

where $J_{e,\phi}$ is the electric current density distribution in the azimuthal direction. This type of antenna presents an axial symmetry along the z axis.

Another choice of antenna for oil well wireless telemetry is the toroidal antenna, which geometry is equivalent to an electrical dipole source. A toroidal antenna can be defined as a helical winding of a conducting wire around a ring of material with a high magnetic permeability, as depicted in Fig. 3.3. When an alternating current flows through the helical wire, it will generate an alternating magnetic field inside the ring, which consequently induce radial and axial currents in the surrounding formations. The core is usually made of either ferrite materials or mu-metal to increase the radiation efficiency [3].

The toroidal antenna carrying electric current can be modeled as an electric dipole, as well as a magnetic current loop. Although magnetic charges or currents do not exist in the physical world, a magnetic current loop may be used as a mathematical tool to facilitate the analytical calculations in the modeling of toroidal antennas. The schematic of a toroidal antenna, and its equivalent source model (magnetic current loop), are illustrated in Fig. 3.4.

A magnetic current loop source, which is axially symmetric along the z axis, can be expressed by its magnetic current density as

$$\mathbf{J}_m = J_{m,\phi}\ \hat{i}_\phi. \tag{3-17}$$

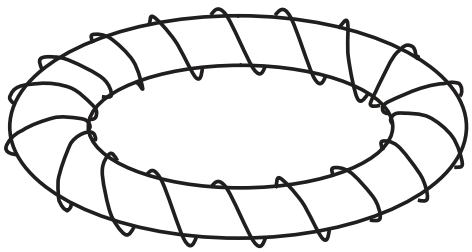

Figure 3.3: Toroidal helical antenna. (Adapted from [3])

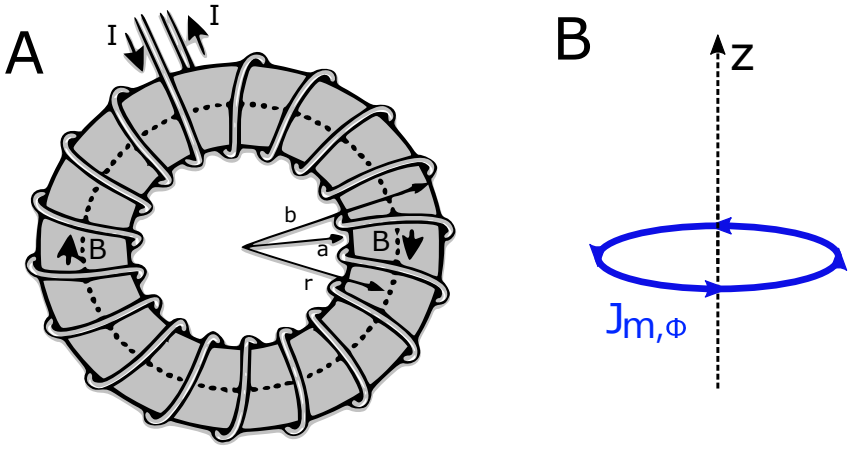

Figure 3.4: (A) Schematic of the toroidal antenna. (B) Source model of the antenna: magnetic current loop. (Adapted from [3])

where $J_{m,\phi}$ is the magnetic current density distribution in the azimuthal direction.

Furthermore, a toroidal transmitter can also be modeled theoretically as an insulating gap, as it is depicted in Fig. 3.5. This model is very useful for numerical approximation, and implies the separation of the long metal drill into two parts, with an alternating voltage source connecting to both sides of an embedded insulator [3, 30].

Through this work it will be considered the electromagnetic radiation of electric and magnetic current loops only. Because the two problems are dual of each other, the field solutions for a current loop may be easily adapted for the other one.

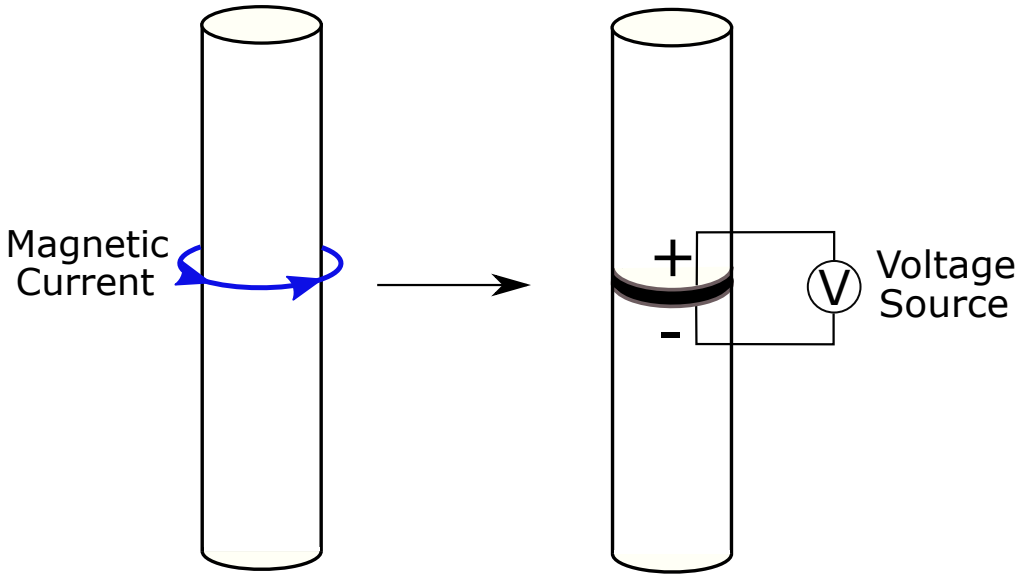

Figure 3.5: Modeling a toroidal transmitter as an insulating gap. (Adapted from [3])

3.4 Azimuthally Symmetric Electromagnetic Fields

It can be shown that in case of having the radiation of electric source only or magnetic source only, the vector wave equations satisfied by the electric field or the magnetic field are, respectively,

$$\nabla \times \bar{\bar{\mu}}^{-1} \cdot \nabla \times \mathbf{E} - \omega^2 \bar{\bar{\epsilon}} \cdot \mathbf{E} = i\omega \mathbf{J}_e, \quad \text{for} \quad \mathbf{J}_m = \mathbf{0}, \tag{3-18}$$

$$\nabla \times \bar{\bar{\epsilon}}^{-1} \cdot \nabla \times \mathbf{H} - \omega^2 \bar{\bar{\mu}} \cdot \mathbf{H} = i\omega \mathbf{J}_m, \quad \text{for} \quad \mathbf{J}_e = \mathbf{0}. \tag{3-19}$$

When the transmission antenna is a filament electric current loop placed at $\rho = \rho'$ and $z = z'$, then $\mathbf{J}_e$ in (3-19) can be described as in (3-16) with

$$J_{e,\phi} = I_e(\phi)\delta(\rho - \rho')\delta(z - z'), \tag{3-20}$$

where $I_e(\phi)$ is the electric current distribution in the azimuthal direction and $\delta(\cdot)$ is the Dirac delta. Then, the projection of (3-18) onto $\hat{i}_\phi$ results in

$$\hat{i}_\phi \cdot \nabla \times \bar{\bar{\mu}}^{-1} \cdot \nabla \times \mathbf{E} - \omega^2 \, \hat{i}_\phi \cdot \bar{\bar{\epsilon}} \cdot \mathbf{E} = i\omega \, \hat{i}_\phi \cdot \mathbf{J}_e, \tag{3-21}$$

or, the more simplified form

$$\begin{aligned} \frac{1}{\mu_\rho}\left[\frac{\partial}{\partial z}\left(\frac{1}{\rho}\frac{\partial E_z}{\partial \phi} - \frac{\partial E_\phi}{\partial z}\right)\right] - \frac{1}{\mu_z}\frac{\partial}{\partial \rho}\left\{\frac{1}{\rho}\left[\frac{\partial\left(\rho E_\phi\right)}{\partial \rho}\right] - \frac{\partial E_\rho}{\partial \phi}\right\} - \omega^2 \epsilon_\phi E_\phi \\ = i\omega I_e(\phi)\delta(\rho - \rho')\delta(z - z'). \end{aligned} \tag{3-22}$$

In the above, the three components of the electric field (E_ρ, E_ϕ, E_z) are coupled by a second-order partial differential equation. A more simplified scenario occurs, however, when the current distribution $I_e(\phi)$ is uniform and azimuthally independent. This azimuthally symmetric scenario (without ϕ variations, i.e., $\partial/\partial\phi = 0$), allows to reduce (3-22) to a second-order partial differential equation in terms of only E_ϕ, i.e.,

$$\frac{1}{\mu_\rho}\left[\frac{\partial}{\partial z}\left(-\frac{\partial E_\phi}{\partial z}\right)\right] - \frac{1}{\mu_z}\frac{\partial}{\partial \rho}\left\{\frac{1}{\rho}\left[\frac{\partial\left(\rho E_\phi\right)}{\partial \rho}\right]\right\} - \omega^2 \epsilon_\phi E_\phi = i\omega I_e \delta(\rho - \rho')\delta(z - z'). \tag{3-23}$$

The above equation can be rewritten into a more compact shape

$$-\left[\frac{\partial^2 E_\phi}{\partial z^2}\right] - \frac{\mu_\rho}{\mu_z}\frac{\partial}{\partial \rho}\left\{\frac{1}{\rho}\left[\frac{\partial\left(\rho E_\phi\right)}{\partial \rho}\right]\right\} - \omega^2 \epsilon_\phi \mu_\rho E_\phi = i\omega \mu_\rho I_e \delta(\rho - \rho')\delta(z - z'), \tag{3-24}$$

which can be rearranged as

$$\left[\left(\frac{\mu_\rho}{\mu_z}\right)\frac{\partial}{\partial\rho}\frac{1}{\rho}\frac{\partial}{\partial\rho}\rho+\frac{\partial^2}{\partial z^2}+k^2\right]E_\phi=-i\omega\mu_\rho I_e\delta(\rho-\rho')\delta(z-z'), \tag{3-25}$$

where k is defined as

$$k=\pm\omega\sqrt{\epsilon_\phi\mu_\rho}. \tag{3-26}$$

Similarly, from the duality principle, if the source is now a magnetic current loop, $\mathbf{J}_m$ has only a ϕ-component and (3-19) gives

$$\left[\left(\frac{\epsilon_\rho}{\epsilon_z}\right)\frac{\partial}{\partial\rho}\frac{1}{\rho}\frac{\partial}{\partial\rho}\rho+\frac{\partial^2}{\partial z^2}+k^2\right]H_\phi=-i\omega\epsilon_\rho I_m\delta(\rho-\rho')\delta(z-z'), \tag{3-27}$$

where I_m is the uniform and azimuthally independent magnetic current distribution, and k is defined as

$$k=\pm\omega\sqrt{\epsilon_\rho\mu_\phi}. \tag{3-28}$$

Equations (3-25) and (3-27) can be recast into a simplified form by using

$$\left[\left(\frac{p_\rho}{p_z}\right)\frac{\partial}{\partial\rho}\frac{1}{\rho}\frac{\partial}{\partial\rho}\rho+\frac{\partial^2}{\partial z}+k^2\right]A_\phi=-i\omega p_\rho I\delta(\rho-\rho')\delta(z-z'), \tag{3-29}$$

where $A_\phi=E_\phi$, $p=\mu$, $I=I_e$ and k as in (3-26) for the electric current loop excitation. In contrast, $A_\phi=H_\phi$, $p=\epsilon$, $I=I_m$, and k as in (3-28) for the magnetic current loop.

3.4.1 Azimuthal Field Components

In order to obtain the solution of (3-29), first it will be analyzed the electromagnetic fields in the source-free regions, where (3-29) becomes an ordinary homogeneous Helmholtz equation, i.e.,

$$\left[\left(\frac{p_\rho}{p_z}\right)\frac{\partial}{\partial\rho}\frac{1}{\rho}\frac{\partial}{\partial\rho}\rho+\frac{\partial^2}{\partial z}+k^2\right]A_\phi=0. \tag{3-30}$$

The method of separation of variables can then be used to solve such differential equation in cylindrical coordinates [48]. In this method it is assumed that a function of independent variables can be expressed as a product of independent functions of each variable, each of which depends on one variable only. As a result, the solution for A_ϕ may be expressed in the form of

$$A_\phi(\rho,z)=R(\rho)Z(z). \tag{3-31}$$

After substitution the above into (3-30), replacing the partials derivatives by ordinary ones, and dividing the result by A_ϕ, yields

$$\left(\frac{p_\rho}{p_z}\right)\frac{1}{R}\frac{d}{d\rho}\frac{1}{\rho}\frac{d}{d\rho}(\rho R)+\frac{1}{Z}\frac{d^2Z}{dz^2}+k^2=0. \tag{3-32}$$

By noting that the second term in the above equation is independent of ρ, it must be also independent of z in order to (3-32) sum zero for all ρ and z. Hence,

$$\frac{1}{Z}\frac{d^2Z}{dz^2}=-k_z^2, \tag{3-33}$$

where k_z is a constant and the minus sign is chosen only for convenience in the resulting solutions. A typical solution to (3-33) can take the form of a linear combination of traveling waves

$$Z=h(k_z z)=A_1e^{ik_z(z-z')}+A_2e^{-ik_z(z-z')}, \tag{3-34}$$

where A_1 and A_2 represent the amplitude of a wave that travel in the $+z$ and $-z$ directions, respectively, and such constants will be determined latter by matching the boundary conditions (BCs) at the source.

Substituting (3-33) into (3-32), results in an equation with only ρ-dependence, which, after some manipulation, yields

$$\rho^2\frac{d^2R}{d\rho^2}+\rho\frac{dR}{d\rho}+[(k_\rho\rho)^2-1]R=0, \tag{3-35}$$

where

$$k_\rho^2=\left(\frac{p_z}{p_\rho}\right)\left(k^2-k_z^2\right). \tag{3-36}$$

Equation (3-35) is recognized as a first order Bessel differential equation, which solutions are in general, a linear superposition of any two of Bessel and Hankel function of first and second kind: $\mathrm{J}_1(k_\rho\rho)$ and $\mathrm{Y}_1(k_\rho\rho)$, and $\mathrm{H}_1^{(1)}(k_\rho\rho)$ and $\mathrm{H}_1^{(2)}(k_\rho\rho)$. The most appropriate choice will depend on the problem BCs.

For the analyzed cases through this work, the radial wave functions will take the form of

$$R=\hat{F}_1(k_\rho\rho)=\frac{J_1(k_\rho\rho)+BY_1(k_\rho\rho)}{\sqrt{1+B^2}}, \tag{3-37}$$

where B will be specified according to the radial boundary conditions. Thus, (3-31) can be rewritten as

$$\begin{aligned}A_\phi&=\hat{F}_1(k_\rho\rho)h(k_z z)\\&=\left[\frac{J_1(k_\rho\rho)+BY_1(k_\rho\rho)}{\sqrt{1+B^2}}\right]\left[A_1e^{ik_z(z-z')}+A_2e^{-ik_z(z-z')}\right].\end{aligned} \tag{3-38}$$

Linear combinations of the above wave function are also solutions to the Helmholtz equation (3-30). More general solutions can be constructed by summing over all possible values (eigenvalues or characteristics values) of k_ρ (or k_z), i.e.,

$$A_\phi = \sum_{k_\rho} C_{k_\rho} \hat{F}_1(k_\rho \rho) h(k_z z), \tag{3-39}$$

which represents the solutions to the guided modal fields. The amplitude constants C_{k_ρ} can be evaluated when applying the boundary conditions. It is important to note that due to (3-36) only one of the k_i ($i = \{\rho, z\}$) may be chosen independently. Elementary wave functions corresponding to specified eigenvalues are called eigenfunctions [48].

For some electromagnetic problems, the finite number of discrete eigen-solutions of guided modes in (3-39) may not represent the complete solution, and continuum radiated modes must be also included. This wave functions can be constructed by integrating (3-38) in terms of k_ρ (or k_z) over any contour in the complex plane. Therefore, a complete solution to the Helmholtz equation can be expressed as

$$A_\phi = \int_{k_\rho} dk_\rho \; g(k_\rho) \hat{F}_1(k_\rho \rho) h(k_z z), \tag{3-40}$$

where $g(k_\rho)$ is an analytic function and can be determined by enforcing the boundary conditions at the source. The above equation exhibits a continuous variation of the separation parameter, an then there exists a continuous spectrum of eigenvalues.

Solutions for finite regions, as waveguides or cavities, may be characterized by discrete spectra of eigenvalues, while solutions for unbounded regions, like antennas, often require continuous spectra [48]. Accordingly, the adopted solution for the electromagnetic field produced by an azimuthally symmetric electric or magnetic current loop will be the one expressed in (3-40).

3.4.1.1 Construction of the Complete Solution

The solution in (3-40) allows to find the field vectors **E** and **H** as long as the field quantities are single-value, bounded, and possess continuous distributions. Along boundaries where the media exhibit discontinuities in electric or magnetic properties (or there exist sources along the boundaries), the normal field components are also discontinuous and their behaviors across the boundaries are governed by the boundary conditions [49].

In order to determine the complete solution for the azimuthal fields, it is necessary to analyze the field behavior in the near-source region. To achieve this, it can be thought as if the source is located in the interface between two media which have the same electromagnetic properties, in $z = z'$, as depicted in Fig. 3.6.

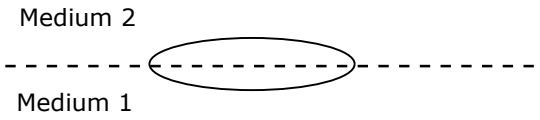

Figure 3.6: Source located in the interface between two media.

When electric or magnetic sources exist along the interface between two media, with neither one being a perfect conductor the boundary conditions on the tangential components of the fields can be written, in general form, as

$$\hat{n} \times \mathbf{E}_2 - \hat{n} \times \mathbf{E}_1 = -\mathbf{J}_{m,s}, \tag{3-41}$$

$$\hat{n} \times \mathbf{H}_2 - \hat{n} \times \mathbf{H}_1 = \mathbf{J}_{e,s}, \tag{3-42}$$

where $\hat{n}$ is a vector normal to the interface between medium 1 and medium 2 ($\hat{n} = \hat{i}_z$).

Equation (3-41) states that the tangential components of the electric field across an interface between two media, along which there exists a surface magnetic current density $J_{m,s}$, are discontinuous by an amount equal to the magnetic current density. On the other hand, equation (3-42) states that the tangential components of the magnetic field across an interface between two media, along which there exists a surface electric current density $J_{e,s}$, are discontinuous by an amount equal to the electric current density [49].

The vector equations (3-41) and (3-42) can be expanded as

$$E_{2\phi} - E_{1\phi} = +J_{m,\rho}, \tag{3-43}$$

$$E_{2\rho} - E_{1\rho} = -J_{m,\phi}, \tag{3-44}$$

$$H_{2\phi} - H_{1\phi} = -J_{e,\rho}, \tag{3-45}$$

$$H_{2\rho} - H_{1\rho} = +J_{e,\phi}. \tag{3-46}$$

If the transmission antenna is an electric current loop which impressed surface electric current density in the ϕ-direction, the only field that is discontinuous at the interface is H_ρ, while the other remaining field components are continuous. Under this specification,

$$E_{2\phi} - E_{1\phi} = 0. \tag{3-47}$$

Taking the solution for the electric field of (3-40), and then substituting into the above equation, results in

$$\int_{k_\rho} dk_\rho\, g(k_\rho)\hat{F}_1(k_\rho\rho)A_1\, e^{ik_z(z-z')}\Big|_{z=z'} - \int_{k_\rho} dk_\rho\, g(k_\rho)\hat{F}_1(k_\rho\rho)A_2\, e^{-ik_z(z-z')}\Big|_{z=z'} = 0. \tag{3-48}$$

At $z = z'$, the exponential function in both terms vanishes. If the integration of both terms is taken over the same complex contour, the previous equation can be reduced to

$$\int_{k_\rho} dk_\rho\; g(k_\rho)\hat{F}_1(k_\rho\rho)(A_1 - A_2) = 0. \tag{3-49}$$

In order to satisfy last equation for all ρ, the amplitude constants A_1 and A_2 must be set equals. As a consequence, $h(k_z z)$ can be arranged in a more compact form

$$h(k_z z) = A\; e^{ik_z|z-z'|}. \tag{3-50}$$

The previous definition allows to rewrite (3-40) as

$$A_\phi = \int_{k_\rho} dk_\rho\; g_s(k_\rho)\hat{F}_1(k_\rho\rho)\; e^{ik_z|z-z'|} \tag{3-51}$$

where $g_s(k_\rho) = g(k_\rho)A$.

In order to determine the coefficient $g(k_\rho)$, the magnetic field boundary condition (3-46) was enforced. The H_ρ component can be easily found by projecting (3-1) into $\hat{i}_\phi$, i.e.:

$$\frac{1}{\rho}\frac{\partial E_z}{\partial \phi} - \frac{\partial E_\phi}{\partial z} = i\omega\mu_\rho H_\rho - J_{m,\rho}, \tag{3-52}$$

As a result of $\partial/\partial\phi = 0$, the above can be simplified to

$$H_\rho = -(i\omega\mu_\rho)^{-1}\frac{\partial E_\phi}{\partial z}. \tag{3-53}$$

Now, by using (3-53) into (3-46) it is obtained

$$-(i\omega\mu_\rho)^{-1}\frac{\partial E_{2\phi}}{\partial z} + (i\omega\mu_\rho)^{-1}\frac{\partial E_{1\phi}}{\partial z} = +J_{e,\phi}, \tag{3-54}$$

a function that only depends on E_ϕ with $J_{e,\phi}$ described by (3-20) for a uniform and azimuthally independent current distribution. Then, substituting (3-40) into the previous equation yields

$$\begin{aligned} &-(i\omega\mu_\rho)^{-1}\frac{\partial}{\partial z}\int_{k_\rho} dk_\rho\; g_s(k_\rho)\hat{F}_1(k_\rho\rho)\; e^{ik_z(z-z')}\Big|_{z=z'} \\ &+(i\omega\mu_\rho)^{-1}\frac{\partial}{\partial z}\int_{k_\rho} dk_\rho\; g_s(k_\rho)\hat{F}_1(k_\rho\rho)\; e^{-ik_z(z-z')}\Big|_{z=z'} = I_e\;\delta(\rho-\rho')\delta(z-z'). \end{aligned} \tag{3-55}$$

The partial derivative in z of both terms commutes with the integral, and then

$$- (i\omega\mu_\rho)^{-1} \int_{k_\rho} dk_\rho \; g_s(k_\rho)\hat{F}_1(k_\rho\rho)(ik_z)e^{ik_z(z-z')}\Big|_{z=z'}$$
$$+ (i\omega\mu_\rho)^{-1} \int_{k_\rho} dk_\rho \; g_s(k_\rho)\hat{F}_1(k_\rho\rho)(-ik_z)e^{-ik_z(z-z')}\Big|_{z=z'} = I_e \; \delta(\rho-\rho')\delta(z-z'). \tag{3-56}$$

Evaluating both sides of the above equation for $z = z'$, it can be reduced to

$$-2(ik_z)(i\omega\mu_\rho)^{-1} \int_{k_\rho} dk_\rho \; g_s(k_\rho) \; \hat{F}_1(k_\rho\rho) = I_e \; \delta(\rho-\rho'), \tag{3-57}$$

and, after some manipulations, to the compact expression

$$\int_{k_\rho} dk_\rho \; g_s(k_\rho)\hat{F}_1(k_\rho\rho) = -\frac{\omega\mu_\rho}{2k_z} I_e \delta(\rho-\rho'). \tag{3-58}$$

To determine $g_s(k_\rho)$, it would be taken advantage of the orthogonality of Bessel functions [50] by using the solution form presented in Appendix A:

$$\int_0^\infty dk_\rho \; \rho' k_\rho \hat{B}_n(k_\rho\rho)\hat{B}_n(k_\rho\rho') = \delta(\rho-\rho'), \tag{3-59}$$

where $\hat{B}_n(k_\rho\rho)$ must be a normalized combination of Bessel functions of integer order n. In short, the Dirac delta can be expressed as an integral in terms of the radial propagation constant k_ρ. Using the above expression in the right-hand side (RHS) of (3-58) yields

$$\int_{k_\rho} dk_\rho \; g_s(k_\rho)\hat{F}_1(k_\rho\rho) = -\frac{\omega\mu_\rho}{2k_z} I_e \int_0^\infty dk_\rho\rho' \; k_\rho \hat{B}_n(k_\rho\rho)\hat{B}_n(k_\rho\rho'). \tag{3-60}$$

It can be appreciated that both sides of the last equation have a similar format. By virtue of which the equation (3-59) is valid for $\hat{B}_n(\cdot)$ being a combination of Bessel functions, consequently, it must also be valid for a radial function with the format specified by (3-37). Furthermore, when taking the integral in the left-hand side (LHS) of (3-60) from 0 to ∞, it is obtained

$$\int_0^\infty dk_\rho \; g_s(k_\rho)\hat{F}_1(k_\rho\rho) = -\frac{\omega\mu_\rho}{2k_z} I_e \int_0^\infty dk_\rho\rho' \; k_\rho \hat{F}_1(k_\rho\rho)\hat{F}_1(k_\rho\rho'). \tag{3-61}$$

By matching the arguments of the above equation, it can be determined the coefficient $g_s(k_\rho)$ as

$$g_s(k_\rho) = -\frac{\omega\mu_\rho\rho'}{2k_z} I_e k_\rho \hat{F}_1(k_\rho\rho'). \tag{3-62}$$

Once $g_s(k_\rho)$ is found, the complete solution for the azimuthal electric field component, E_ϕ, can be expressed as

$$E_\phi = -\frac{\omega\mu_\rho\rho' I_e}{2} \int_0^\infty dk_\rho \frac{k_\rho}{k_z} \hat{F}_1(k_\rho\rho)\hat{F}_1(k_\rho\rho')e^{ik_z|z-z'|}, \tag{3-63}$$

Using the same procedure, the solution for the magnetic field produced by a uniform and azimuthally independent magnetic current loop is given by the dual equation

$$H_\phi = -\frac{\omega\epsilon_\rho\rho' I_m}{2}\int_0^\infty dk_\rho \frac{k_\rho}{k_z}\hat{F}_1(k_\rho\rho)\hat{F}_1(k_\rho\rho')e^{ik_z|z-z'|}. \tag{3-64}$$

Equations (3-63) and (3-64) can be recast as the unified form

$$A_\phi = -\frac{\omega p_\rho\rho' I}{2}\int_0^\infty dk_\rho \frac{k_\rho}{k_z}\hat{F}_1(k_\rho\rho)\hat{F}_1(k_\rho\rho')e^{ik_z|z-z'|}, \tag{3-65}$$

$$k_z = \pm\sqrt{k^2 - \left(\frac{p_\rho}{p_z}\right)k_\rho^2}, \tag{3-66}$$

$$k = \pm\,\omega\sqrt{p_\rho q_\phi}. \tag{3-67}$$

where $\hat{F}_1(k_\rho\rho)$ is defined as in (3-37), and $A_\phi = E_\phi$, $p = \mu$, $q = \epsilon$, and $I = I_e$ is the electric current associated with the electric current loop. In contrast, $A_\phi = H_\phi$, $p = \epsilon$, $q = \mu$, and $I = I_m$ is the magnetic current associated with the magnetic current loop. For isotropic media, this solution corresponds with the well-known form [33].

So far, the boundary condition (3-43) and (3-46) has been accomplished for electric loop antenna, whereas (3-44) and (3-45) for the magnetic loop antenna. In order to guarantee the consistence of the proposed solution, all boundary conditions must be satisfied independent of the source kind. For this purpose, it is mandatory to determinate the other field components transversal to $\hat{i}_\phi$.

3.4.2 Radial and Axial Field Components

By using (3-1) and (3-2), and projecting them into $\hat{i}_\rho$, $\hat{i}_\phi$, and $\hat{i}_z$, respectively, results in

$$\frac{1}{\rho}\frac{\partial E_z}{\partial\phi} - \frac{\partial E_\phi}{\partial z} = i\omega\mu_\rho H_\rho - J_{m,\rho}, \tag{3-68}$$

$$\frac{\partial E_\rho}{\partial z} - \frac{\partial E_z}{\partial\rho} = i\omega\mu_\phi H_\phi - J_{m,\phi}, \tag{3-69}$$

$$\frac{1}{\rho}\left[\frac{\partial}{\partial\rho}(\rho E_\phi) - \frac{\partial E_\rho}{\partial\phi}\right] = i\omega\mu_z H_z - J_{m,z}, \tag{3-70}$$

$$\frac{1}{\rho}\frac{\partial H_z}{\partial \phi} - \frac{\partial H_\phi}{\partial z} = -i\omega\epsilon_\rho E_\rho - J_{e,\rho}, \tag{3-71}$$

$$\frac{\partial H_\rho}{\partial z} - \frac{\partial H_z}{\partial \rho} = -i\omega\epsilon_\phi E_\phi - J_{e,\phi}, \tag{3-72}$$

$$\frac{1}{\rho}\left[\frac{\partial}{\partial \rho}(\rho H_\phi) - \frac{\partial H_\rho}{\partial \phi}\right] = -i\omega\epsilon_z E_z - J_{e,z}. \tag{3-73}$$

When the current density $\mathbf{J}_e$ and $\mathbf{J}_m$ have only $\hat{\phi}$-component and $\partial/\partial\phi = 0$, equations (3-68) to (3-73) reduce to

$$-\frac{\partial E_\phi}{\partial z} = i\omega\mu_\rho H_\rho, \tag{3-74}$$

$$\frac{\partial E_\rho}{\partial z} - \frac{\partial E_z}{\partial \rho} = i\omega\mu_\phi H_\phi - J_{m,\phi}, \tag{3-75}$$

$$\frac{1}{\rho}\frac{\partial}{\partial \rho}(\rho E_\phi) = i\omega\mu_z H_z, \tag{3-76}$$

$$-\frac{\partial H_\phi}{\partial z} = -i\omega\epsilon_\rho E_\rho, \tag{3-77}$$

$$\frac{\partial H_\rho}{\partial z} - \frac{\partial H_z}{\partial \rho} = -i\omega\epsilon_\phi E_\phi - J_{e,\phi}, \tag{3-78}$$

$$\frac{1}{\rho}\frac{\partial}{\partial \rho}(\rho H_\phi) = -i\omega\epsilon_z E_z. \tag{3-79}$$

For the radiation of an electric current loop (i.e., $J_{e,\phi} \neq 0$ and $J_{m,\phi} = 0$), once E_ϕ is determined by (3-65), H_ρ can be found using (3-53) and H_z by manipulating (3-76) as

$$H_z = (i\omega\mu_z)^{-1}\frac{1}{\rho}\frac{\partial}{\partial \rho}(\rho E_\phi). \tag{3-80}$$

The other components cannot be found from the solution to (3-65), however, expressing the E_ρ and E_z of equations (3-77) and (3-79), respectively, in terms of H_ϕ as follows,

$$E_\rho = (i\omega\epsilon_\rho)^{-1}\frac{\partial H_\phi}{\partial z}, \tag{3-81}$$

$$E_z = -(i\omega\epsilon_z)^{-1}\frac{1}{\rho}\frac{\partial}{\partial \rho}(\rho H_\phi), \tag{3-82}$$

and then, using the above equations into (3-75)

$$(i\omega\epsilon_\rho)^{-1}\frac{\partial^2 H_\phi}{\partial z^2} + (i\omega\epsilon_z)^{-1}\frac{\partial}{\partial \rho}\frac{1}{\rho}\frac{\partial}{\partial \rho}(\rho H_\phi) = i\omega\mu_\phi H_\phi, \tag{3-83}$$

it is obtained a decoupled second-order partial differential equation for the H_ϕ component.

After some manipulations, equation (3-83) can be rewritten as

$$\left[\left(\frac{\epsilon_\rho}{\epsilon_z}\right)\frac{\partial}{\partial\rho}\frac{1}{\rho}\frac{\partial}{\partial\rho}\rho+\frac{\partial^2}{\partial z}+k^2\right]H_\phi=0, \tag{3-84}$$

where $k=\sqrt{\omega^2\epsilon_\rho\mu_\phi}$. This equation is a homogeneous Helmholtz equation for H_ϕ in a source-free region, and likewise in (3-29), its solution will take the form of (3-40).

The application of the boundary conditions (3-45) and (3-44) at $z=z'$ of the result of (3-84) leads to a null H_ϕ, and as a consequence, the other dependent components must vanish too. This is summarized by

$$\begin{aligned} H_\phi &= 0, \\ E_\rho &= 0, \\ E_z &= 0, \end{aligned} \tag{3-85}$$

which indicates that the solution found determinates a transversal electric wave to the z direction (TE^z). From (3-85) it can be inferred that the field generated by the electric loop will induce an $\mathbf{E}$ field in the azimuthal direction inside the conducting formation.

It is important to note that due to $H_\phi = E_\rho = 0$, the boundary conditions in (3-45) and (3-44) are automatically satisfied, which shows that the solution for (3-63) is consistent.

Similarly, for the radiation of a magnetic current loop (i.e., $J_{m,\phi} \neq 0$ and $J_{e,\phi} = 0$), once H_ϕ is determined by (3-27), the field components E_ρ and E_z can be determined using (3-81) and (3-82), respectively. The other field components can be found by using the equations dual to (3-85), where

$$\begin{aligned} E_\phi &= 0, \\ H_\rho &= 0, \\ H_z &= 0, \end{aligned} \tag{3-86}$$

which indicates that the solution found above is a transversal magnetic wave to the z direction (TM^z). As a result of (3-86), the boundary conditions (3-43) and (3-46) are automatically satisfied, which shows that the solution (3-64) is consistent.

The axial electric and magnetic field components for both TM^z and TE^z scenarios, can be obtained from equations (3-80) and (3-82). It can also be observed that they both have the same differentiation structure given by

$$\frac{1}{\rho}\frac{\partial}{\partial\rho}(\rho A_\phi), \tag{3-87}$$

where $A=\{E,H\}$. The above can in addition be expanded into

$$\frac{1}{\rho}\frac{\partial}{\partial\rho}(\rho A_\phi)=\frac{A_\phi}{\rho}+\frac{\partial A_\phi}{\partial\rho}. \tag{3-88}$$

The only ρ-dependent term into (3-65) is $\hat{F}_1(k_\rho\rho)$. As a consequence, the differentiation in (3-88) can commute with the integration in (3-65). Then, it is useful to write

$$\frac{1}{\rho}\frac{\partial}{\partial\rho}(\rho A_{\phi_\rho}) = \frac{\hat{F}_1(k_\rho\rho)}{\rho} + \frac{\partial\hat{F}_1(k_\rho\rho)}{\partial\rho}. \tag{3-89}$$

Then, substituting (3-37) into the above equation, results in

$$\frac{1}{\rho}\frac{\partial}{\partial\rho}(\rho A_{\phi_\rho}) = \frac{1}{\rho}\frac{J_1(k_\rho\rho)+BY_1(k_\rho\rho)}{\sqrt{1+B^2}} + \frac{\partial}{\partial\rho}\left[\frac{J_1(k_\rho\rho)+BY_1(k_\rho\rho)}{\sqrt{1+B^2}}\right], \tag{3-90}$$

The coefficient B does not depend on ρ, then it can be extracted from the derivative, and the above turns

$$\frac{1}{\rho}\frac{\partial}{\partial\rho}(\rho A_{\phi_\rho}) = \frac{1}{\sqrt{1+B^2}}\left[\frac{J_1(k_\rho\rho)}{\rho} + B\frac{Y_1(k_\rho\rho)}{\rho} + \frac{\partial}{\partial\rho}J_1(k_\rho\rho) + B\frac{\partial}{\partial\rho}Y_1(k_\rho\rho)\right]. \tag{3-91}$$

The spectral domain parameter k_ρ does not depend on ρ, and because of that, the partial derivatives in the RHS of the last equation can be substitute by its total derivative, and then determined by using the derivative formulas of Bessel equations of [49, Appendix IV]

$$\frac{d}{dx}B_v(\alpha x) = \alpha B_{v-1}(\alpha x) - \frac{v}{x}B_v(\alpha x). \tag{3-92}$$

Using this result on the RHS of (3-91) allows to obtain

$$\begin{aligned}\frac{1}{\rho}\frac{\partial}{\partial\rho}(\rho A_{\phi_\rho}) &= \frac{1}{\sqrt{1+B^2}} \\ &\cdot\left[\frac{J_1(k_\rho\rho)}{\rho} + B\frac{Y_1(k_\rho\rho)}{\rho} + k_\rho J_0(k_\rho\rho) - \frac{J_1(k_\rho\rho)}{\rho} + k_\rho BY_0(k_\rho\rho) - B\frac{Y_1(k_\rho\rho)}{\rho}\right],\end{aligned} \tag{3-93}$$

which reduces to

$$\frac{1}{\rho}\frac{\partial}{\partial\rho}(\rho A_{\phi_\rho}) = \frac{k_\rho}{\sqrt{1+B^2}}\left[J_0(k_\rho\rho)+BY_0(k_\rho\rho)\right], \tag{3-94}$$

The previous result can be substituted into equations (3-80) and (3-82) to find the axial fields

$$E_z = -\frac{i\epsilon_\rho\rho' I_m}{2\epsilon_z}\int_0^\infty dk_\rho\ \frac{k_\rho^2}{k_z}\hat{F}_0(k_\rho\rho)\hat{F}_1(k_\rho\rho')e^{ik_z|z-z'|} \tag{3-95}$$

$$H_z = \frac{i\rho'\mu_\rho I_e}{2\mu_z}\int_0^\infty dk_\rho\ \frac{k_\rho^2}{k_z}\hat{F}_0(k_\rho\rho)\hat{F}_1(k_\rho\rho')e^{ik_z|z-z'|}, \tag{3-96}$$

for TM^z and TE^z, respectively.

To summarize, the electromagnetic field components for the TE^z wave can be expressed as

$$\begin{aligned}
E_\rho &= 0, \\
E_\phi &= -\frac{\omega\mu_\rho\rho' I_e}{2}\int_0^\infty dk_\rho \frac{k_\rho}{k_z}\hat{F}_1(k_\rho\rho)\hat{F}_1(k_\rho\rho')e^{ik_z|z-z'|}, \\
E_z &= 0, \\
H_\rho &= -\frac{i\rho' I_e}{2}\int_0^\infty dk_\rho k_\rho\ \hat{F}_1(k_\rho\rho)\hat{F}_1(k_\rho\rho')\frac{|z|}{z}e^{ik_z|z-z'|}, \\
H_\phi &= 0, \\
H_z &= \frac{i\rho'\mu_\rho I_e}{2\mu_z}\int_0^\infty dk_\rho\ \frac{k_\rho^2}{k_z}\hat{F}_0(k_\rho\rho)\hat{F}_1(k_\rho\rho')e^{ik_z|z-z'|}.
\end{aligned} \tag{3-97}$$

And for the TM^z wave the electromagnetic field components take the form of

$$\begin{aligned}
E_\rho &= \frac{i\rho' I_m}{2}\int_0^\infty dk_\rho k_\rho\ \hat{F}_1(k_\rho\rho)\hat{F}_1(k_\rho\rho')\frac{|z|}{z}e^{ik_z|z-z'|}, \\
E_\phi &= 0, \\
E_z &= -\frac{i\epsilon_\rho\rho' I_m}{2\epsilon_z}\int_0^\infty dk_\rho\ \frac{k_\rho^2}{k_z}\hat{F}_0(k_\rho\rho)\hat{F}_1(k_\rho\rho')e^{ik_z|z-z'|}, \\
H_\rho &= 0, \\
H_\phi &= -\frac{\omega\epsilon_\rho\rho' I_m}{2}\int_0^\infty dk_\rho\frac{k_\rho}{k_z}\hat{F}_1(k_\rho\rho)\hat{F}_1(k_\rho\rho')e^{ik_z|z-z'|}, \\
H_z &= 0.
\end{aligned} \tag{3-98}$$

For both cases

$$\hat{F}_n(k_\rho\rho) = \frac{J_n(k_\rho\rho) + BY_n(k_\rho\rho)}{\sqrt{1+B^2}} \tag{3-99}$$

with $n = \{0, 1\}$, and k and k_z can be determined using (3-67) and (3-66), respectively, for each mode.

3.4.3 Radiation Boundary Condition: A Proper Branch Selection for the Square Root Function

In addition to satisfy the boundary conditions, it is important to guarantee that the electromagnetic field is finite everywhere in the considered domain, and the energy which is radiated from the sources must scatter to infinity.

According to this, the electromagnetic field generated by a current loop within an homogeneous, anisotropic medium, must vanish for large ρ (because there are no sources at infinity). This is naturally satisfied by the radial

functions ($J_1(\rho)$ and $Y_1(\rho)$), which vanish at $\rho \to \infty$. Furthermore, the fields must also be finite at the origin ($\rho = 0$), which it is not satisfied by the Bessel function of second order $Y_1(\rho = 0) \to \infty$ as $\rho \to 0$, and therefore it cannot describe a field. According to this B must be null, and the radial function must be expressed as:

$$\hat{F}_1(k_\rho \rho) = J_1(k_\rho \rho), \tag{3-100}$$

for both electric and magnetic current loop sources.

Furthermore, it must be ensured that the exponential term in (3-65) be limited and must vanish when $|z| \to +\infty$. In order to face this, the square root branch of the complex axial propagation constant k_z in (3-36) must be selected according to the Sommerfeld radiation condition [31]

$$\mathrm{Im}(k_z) > 0, \text{when} \;\; z \to +\infty, \;\text{and} \tag{3-101}$$

$$\mathrm{Im}(k_z) < 0, \text{when} \;\; z \to -\infty. \tag{3-102}$$

3.4.4 Convergence of the Solution

In the previous subsection, the expressions for all the components of the electric and magnetic fields were obtained . As can be seen from (3-97) and (3-98), in order to compute the field quantities, integrals over k_ρ must be calculated. The convergence of the numerical integration plays key influence on the operation speed of the solution.

To accelerate the convergence of the semi-infinite integrals over k_ρ, an adaptive Gauss-Kronrod quadrature algorithm is used. This algorithm attempts to approximate the integral of a scalar-valued function using high-order global adaptive quadrature and default error tolerances, which incorporates less effective points for the integral.

This integral method can be used because the integrand must decay rapidly as the integration variable approaches infinity, which is the case of wave propagation in highly conductive media. Special methods, as the presented in [51], should be used for oscillatory functions on infinite.

3.4.5
Numerical Implementation and Analysis

In this section will be presented some simulation results (via Matlab) obtained using the procedure described in Section 3.4 for isotropic and biaxial anisotropic lossy media excited by an electric or magnetic current loop. These examples are meant to verify and analyze the accuracy of the solution derived previously. The results will be benchmarked against solutions obtained using COMSOL, whose solver uses FEM. Table. 3.1 shows the computer system where all the simulations of this dissertation were performed.

Some simplifications can be done in the implementation as a function of the electrical conductivity of the medium. Fig. 3.7 shows a comparison between the imaginary part of the complex permittivity as a function of the frequency, and the real part for a unitary dielectric constant. As it can be appreciated, for logging devices operating at relatively low frequencies and formations with conductivities greater than 10^{-4} S/m it can be assumed that contributions

System	Red Hat Enterprise Linux Server 7.5
CPU	Intel Xeon(R) Gold 6140 (18 cores)
Processor	2.30 GHz
RAM	314.4 GB

Table 3.1: Computer System Resources.

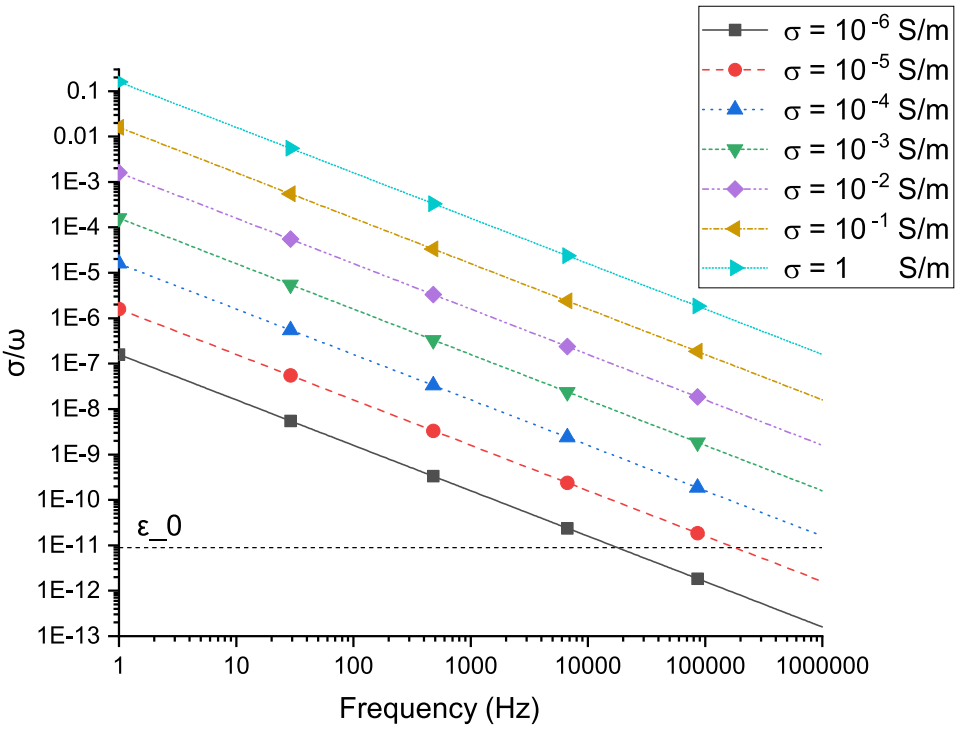

Figure 3.7: Relation between the real and imaginary parts of the permittivity.

from displacement current can be ignored in comparison with the conduction current, which simplify the modeling.

3.4.5.1 Homogeneous Isotropic Formation

First, the source is modeled as a 10-in-radius electric (magnetic) coil at $z = 0$ (where 1 in $= 2.54 \times 10^{-2}$ m) with a constant electric (magnetic) current of 1 A (1 V) placed in a lossy medium described by its electrical conductivity with value 0.5 S/m. The operation frequency for this example is 200 kHz. The relative dielectric and magnetic constants (ϵ_r and μ_r) are unity, i.e., the vacuum dielectric and magnetic constants.

In Fig. 3.8 is plotted the absolute value of azimuthal component of the electrical E_ϕ (magnetic H_ϕ) due to a unit electric (magnetic) current excitation obtained from the solution derived (identified by the label "Matlab") and the obtained with COMSOL. The fields are measured at $\rho = \rho'$ along the axial position.

It can be noticed that there is no considerable difference between the values of the electric field when compared to those of the magnetic field. This was expected as a consequence of the isotropic characteristic of the media,

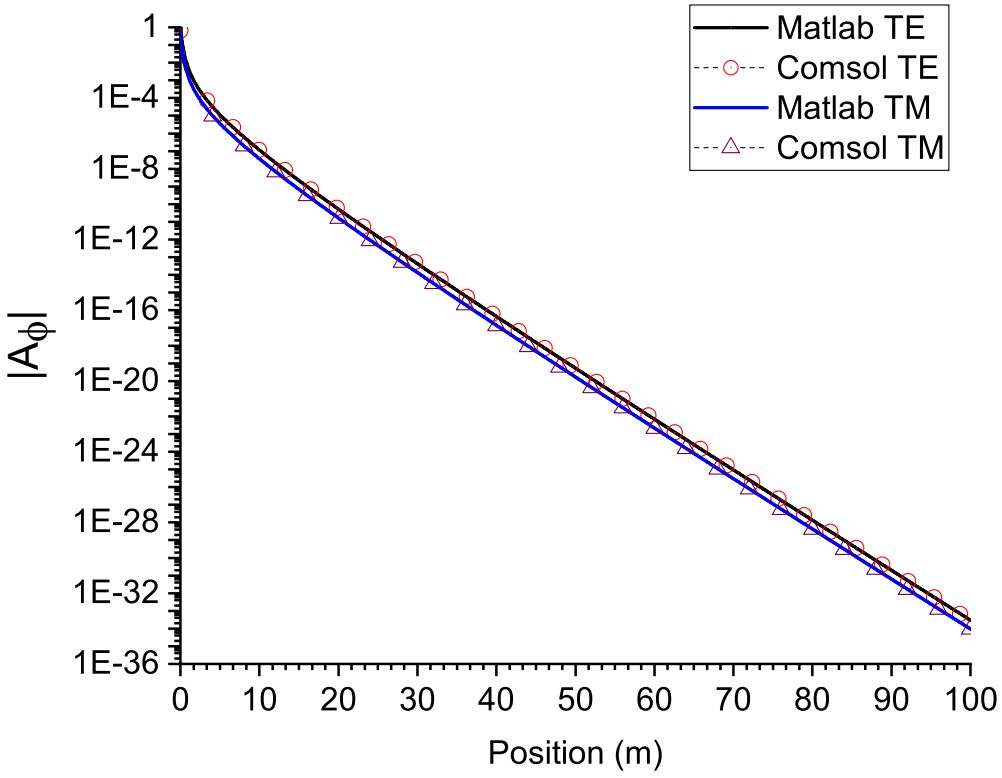

Figure 3.8: Comparison between the absolute values of the azimuthal components of the electric (magnetic) field E_ϕ (H_ϕ) simulated with COMSOL and the obtained values of the derived solution (200 kHz) ($\sigma = 0.5$ S/m).

which causes the value of k in (3-26) and (3-28) to be the same. Therefore the vale of k_z in (3-66) is also the same for both propagations modes. This leads to the same results of the integral term in (3-97) and (3-98), and basically, the main difference in the absolute value is determined by the electrical permittivity and magnetic permeability in front of equations (3-97) and (3-98), respectively.

Also the phase of the different solutions is also dependent of these terms, and it is plotted in Fig. 3.9. The phase difference between the TE^z and TM^z modes is 90°, which is introduced as a consequence of the permittivity be determined mainly by its imaginary part, while the permeability stays as a real value. It is observed that although totally different methods are used, the two results are almost the same, validating the presented solution. The numerical results showed that the achieved solution can accurately model the electromagnetic propagation excited by a azimuthally symmetric magnetic current loop in a conductive media.

Table 3.2 compares the computational costs for COMSOL and the employed solution, from which it can be seen that the provided solution is more computationally efficient. It is important to mention that the solution obtained with COMSOL uses a two-dimensional (2D) axisymmetric modeling, which is less computationally intense when compared with the three-dimensional (3D) model.

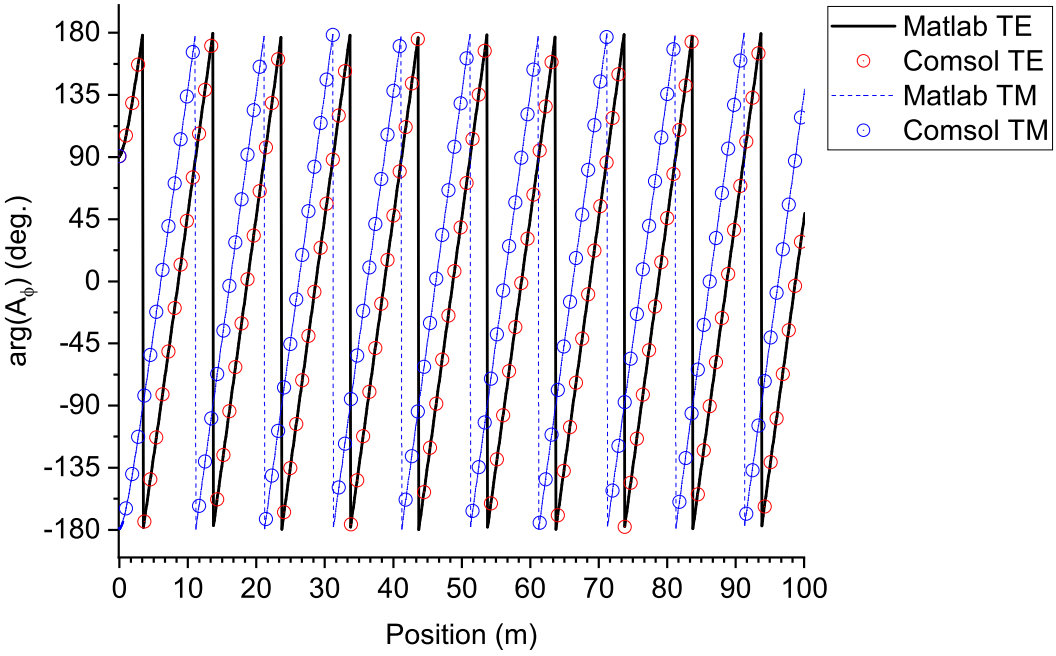

Figure 3.9: Phase values of the azimuthal components of the electric (magnetic) field E_ϕ (H_ϕ) simulated with COMSOL and the obtained values of the derived solution (200 kHz) ($\sigma = 0.5$ S/m).

	Implemented solution	COMSOL
RAM memory	4.4 MB	21.54 GB
CPU time	5.76 s	17.5 s

Table 3.2: Computational costs for modeling a homogeneous isotropic formation.

By defining the *attenuation* as

$$\text{Att(dB)} = -20 \cdot \log_{10} \left| \frac{A(\rho, z)}{A_{\text{source}}} \right|, \tag{3-103}$$

where $A(\rho, z)$ represents the magnetic or electric field as a function of the position and A_{source} is such maximum amplitude near the source at ($\rho = \rho'$, $z \approx 0$), we can analyze the dispersion suffered by an electromagnetic wave as a function of the distance away from the source, as in Fig. 3.10. The wave experiments a severe attenuation as a consequence of the high value of the conductivity and the operation frequency. Also, the values for both modes overlap each other due to the isotropic characteristic of the medium.

One possibility to reduce the attenuation due to propagation, is to increase the radius of the antenna loop, which increase the overall effective area of the antenna. In Fig. 3.11 is presented the behavior of the field as a

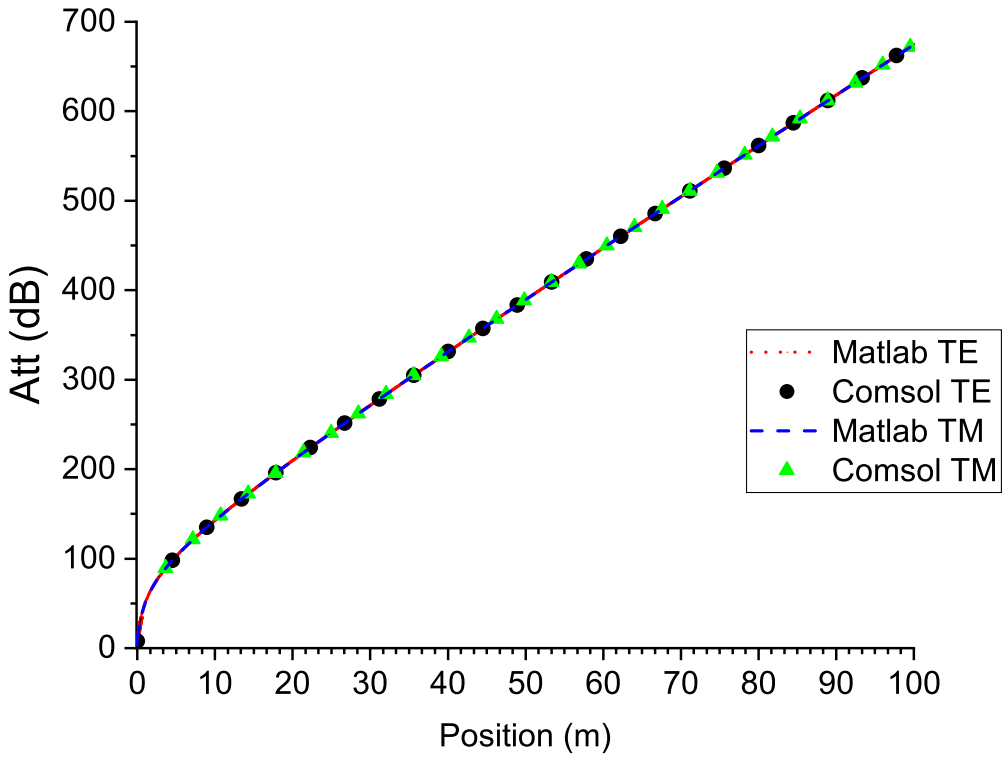

Figure 3.10: Attenuation experimented by the azimuthal component of the electric (magnetic) field E_ϕ (magnetic H_ϕ) as the wave propagates away from the source (200 kHz)($\sigma = 0.5$ S/m).

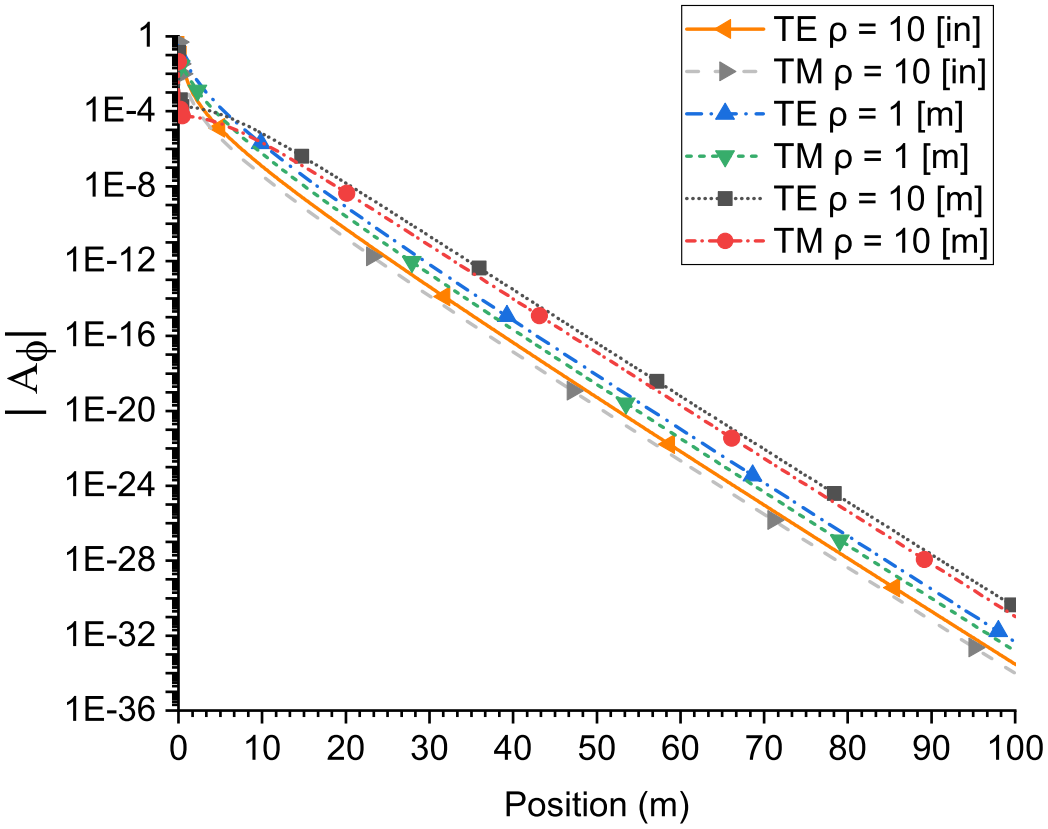

Figure 3.11: Absolute values of the azimuthal components of the electric (magnetic) field E_ϕ (H_ϕ) for different values of the radio of the loop source (200 kHz) ($\sigma = 0.5$ S/m).

function of the radio of the loop antenna. It can be appreciated how the field is less reduced as the radio of the loop source increases. When comparing the attenuation, as in Fig. 3.12, this effect is more noticeable. Going from 1 m to 10 m value for the radio of the loop, the overall attenuation reduces more than 50 dB.

The frequency-dependence of the fields was also investigated. While keeping the radius fixed, a strong impact on the field and the respective attenuation were noticed when varying the frequency. As presented in Fig. 3.13 and Fig. 3.14, the absolute value of the field and its attenuation are inversely proportional to the frequency. It is important to notice that for highest frequency values, the amplitude of the electric field is slightly superior than the magnetic one. But, as the frequency is reduced, the electric field experiments a reduction higher than the magnetic field.

For media with lower values of conductivity, the attenuation behavior (for both modes) as a function of the frequency is shown in Fig. 3.15 and Fig. 3.16. It can be noticed that for frequencies below 1 kHz, the attenuation does not vary so significantly with the frequency when the conductivity of the medium is low (10^{-3} S/m), but as the frequency increases, the attenuation

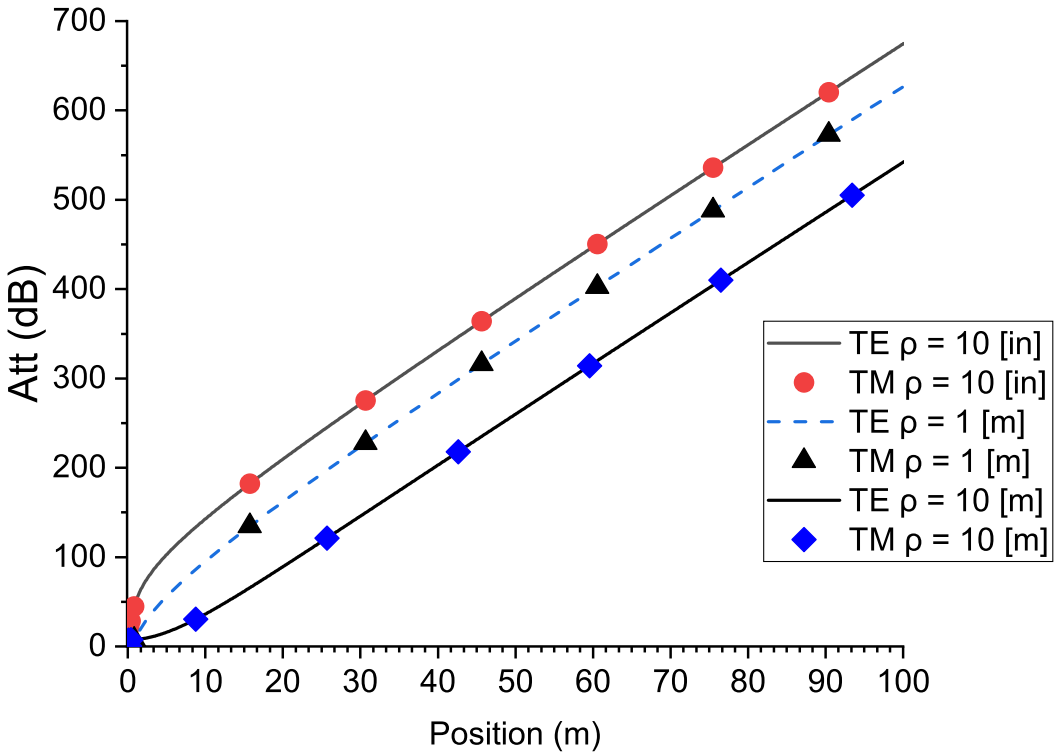

Figure 3.12: Attenuation experimented by the azimuthal components of the electric (magnetic) field E_ϕ (H_ϕ) for different values of the radio of the loop source (200 kHz) ($\sigma = 0.5$ S/m).

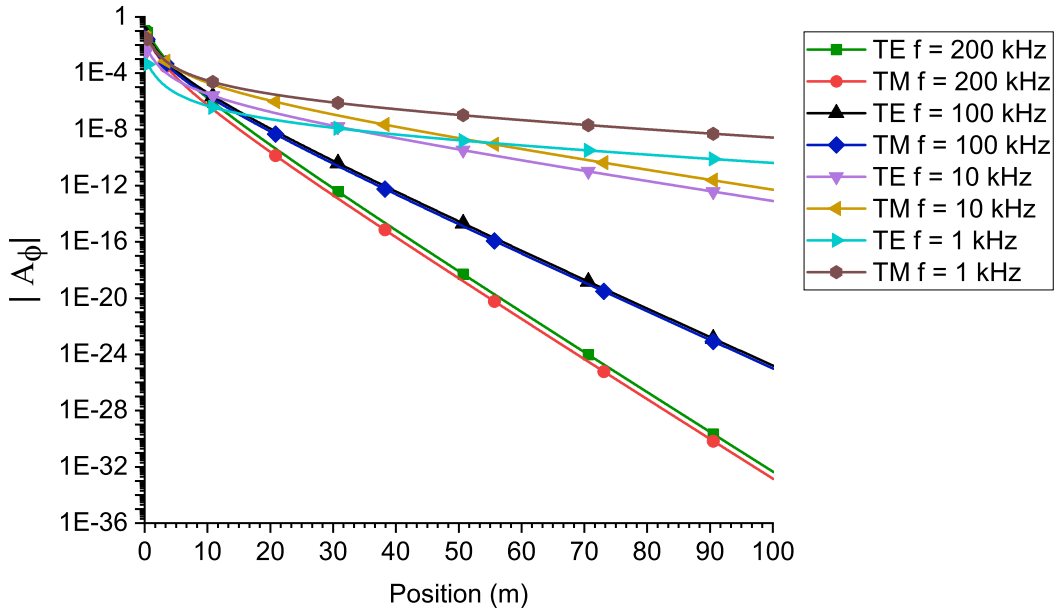

Figure 3.13: Absolute values of the azimuthal components of the electric (magnetic) field E_ϕ (H_ϕ) for different frequency values ($\sigma = 0.5$ S/m).

begins to vary slightly in consequence.

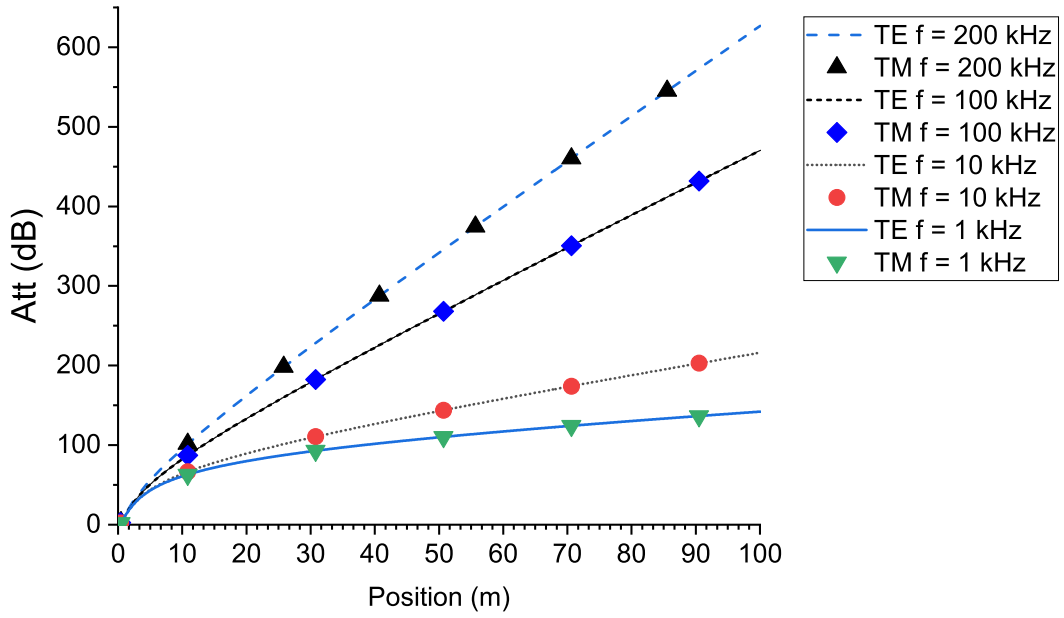

Figure 3.14: Attenuation experimented by the azimuthal component of the electric (magnetic) field E_ϕ (H_ϕ) for different frequency values ($\sigma = 0.5$ S/m).

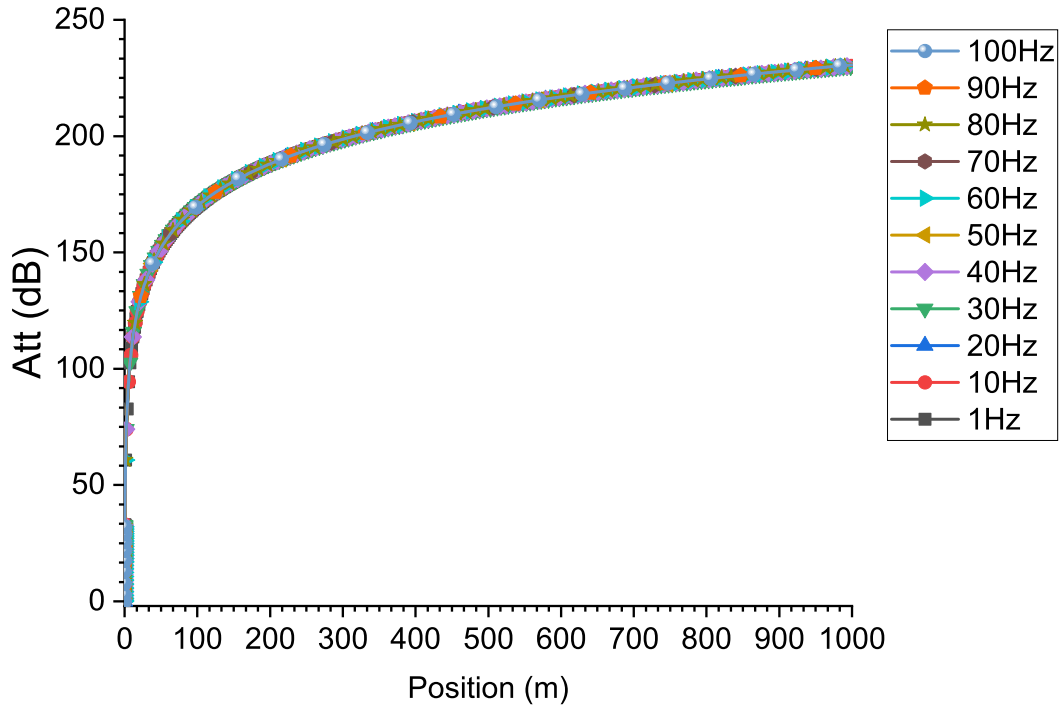

Figure 3.15: Absolute values of the azimuthal components of the electric (magnetic) field E_ϕ (H_ϕ) for different frequency values ($\sigma = 10^{-3}$ S/m).

3.4.5.2 Homogeneous Biaxial Anisotropic Formation

In this section will be analyzed the accuracy of the presented algorithm for anisotropic media. The solutions obtained will be compared with the ones obtained with COMSOL.

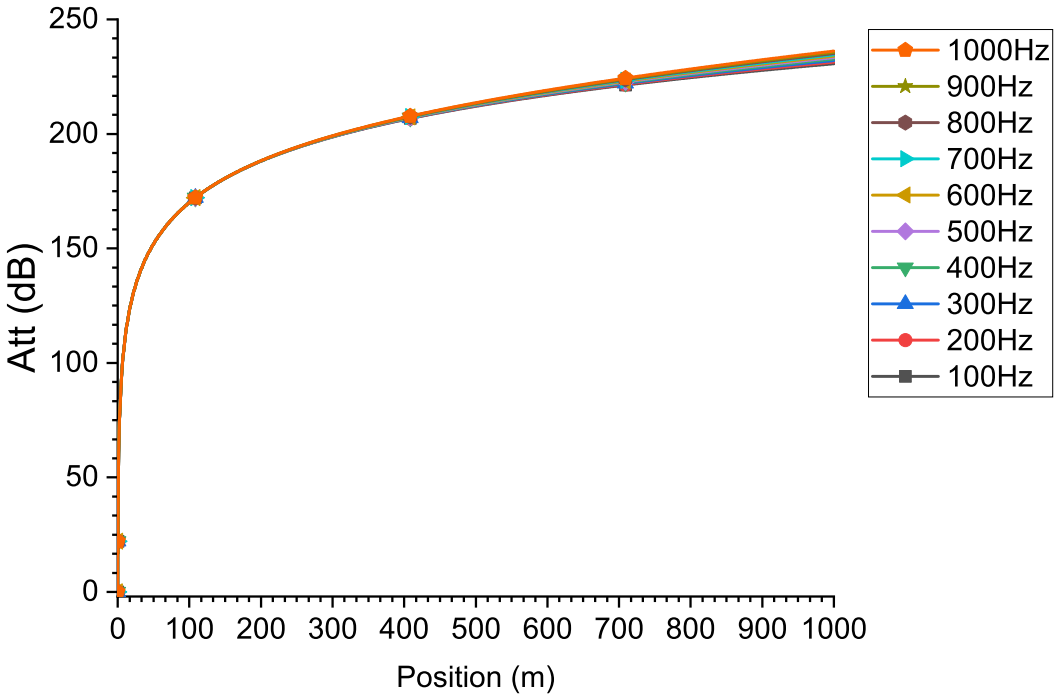

Figure 3.16: Attenuation experimented by the azimuthal component of the electric (magnetic) field E_ϕ (H_ϕ) for different frequency values ($\sigma = 10^{-3}$ S/m).

Consider first a biaxial anisotropic homogeneous medium, which conductivity tensor can be expressed by

$$\bar{\bar{\sigma}} = \begin{bmatrix} \sigma_\rho & 0 & 0 \\ 0 & \sigma_\phi & 0 \\ 0 & 0 & \sigma_z \end{bmatrix} = \begin{bmatrix} 0.5 & 0 & 0 \\ 0 & 0.3 & 0 \\ 0 & 0 & 0.1 \end{bmatrix}. \tag{3-104}$$

The operation frequency for this example is 200 kHz in order to compare with the previous results.

In Fig. 3.17, Fig. 3.18 and Fig. 3.19 are presented the amplitude, phase and attenuation, respectively, of the azimuthal component of the electric (magnetic) field E_ϕ (H_ϕ). Again, the results obtained from the two solutions are almost the same.

In order to analyze the effect of the biaxial anisotropy on the wave propagation, three cases were considered, determined by a permutation of the values in the conductivity tensor, which takes the values of:

$$\bar{\bar{\sigma}}_1 = \begin{bmatrix} 0.5 & 0 & 0 \\ 0 & 0.3 & 0 \\ 0 & 0 & 0.1 \end{bmatrix}, \; \bar{\bar{\sigma}}_2 = \begin{bmatrix} 0.1 & 0 & 0 \\ 0 & 0.5 & 0 \\ 0 & 0 & 0.3 \end{bmatrix}, \; \bar{\bar{\sigma}}_3 = \begin{bmatrix} 0.3 & 0 & 0 \\ 0 & 0.1 & 0 \\ 0 & 0 & 0.5 \end{bmatrix}. \tag{3-105}$$

In Fig. 3.20 is presented the attenuation experimented by the azimuthal component of the electric (magnetic) field E_ϕ (H_ϕ) for different anisotropic configurations and the isotropic case.

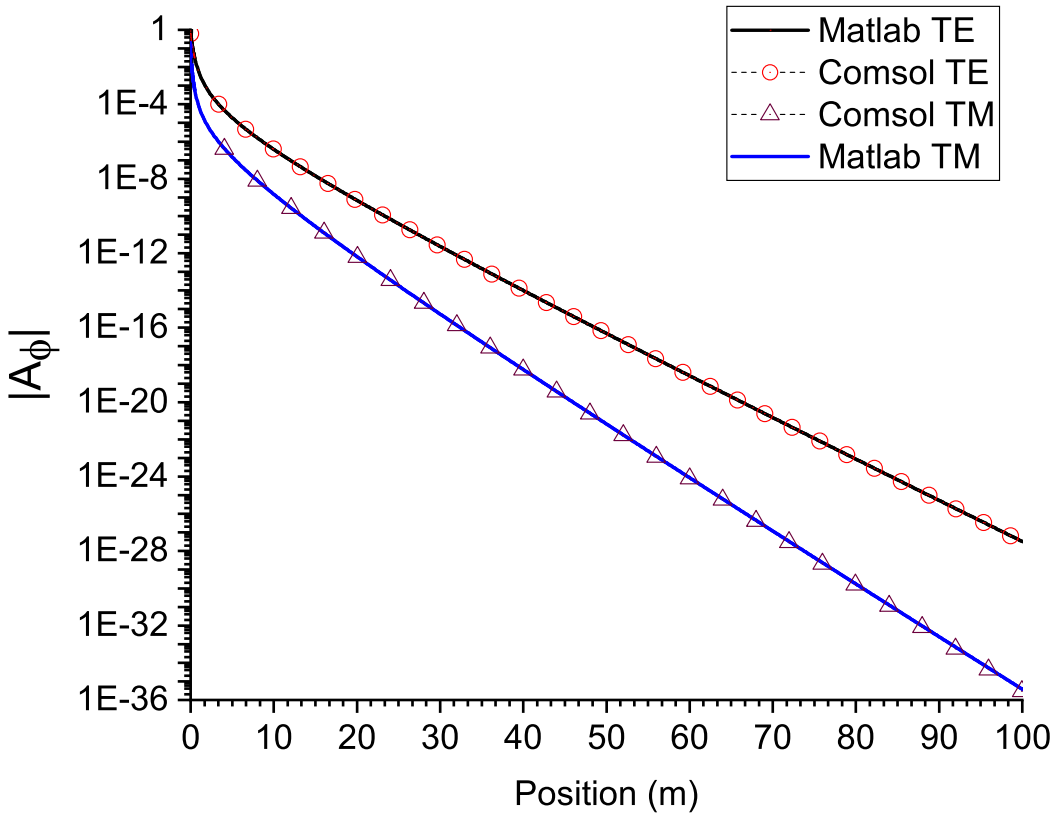

Figure 3.17: Absolute values of the azimuthal components of the electric (magnetic) field E_ϕ (H_ϕ) in an anisotropic formation (200 kHz).

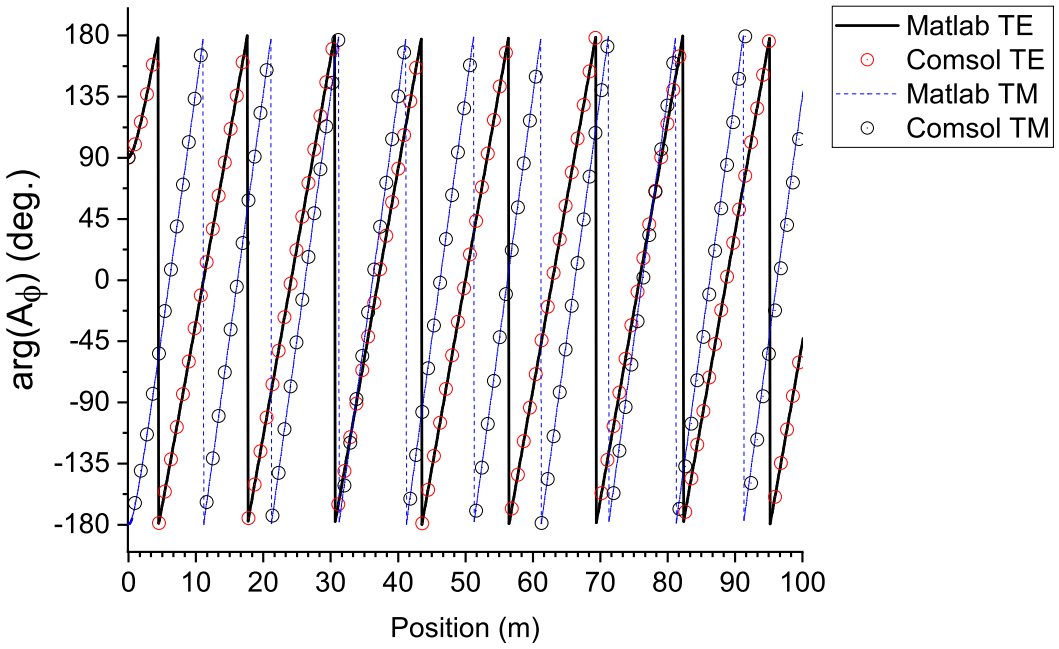

Figure 3.18: Phase values of the azimuthal components of the electric (magnetic) field E_ϕ (H_ϕ) in an anisotropic formation (200 kHz).

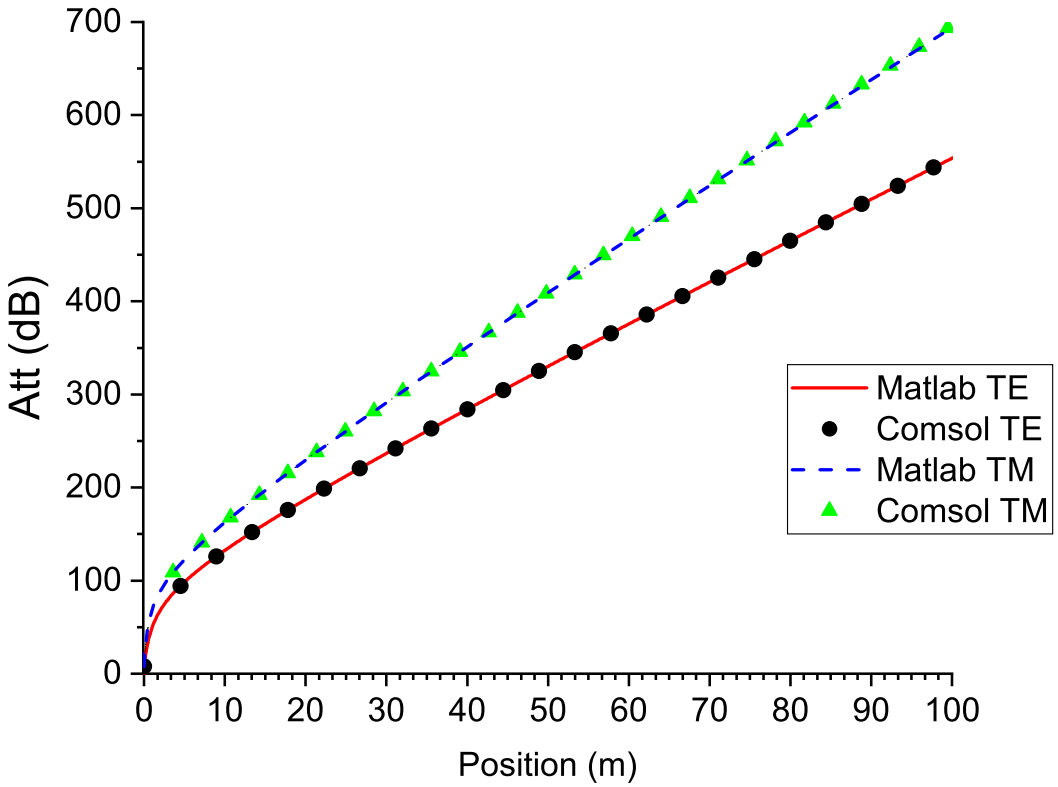

Figure 3.19: Attenuation experimented by the azimuthal components of the electric (magnetic) field E_ϕ (H_ϕ) in an anisotropic formation (200 kHz).

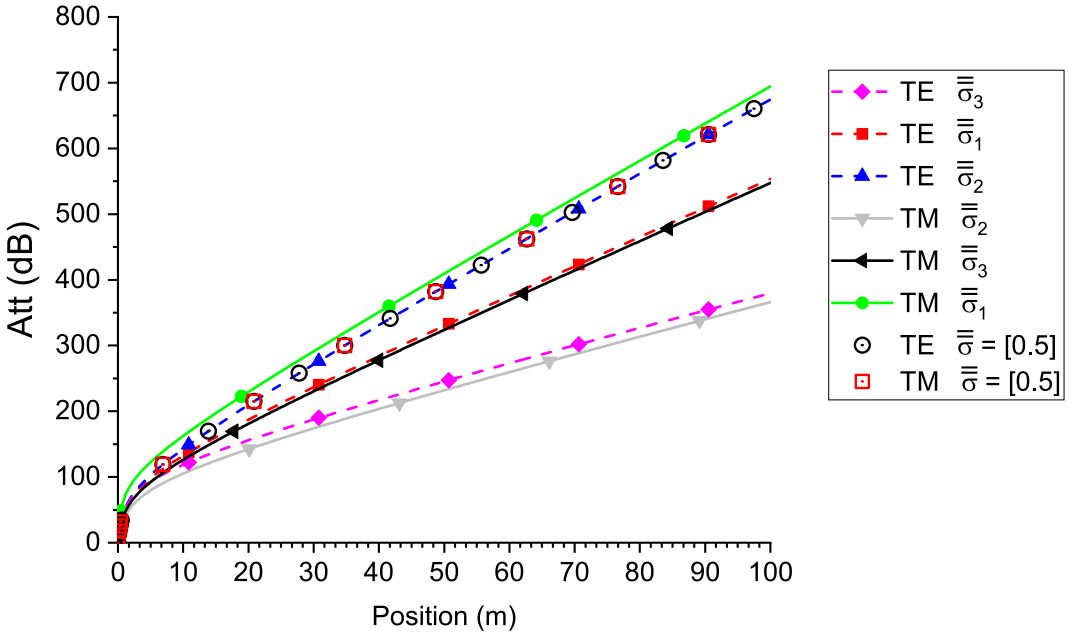

Figure 3.20: Attenuation experimented by the azimuthal component of the electric (magnetic) field E_ϕ (H_ϕ) for different configuration of the anisotropy (200 kHz).

The legend in the Fig. 3.20 is ordered with the smaller attenuation

first, for the respective electromagnetic mode. It can be noticed that for the TE^z mode, the attenuation increases as the azimuthal component of the conductivity increases, with independence of the others components. Similarly, for the TM^z mode, the attenuation increases as the radial component of the conductivity increases, with independence of the others components. This occurs as a consequence of the propagation constant k in (3-26) and (3-28) depends just of the azimuthal and radial component of the conductivity tensor, respectively. When the conductivity component increases, the propagation constant increases, and therefore the attenuation. It is important to note that the attenuation for the TE^z mode with anisotropy described by $\bar{\bar{\sigma}}_2$ is the same as in the isotropic case with conductivity 0.5 S/m. This behavior is due the fact that the only component of the electrical permittivity that is involved in the wave equation for the TE^z is the azimuthal one, the others have no effect on the wave propagation.

3.5 Wave Propagation over the Surface of a Cylindrical Metallic Rod

When the conductivity of the surrounding medium has high values ($\sigma \approx 10^{-3}$ to 1 S/m), the electromagnetic propagation through the soil experiments a strong attenuation. However, the possibility exists that a cylindrical conductor of finite conductivity can act as a guide for electromagnetic waves from the bottom to the surface.

In [52–54] has been explored the propagation of electromagnetic surface waves along a drill stem or metal rod in a conducting host rock. Despite the fact that for oil wells the media around the conductor tube is very lossy, the metallic tube has a much higher refractive index than the surrounding rock. This makes it possible to use the interface between the conductor and rock as a single conductor transmission line (SCTL) which is known to support slow surface waves in the axial direction, in such a way that axial currents along the metal tube propagate to the surface where they can be detected, as in Fig. 3.21.

The transmission of electromagnetic signals along the surface of a metallic conductor on a conductive rock can be obtained inductively by exciting the lower portion of the vertical conductor. Also the lower part of the electromagnetic spectrum should be considered to maintain a low attenuation.

The excitation of axial currents through the metal rod could be done by a coaxial solenoid fed with alternating current. However, in [25] is presented that this configuration would not excite axial currents of any substantial magnitude on the rode. Nevertheless, a more promising setup is achieved using a toroidal

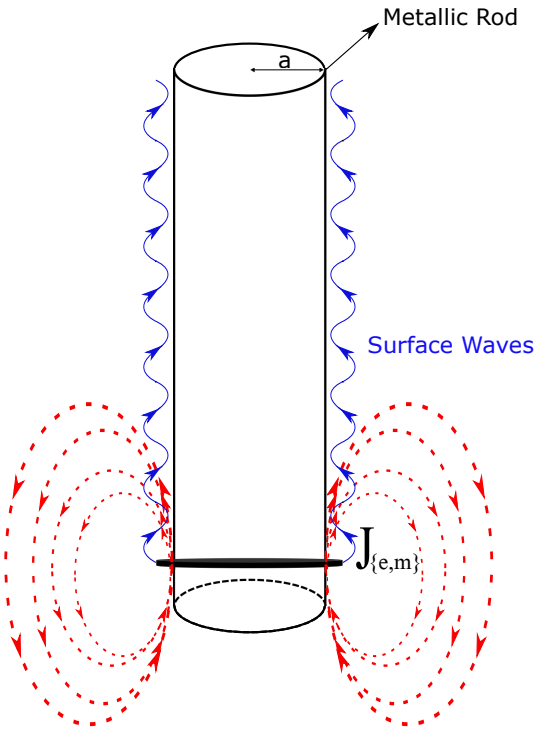

Figure 3.21: Current loop antenna radiating in the vicinity of an impenetrable cylinder.

coil coaxially with the rod. From an electromagnetic point of view, such a coil is equivalent to a magnetic current loop. Thus in this analysis, it will consider the propagation of surface waves through the metal rod excited by a loop sources, both magnetic and electric, in order to compare the results.

3.5.1 Surface Waves

Surface waves are electromagnetic waves that travel intimately tied to the surface of two different materials with a non-positive dielectric constant, like metals. Most of the energy of surface waves is confined to the close vicinity of the interface, which allow them to propagate in a direction parallel to the interface on either side of the interface, as is presented in Fig. 3.22.

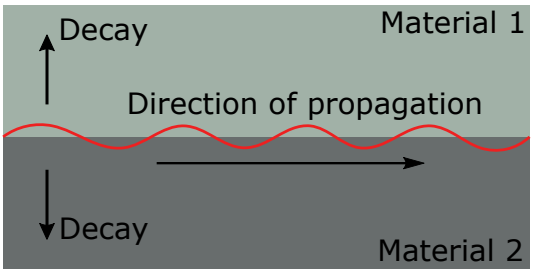

Figure 3.22: Surface wave at the interface of two different materials.

At radio frequencies, these waves can travel thousands of wavelengths and their associated fields are often best described as surface current. After certain distance away from the interface, these waves experiment an exponential decay, which is governed by the propagation function e^{ikz} along the axis of the structure [55, 56].

Surfaces waves come out in several situations involving antennas. When an antenna is located closed a metal surface, it will radiate waves into free space, but also generate currents that propagate along the surface.

The fact that these waves are confined to a very narrow region about the interface, makes them very sensitive to the immediate interfacial environment. Any alteration in the composition of the materials at both sides of the interface could improve, disturb, or even vanish, the surface wave. In that sense, by engineering the composition close the interface, a surface wave can be allowed to propagate longer distances. These engineer structures are known as artificial impedance surfaces. When the two media have permittivities with different values and the permeabilities are very similar, only TM surfaces waves can propagate significant distances, because TE field components vanish identically. By duality, when the permeabilities are different and the permittivities are similar, only TE surface waves will propagate [57].

3.5.2 Conductive Tube Modeling

In Fig. 3.21 is presented a current loop (either electric or magnetic) radiating in the presence of an circular metal rod of radius a, located in an unbounded medium. In most of the electromagnetic problems, the domain under consideration consists of several different media, where the electromagnetic field governing equations for each region are linked by boundary conditions that involve values on both sides of the interface. Thus, even if the main interested is focused only on one side, the problem must be solved simultaneously for all media.

However, under certain conditions, the number of regions involved in the solution procedure may be reduced. One example of this is the elimination of a body of infinite conductivity, Perfect Electrical Conductor (PEC), from the computational space, by enforcing the tangential electric field or normal magnetic flux to be equal to zero at the boundary [58]. The PEC condition is a simplified form of equation (3-41), where

$$\begin{aligned} \hat{n} \times \mathbf{E}\big|_{interface} &= \mathbf{0}, \quad \text{and} \\ \hat{n} \cdot \mathbf{B}\big|_{interface} &= 0. \end{aligned} \tag{3-106}$$

In practice, any real material has finite conductivity so that the PEC is merely a model of a good conductor in which the skin depth is assumed to be zero. The skin depth δ is defined as the distance the wave must travel in a lossy medium to reduce its value to e^{-1}, and is determined as in [49]

$$\delta = \sqrt{\frac{2}{\omega_{source}\sigma_c\mu_c}}, \quad \text{if} \quad \frac{\sigma_c}{\omega_{source}} \gg \epsilon_c. \tag{3-107}$$

Although the PEC condition is very attractive for implementation, its application in practical design is very limited because neglects the electromagnetic fields into the conductor.

To determine when the PEC approximation may be applied requires a comparison between the skin depth and the characteristic size t (generally the thickness) of the conductor. For practical purposes, the conductor thickness can be finite, and must be larger than a few skin depths. The minimum thickness required depends on the accuracy of the application. Some authors have taken this limit as $t > 6\delta$ [59]. For thickness values less than the minimum required for applying the PEC boundary condition, this approximation leads to errors proportional to δ/t.

Most of real line conductors have electric conductivity about 10^4 to 10^7 S/m and the relative permeability about 1. For a frequency range of 1 Hz to 1 MHz, the skin depth take the values in the range of: 1.6×10^{-4} m to 5 m. For conductor with thickness of typical printed circuit boards, these values of skin depth are not small, and the PEC condition may not be applied in these cases.

The thickness of typical oil well tubes, is about 2.5 cm, a value with the same order, or smaller, in comparison with the skin depth for certain frequencies. Under this terms, the PEC condition does not appear to be so accurate for this scenario. However, this is the simplest boundary condition, and will allow to obtain preliminary results of the wave behavior around the conductive tube. In a first analysis, the conducting tube will be treated as a PEC, and posteriorly more rigorous boundary conditions will be assessed.

The PEC boundary condition at ($\rho = a$), specifies that the tangential components of the electric field vanish at the conductor surface. Unlike the scenario without the conductive tube, now the origin of coordinates is no longer included in the problem domain, so the radial component of the electric field takes the form of (3-37), with B the radial coefficient that guarantee

the PEC boundary condition at the metallic surface. In Fig. 3.23 is shown a cross-sectional and a side view, respectively, of a metallic cylinder immersed in a lossy medium (soil/rock).

From (3-106), the axial and azimuthal components of the electric field must satisfy

$$\begin{aligned} E_z\Big|_{\rho=a} &= 0, \text{ and} \\ E_\phi\Big|_{\rho=a} &= 0. \end{aligned} \tag{3-108}$$

In cases of having a transmission antenna in the form of an electric current loop, the null condition of the axial component of the above equation is already satisfied from (3-97), in accordance with the TE^z solution obtained. In order to guarantee the vanishing of the azimuthal component of the electric field in the cylinder surface, the solution of (3-63) must be set to zero when $(\rho = a)$,

$$E_\phi\Big|_{\rho=a} = -\frac{\omega\mu_\rho\rho' I_e}{2}\int_0^\infty dk_\rho \frac{k}{k_z}\hat{F}_1(k_\rho a)\hat{F}_1(k_\rho\rho')e^{ik_z|z-z'|} = 0, \tag{3-109}$$

which is only satisfied provided that the term $\hat{F}_1(k_\rho a)$ vanish

$$\hat{F}_1(k_\rho a) = 0. \tag{3-110}$$

After substituting (3-37) into the above equation

$$J_1(k_\rho a) + BY_1(k_\rho a) = 0, \tag{3-111}$$

yields to

$$B = -\frac{J_1(k_\rho a)}{Y_1(k_\rho a)}. \tag{3-112}$$

According to the above equation, the radial function of the azimuthal component of the electric field when the antenna is an electric current loop

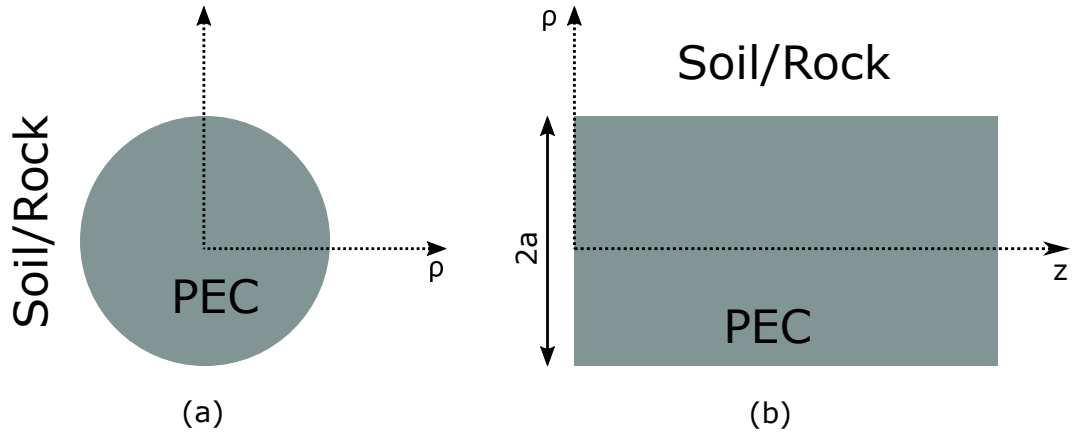

Figure 3.23: Geometry of the cylindrical conductor immersed in a lossy medium. (a) Cross-sectional view. (b) Side view. (Adapted from [52])

adopts the form of

$$\hat{F}_1(k_\rho a) = J_1(k_\rho \rho) - \frac{J_1(k_\rho a)}{Y_1(k_\rho a)} Y_1(k_\rho \rho). \tag{3-113}$$

In a similar manner, when it is considered the radiation of magnetic current loops, the null condition of the azimuthal component of the electric field in (3-108) is already satisfied in accordance with the solution obtained in (3-98). In order to force the vanishing of the axial component of the electric field, it can be used the E_z obtained in (3-98), and imposing that

$$E_z\Big|_{\rho=a} = -\frac{i\epsilon_\rho \rho' I_m}{2\epsilon_z} \int_0^\infty dk_\rho \, \frac{k_\rho^2}{k_z} \hat{F}_0(k_\rho a) \hat{F}_1(k_\rho \rho') e^{ik_z|z-z'|} = 0. \tag{3-114}$$

which is only satisfied if the term $\hat{F}_0(k_\rho a)$ vanish

$$\hat{F}_0(k_\rho a) = 0. \tag{3-115}$$

When substituting (3-37) into the above equation

$$J_0(k_\rho a) + BY_0(k_\rho a) = 0, \tag{3-116}$$

yields to

$$B = -\frac{J_0(k_\rho a)}{Y_0(k_\rho a)}. \tag{3-117}$$

Then, the radial function of the azimuthal component of the magnetic field of a TM^z wave can be expressed as

$$\hat{F}_1(k_\rho a) = J_1(k_\rho \rho) - \frac{J_0(k_\rho a)}{Y_0(k_\rho a)} Y_1(k_\rho \rho). \tag{3-118}$$

Therefore, a general solution for the radial function can be expressed as

$$\hat{F}_1(k_\rho a) = J_1(k_\rho \rho) - \frac{J_s(k_\rho a)}{Y_s(k_\rho a)} Y_1(k_\rho \rho). \tag{3-119}$$

where $s = \{1, 0\}$ for the TE^z and TM^z modes, respectively.

3.5.3 Numerical Implementation and Analysis

In this subsection, some numerical examples calculated using the theory described in Section 3.5 will be presented . In the scenario, the source is modeled as a 10-in-radius electric (magnetic) coil with a constant electric (magnetic) current of 1 A (1 V) placed surrounding a metal pipe with radio $a = 9$ [in]. The metal pipe is modeled as a PEC, without loss of generality. It will be considered isotropic and biaxial anisotropic media, with a magnetic or electric current loop only as excitation source.

3.5.3.1 Homogeneous Isotropic Formation

First, consider the lossy isotropic medium described by its electrical conductivity with value 0.5 S/m. Initially, the operation frequency for this example is 200 kHz in order to compare the results obtained previously. As in the previous example, the relative dielectric and magnetic constants are unity, as in the previous section. The results are compared with the ones obtained with COMSOL. This numerical modeling tools will also help to visualize the field distributions.

In Fig. 3.24, Fig. 3.25 and Fig. 3.26, are presented the amplitude, phase and attenuation, respectively, of the azimuthal component of the electric (magnetic) field E_ϕ (magnetic H_ϕ). The bigger concentration of samples near the origin in the COMSOL solution is due to the selected grid, which aims to a better analysis of the field near the source position. It can be observed how both solutions converge to the same results with a very small difference.

In Table 3.3 the computational costs for COMSOL and the employed solution are compared. It can be appreciated that the implemented solution

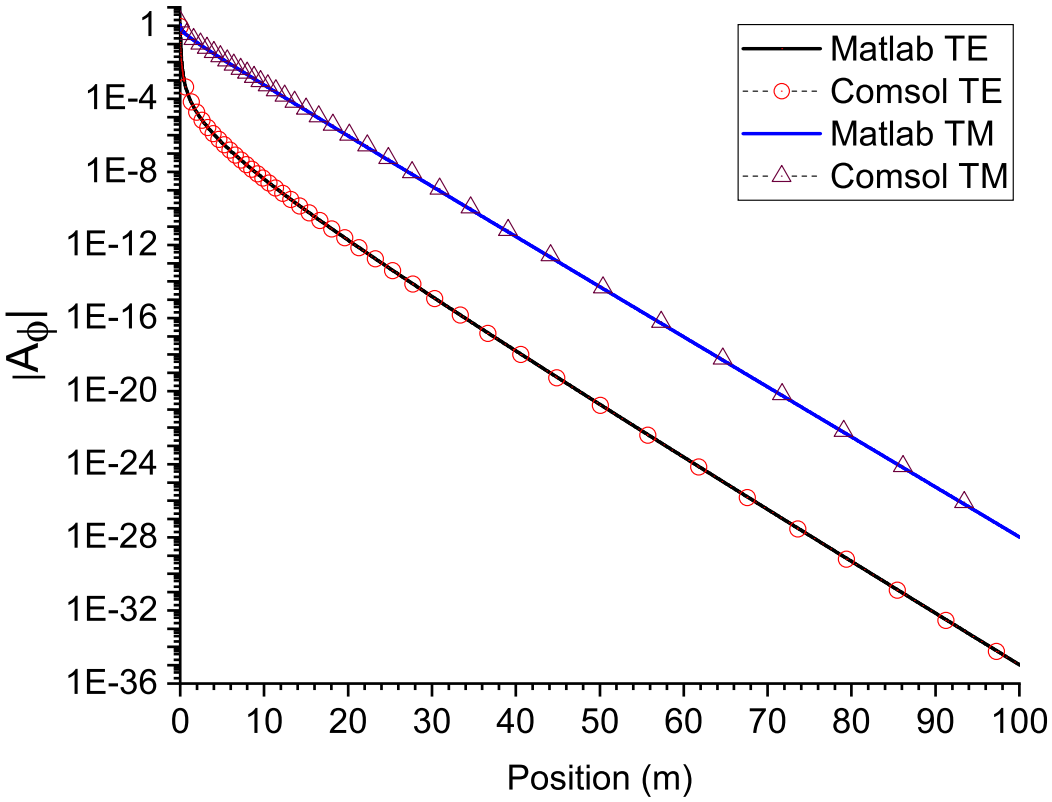

Figure 3.24: Absolute values of the azimuthal components of the electric (magnetic) field E_ϕ (H_ϕ) in an isotropic formation with an embedded cylinder (200 kHz).

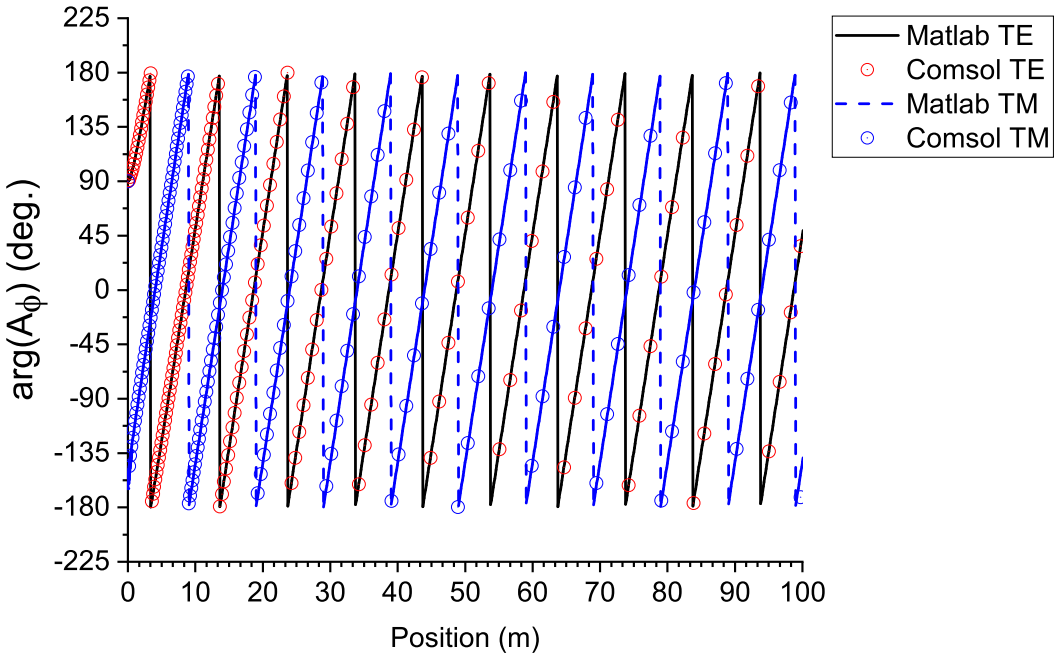

Figure 3.25: Phase values of the azimuthal components of the electric (magnetic) field E_ϕ (H_ϕ) in an isotropic formation with an embedded cylinder (200 kHz).

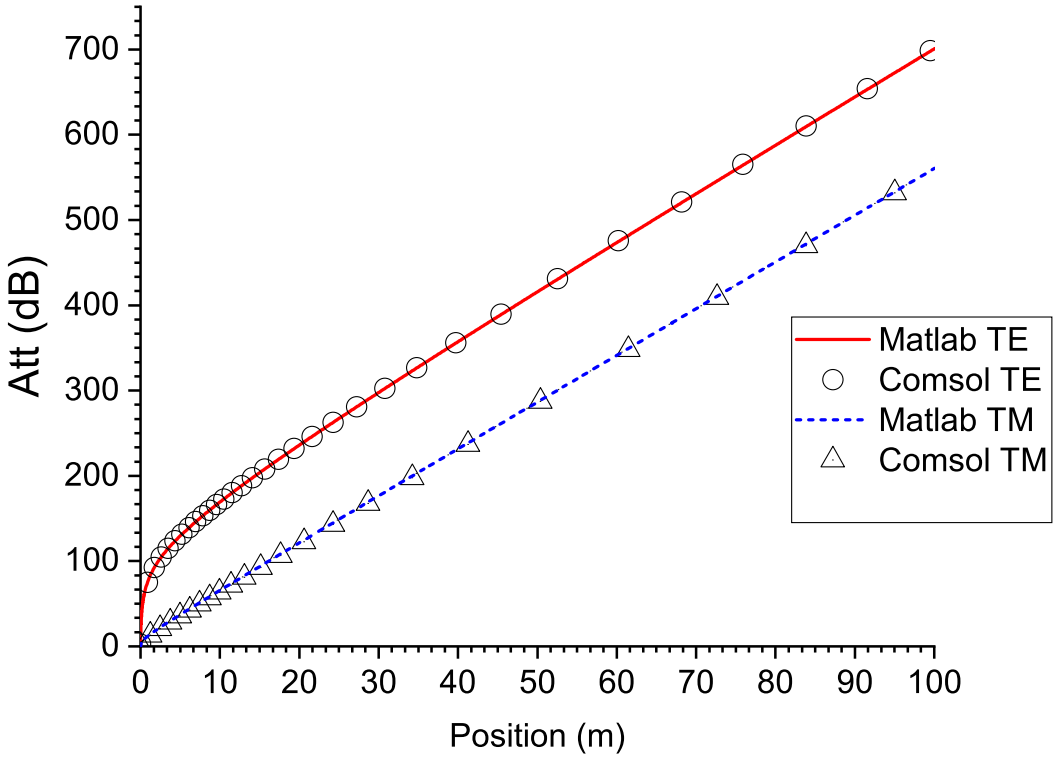

Figure 3.26: Attenuation experimented by the azimuthal components of the electric (magnetic) field E_ϕ (H_ϕ) in an isotropic formation with an embedded cylinder (200 kHz).

	Implemented Solution	COMSOL
RAM memory	15.78 MB	52.83 GB
CPU time	23.42 s	116.3 s

Table 3.3: Computational costs of modeling a homogeneous isotropic formation surrounding a cylindrical metallic rod.

is more computationally efficient than the obtained with COMSOL, and the results from the two solutions are almost the same.

In Fig. 3.27 is presented a comparison between these results with the obtained in the previous section. It can be noticed that the attenuation for the TM^z reduces drastically due the presence of the metallic cylinder, while for the TE^z mode it increases slightly. If the operation frequency is reduced to 1 kHz, also the attenuation is reduced considerably, as in Fig. 3.28. The TM^z mode still experiments less attenuation than the TE^z mode when the cylinder is presented.

The presence of the cylinder makes the attenuation of the TM^z mode have a linear behavior, while the TE^z mode has a logarithmic behavior near the source, and far away from it behaves as linear. In the radial direction, the waves also attenuates considerably, as is shown in Fig. 3.29. As in the previous scenarios, the TM^z mode exhibits better propagation characteristics than the TE^z.

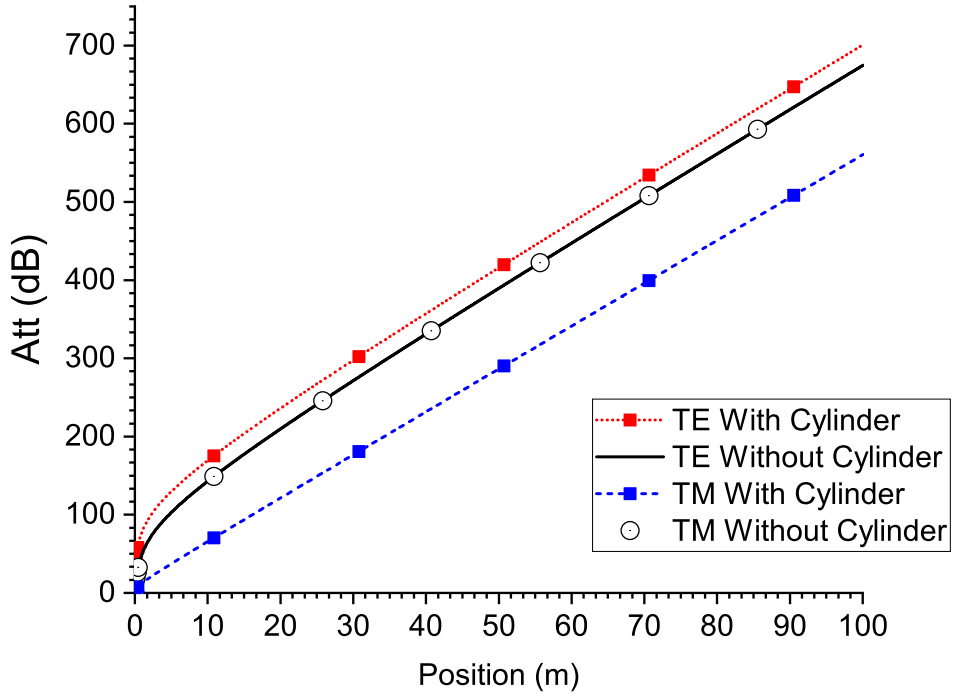

Figure 3.27: Comparison of the attenuation experimented by the azimuthal components of the electric (magnetic) field E_ϕ (H_ϕ) in an isotropic formation with and without the embedded cylinder (200 kHz).

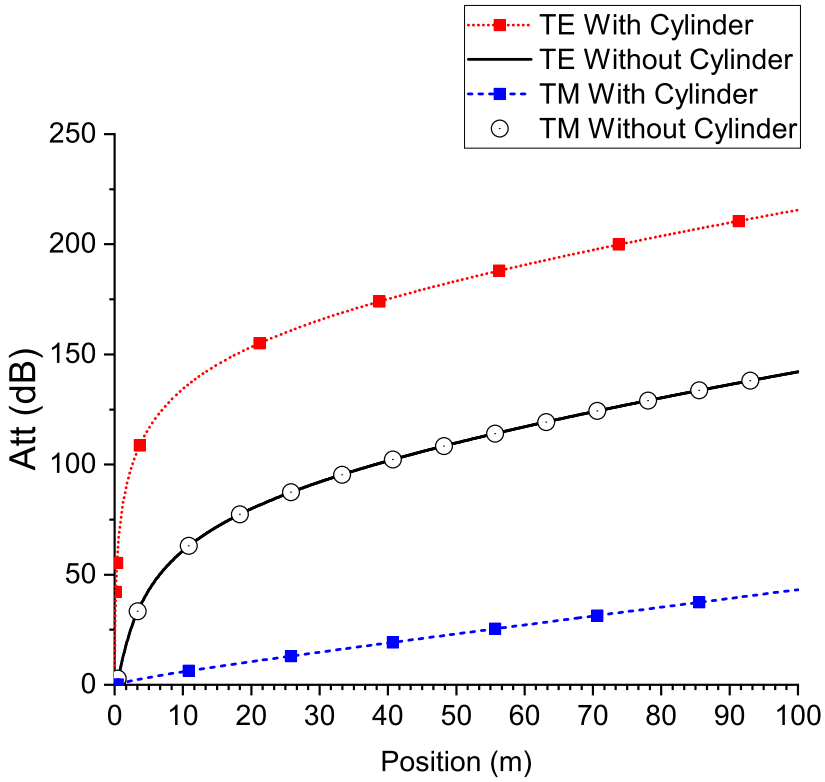

Figure 3.28: Comparison of the attenuation experimented by the azimuthal components of the electric (magnetic) field E_ϕ (H_ϕ) in an isotropic formation with and without the embedded cylinder (1 kHz).

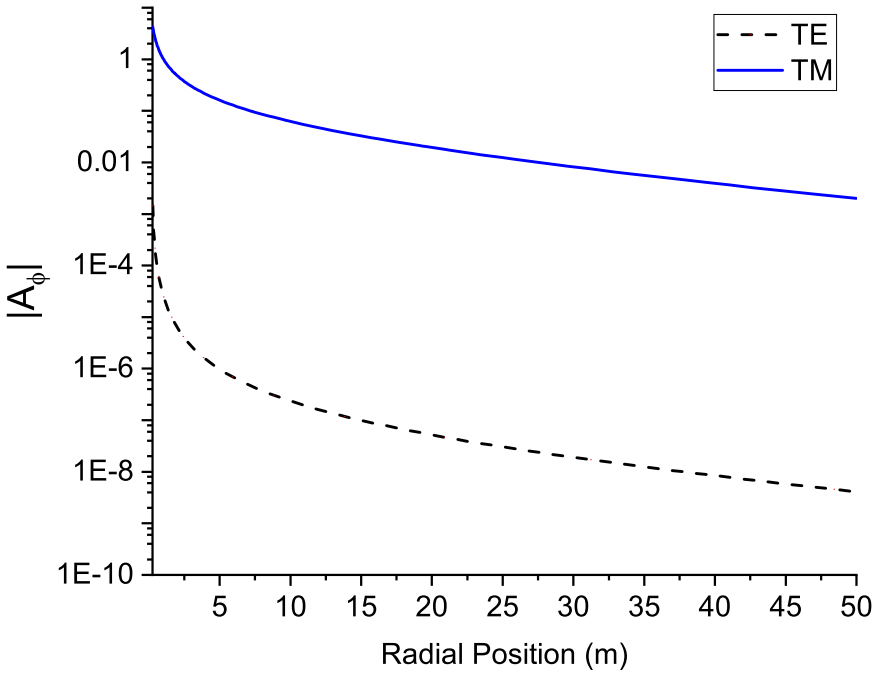

Figure 3.29: Absolute values of the azimuthal components of the electric (magnetic) field E_ϕ (H_ϕ) in an isotropic formation with an embedded cylinder, as a function of the radial position (1 kHz).

In order to visualize the propagation behavior of the electromagnetic field around the cylindrical metallic tube (which is located at the origin of coordinates with an extension of 150 m in the vertical direction and 10 [in] of radio), Fig. 3.30 shows the magnitude of the magnetic field component H_ϕ computed with COMSOL at 1 kHz as a function of the radial and the vertical distance from the source (placed at $z = 0$). It can be observed that the fields are radially concentrated around the metallic cylinder as a consequence of the high conductivity of the surrounding medium.

3.5.3.2 Homogeneous Biaxial Anisotropic Formation

Employing the same procedure that in Section 3.4.5.2, three cases were analyzed by a permutation of the values in the conductivity tensor.

$$\bar{\bar{\sigma}}_1 = \begin{bmatrix} 0.5 & 0 & 0 \\ 0 & 0.3 & 0 \\ 0 & 0 & 0.1 \end{bmatrix}, \quad \bar{\bar{\sigma}}_2 = \begin{bmatrix} 0.1 & 0 & 0 \\ 0 & 0.5 & 0 \\ 0 & 0 & 0.3 \end{bmatrix}, \quad \bar{\bar{\sigma}}_3 = \begin{bmatrix} 0.3 & 0 & 0 \\ 0 & 0.1 & 0 \\ 0 & 0 & 0.5 \end{bmatrix}. \quad \text{(3-120)}$$

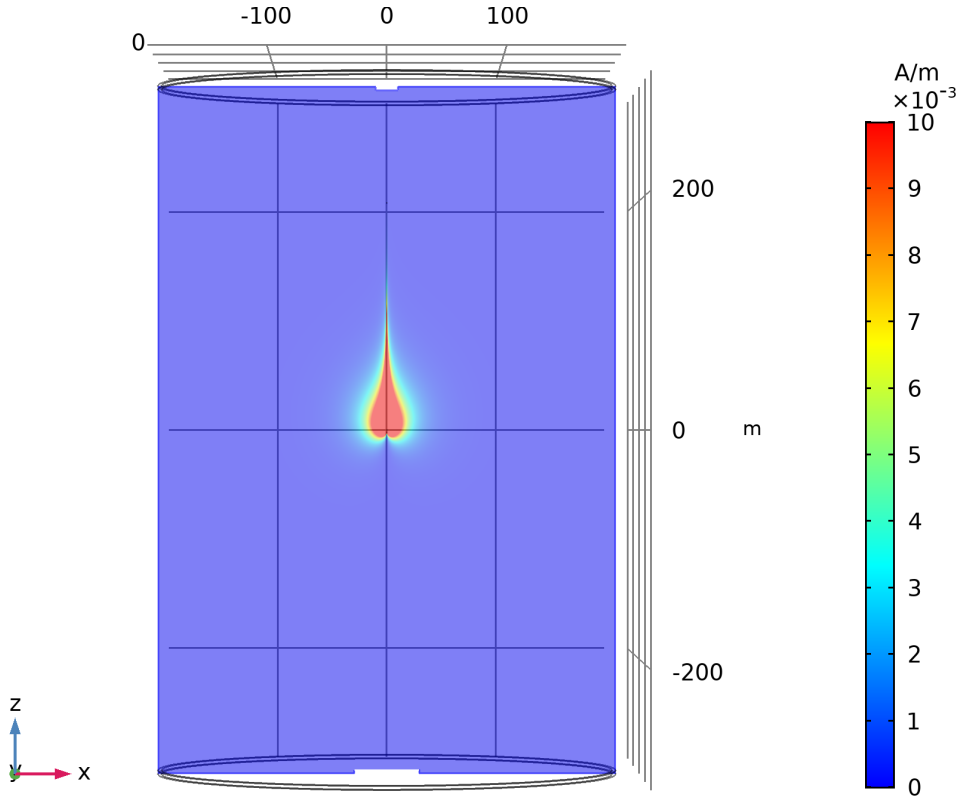

Figure 3.30: Azimuthal components of the magnetic field H_ϕ in an isotropic formation with an embedded cylinder (1 kHz) (simulated with COMSOL).

The operation frequency for this example is 1 kHz. The obtained results for the attenuation are shown in Fig. 3.31. Also, for comparison, the attenuation curves for the isotropic medium characterized by a conductivity of 0.5 S/m are included.

There are several differences between the above figure and the scenario without the metallic cylinder, as in Fig. 3.20. When the metallic cylinder is presented, the attenuation experimented by the TE^z, regardless of the ordering of the values in the conductivity tensor, is always higher than the attenuation suffered by the TM^z wave. For the TM^z mode, the isotropic case has the higher attenuation, which value is a slightly superior than the one with the same conductivity value in the radial component of the conductivity tensor. Without the cylinder, the isotropic medium was not the most attenuator case for the TM^z mode. However, for the TE^z mode, the isotropic configuration lead to the more attenuated scenario, as in the case without the cylinder. It can be noticed that the difference in the attenuation values for both modes is considerable (about 175 dB).

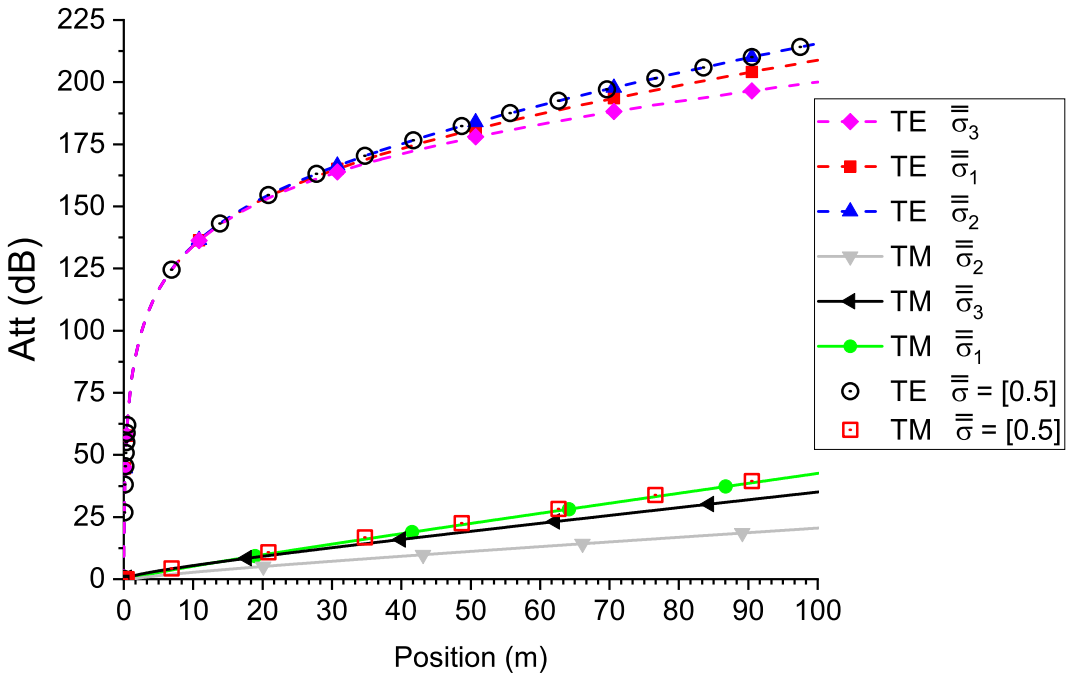

Figure 3.31: Attenuation experimented by the azimuthal component of the electric (magnetic) field E_ϕ (H_ϕ) for different configuration of the anisotropy (1 kHz). Comparison with the isotropic case for $\bar{\bar{\sigma}} = [0.5]$.

3.6 Conclusions

A numerically stable method for solving Maxwell's equations in a biaxially anisotropic media was introduced in this chapter. To reduce the complexity, the initial 3D problem was simplified to a equivalent 2D one by assuming that the media and the sources are azimuthally symmetric.

A novel spectral domain approach based on the Hankel transform was introduced and a series of validation results against brute-force finite-element solvers were presented that demonstrate the ability of the technique for analyzing surface wave propagation in complex media via a numerically stable and robust semi-analytic algorithm. It was also analyzed the effect of the anisotropy in the wave propagation.

In addition, it was shown that the presence of a metallic tube severely impacts the attenuation of electromagnetic fields. In such scenario, antennas based on magnetic field excite fields with lower attenuation than those created by electric one in conductive media at low frequency. This makes the use of TM^z fields antennas more suitable for wireless telemetry in deep oil wells.

4
Horizontal Stratified Media

4.1
Introduction

The scattering of electromagnetic waves is an important problem in borehole geophysics probing. Horizontal bed boundaries change the response of tools, making the interpretation of logs very difficult [32]. A good understanding of the diffraction of waves by bed boundary is necessary to predict the characteristics of the electromagnetic telemetry systems for oil well.

The electromagnetic properties of the Earth's crust generally do not vary significantly in the horizontal direction. However, there is a tendency to vary in the transversal direction in the form of abrupt or continuous changes [24]. Therefore, an idealization to analyze the propagation of electromagnetic waves can be done by supposing the medium horizontally stratified, and effectively treat it by the sub-division into a number of parallel homogeneous layers.

In Fig. 4.1 it is presented an approximately planar layered medium. Each layer is characterized by its own electromagnetic properties. Without loss of generality, it will be assumed that the region m is bellow region n. This is done in order to facilitate the mathematical modeling presented herein.

The media is characterized by the complex magnetic permeability and electric permittivity tensors

$$\begin{bmatrix} \mu_\rho(z) & 0 & 0 \\ 0 & \mu_\phi(z) & 0 \\ 0 & 0 & \mu_z(z) \end{bmatrix} \quad \text{and} \quad \begin{bmatrix} \epsilon_\rho(z) & 0 & 0 \\ 0 & \epsilon_\phi(z) & 0 \\ 0 & 0 & \epsilon_z(z) \end{bmatrix}, \tag{4-1}$$

respectively, with

$$\begin{aligned} \mu_{\{\rho,\phi,z\}}(z) &= \mu_0 \mu_{r\{\rho,\phi,z\}}(z) \ , \ \text{and} \\ \epsilon_{\{\rho,\phi,z\}}(z) &= \epsilon_0 \epsilon_{r\{\rho,\phi,z\}}(z) + \frac{i}{\omega}\sigma_{\{\rho,\phi,z\}}(z). \end{aligned} \tag{4-2}$$

The effective magnetic and dielectric constants, and effective conductivity of the media in the α-direction, are function of the axial position. When considering the case in which the permeability and permittivity tensors are piecewise constant functions of z, the equation (3-30) can be solved first in

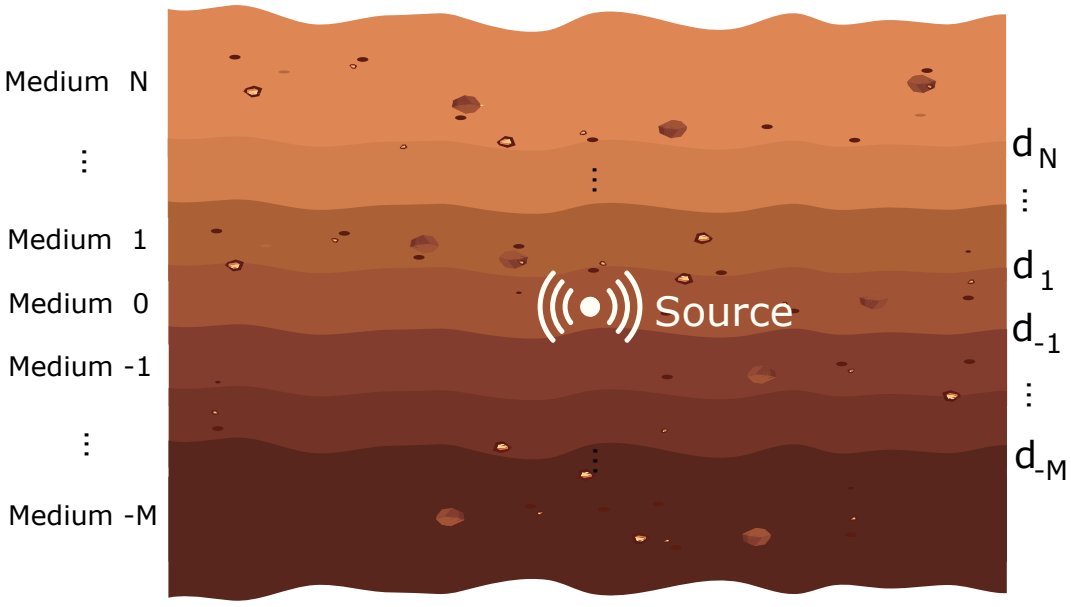

Figure 4.1: Horizontally stratified N-layer media.

each region, and a unique solution can be found later by matching boundary conditions across the discontinuities at the interfaces d_j $(j = \pm 1, \pm 2, ...)$.

This chapter will discuss the electromagnetic field solutions in a biaxially anisotropic N-layer media whose interfaces are delimited by planar boundary of infinite extent in the radial direction. Reflection and transmission coefficients will be derived to account for the reflection and transmission of the fields by the several boundaries. These coefficients will be functions of the constitutive parameters of the media and the operation frequency. Some numerical results are presented for validation of the solution. Also, some cases are considered to analyze the propagation effects at high contrast interfaces.

4.2 Reflection and Transmission in Multiple Interfaces

In addition to the propagation attenuation of electromagnetic waves in lossy-media, when a propagating wave (incident wave) encounters an interface that separates two media characterized by the constitutive parameters ϵ and μ, part of the wave intensity will be reflected back into the incidence medium, and another part will be transmitted into the medium delimited by the other side of the interface. Furthermore, a wave that crosses an interface may reflect multiple times on the walls delimiting the layer until it is transmitted to the next layer. As a consequence, the wave will be interfered with multipath signals due to the multiple reflection and refraction through the geological formation. This phenomenon can be visualized in the geometrical optics, multiple reflection

and transmission scenario depicted in Fig. 4.2.

A simplified approach of the above figure may be achieved if it is defined a generalized reflection and transmission coefficient, which are result of the contribution of the multiple reflected waves inside a layer and the transmitted waves of the layers outside. This strategy is described in [34], and presented in the Fig. 4.3, where $\tilde{R}_{nm}$ and $\tilde{T}_{nm}$ denote the generalized reflection and transmission coefficients at the interface between the media n and m. These coefficients can be determined using the geometrical optic model, by mean of a combination of the reflected and transmitted wave described below

$$\begin{aligned}
\tilde{R}_{0,1} &= R_1^0 + T_1^0 + T_2^0 + T_3^0 + .., \\
\tilde{R}_{1,2} &= R_1^1 + R_3^1 + RT_1^1 + RT_2^1 + ..., \\
\tilde{T}_{0,1} &= T_1^1 + R_2^1 + R_4^1 + R_5^1 + ..., \\
\tilde{R}_{2,3} &= R_1^2 + R_2^2 + ..., \\
\tilde{T}_{1,2} &= T_1^2 + T_2^2 + RT_1^2 + RT_2^2 + ...,
\end{aligned} \tag{4-3}$$

It is important to note that the solution for the z-component of the electromagnetic fields of equation (3-40) can be treated as locally plane waves for a given radial position. Since the reflecting surface considered are planar, the solution for the z-component for the reflected or transmitted waves can be also considered locally plane waves. This allows to express the reflected and transmitted waves as exponential functions weighted by the reflection

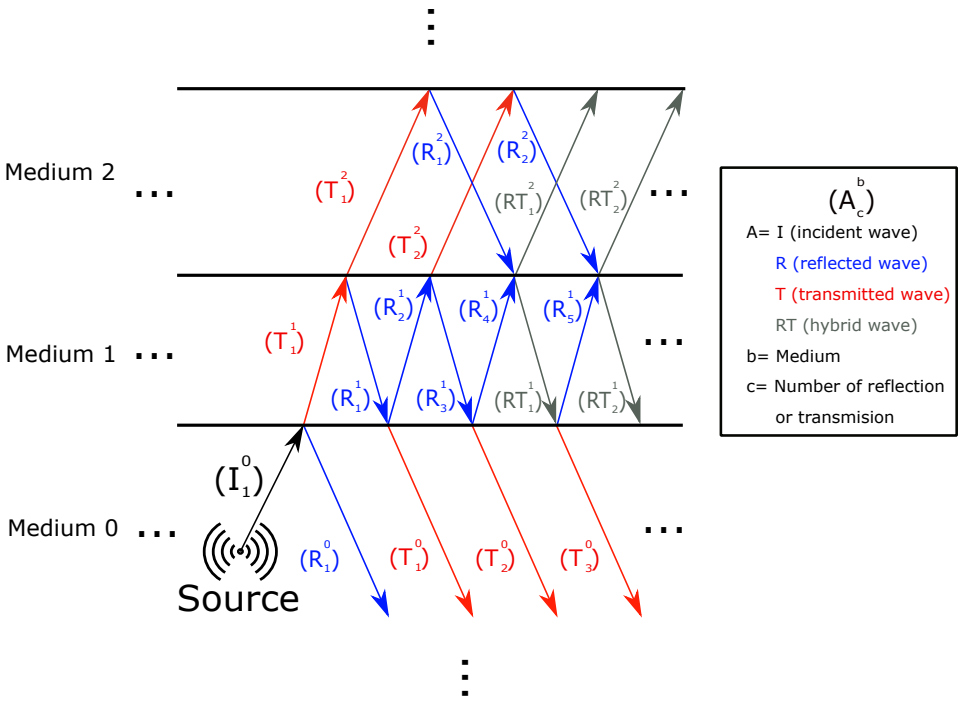

Figure 4.2: Reflection and transmission at interfaces.

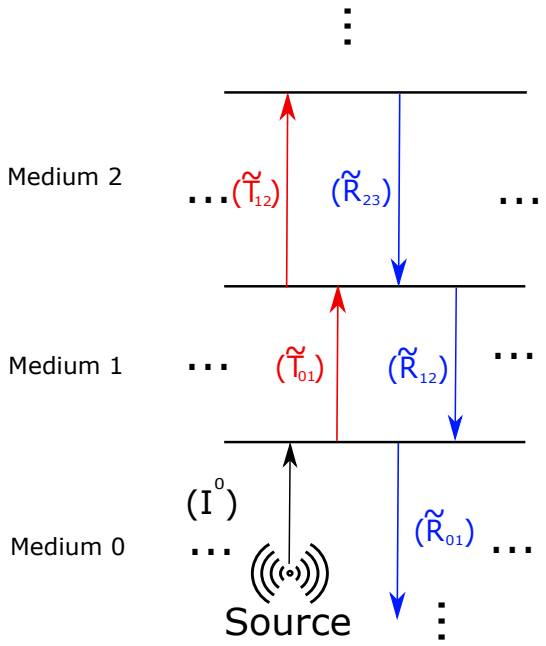

Figure 4.3: Generalized reflection and transmission at interfaces.

and transmission coefficient of the media surrounding the interface. For the region n, where $n > 0$, the generalized reflection coefficient takes the form of

$$\begin{aligned}\tilde{R}_{n,n+1} = R_{n,n+1} + T_{n,n+1}\tilde{R}_{n+1,n+2}\ e^{2ik_{n+1,z}(d_{n+2}-d_{n+1})}T_{n+1,n} + \\ T_{n,n+1}\left[\tilde{R}_{n+1,n+2}\ e^{2ik_{n+1,z}(d_{n+2}-d_{n+1})}\right]^2 R_{n+1,n}T_{n+1,n} + \\ T_{n,n+1}\left[\tilde{R}_{n+1,n+2}\ e^{2ik_{n+1,z}(d_{n+2}-d_{n+1})}\right]^3 R^2_{n+1,n}T_{n+1,n}\cdots,\end{aligned} \tag{4-4}$$

where the first term is the result of a single reflection at the interface, and the following terms are the result of multiple reflections of waves that kept trap in the considered layer. The above definition of the generalized reflection coefficient can be used to define the generalized transmission coefficient, which can be expressed as

$$\begin{aligned}\tilde{T}_{n,n+1} = T_{n,n+1} + R_{n,n+1}\tilde{R}_{n,n-1}\ e^{2ik_{n,z}(d_{n+1}-d_n)}T_{n,n+1} + \\ \left[R_{n,n+1}\tilde{R}_{n,n-1}\ e^{2ik_{n,z}(d_{n+1}-d_n)}\right]^2 T_{n,n+1} + \\ \left[R_{n,n+1}\tilde{R}_{n,n-1}\ e^{2ik_{n,z}(d_{n+1}-d_n)}\right]^3 T_{n,n+1}\cdots,\end{aligned} \tag{4-5}$$

where the exponential term

$$e^{2ik_{n+1,z}(d_{n+2}-d_{n+1})} \tag{4-6}$$

corresponds to the phase gained by the wave in its round trip in a slab of thickness $(d_{n+2} - d_{n+1})$.

It is important to note that $R_{n,n+1}$ and $T_{n,n+1}$ are the intrinsic local

reflection and transmission coefficients, respectively. They represent the ratio of the amplitude of the reflected and transmitted wave to the amplitude of the incident wave, respectively, that would exist at each interface if two semi-infinite media form each of the boundaries [49]. The reflection and transmission coefficients are unknown variables that will be determined by applying boundary conditions on the field along the interfaces, by enforcing continuity of the tangential components of the electric and magnetic fields.

4.2.1 Local Reflection and Transmission Coefficients

The local reflection and transmission coefficients at the interface between two media can be determined by neglecting the presence of other boundaries, assuming that the media at both sides of the interface have semi-infinite extension. This can be approximated as a half-space media with two piecewise constant regions, which is the simplest example of a planar, one-dimensional inhomogeneity [34].

In Fig. 4.4 it is presented a two-layers medium with different electromagnetic characteristics on each other. For simplicity, the source is placed in the lower layer, but it could perfectly allocated in the upper one. It can be noticed that the media only vary in the z-direction, and remain translationally invariant in the ρ-direction. As a result, the ρ-component must be equal at both sides of the interface in order to satisfy the matching condition.

However, the electromagnetic characteristics of the media change in the z-direction, and as a consequence, part of the energy of the incident wave in the lower layer will experiment a reflection, making that in the lower half-space, both incident and reflected waves are present. Thus, the general expression for the z-component in the lower half-space can be expressed as

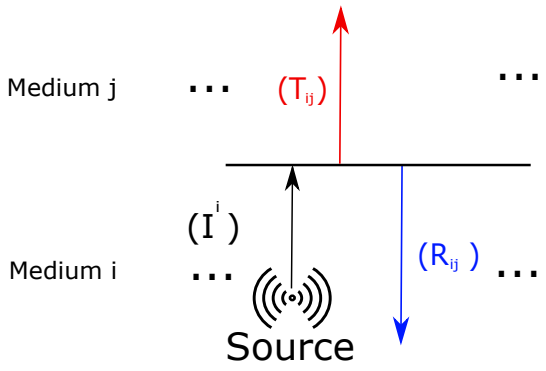

Figure 4.4: Reflection and transmission of a plane wave at an interface.

$$Z_1^+(z) = A_1^+ e^{ik_{1z}(z-z')} \left[1 + R_{12} e^{-2ik_{1z}(z-d_1)}\right], \tag{4-7}$$

$$Z_1^-(z) = A_1^- e^{-ik_{1z}(z-z')} \left[1 + R_{12} e^{-2ik_{1z}(z'-d_1)}\right], \tag{4-8}$$

where R_{12} represents the intrinsic local reflection coefficient at the interface delimited by the media 1 and 2.

Meanwhile, in the upper half-space only a transmitted wave is present, which general expression may be defined as

$$Z_2(z) = A_1^+ T_{12} e^{ik_{2z}(z-d_1)} e^{ik_{1z}(d_1-z')}, \tag{4-9}$$

where T_{12} represents the intrinsic local transmission coefficient at the same interface.

It is important to have in mind that the axial propagation constant from (3-66) is no longer the same throughout the structure as a consequence of the different electromagnetic properties of each layer. Therefore, k_z for the n-layer it can be define as

$$k_{nz} = \pm\sqrt{k_n^2 - \left(\frac{p_{n\rho}}{p_{nz}}\right) k_\rho^2}. \tag{4-10}$$

where $p = \mu$, $k_n^2 = \omega^2 \epsilon_{n\phi} \mu_{n\rho}$, for TE^z mode, and $p = \epsilon$, $k_n^2 = \omega^2 \epsilon_{n\rho} \mu_{n\phi}$, for TM^z mode.

The constants A_1^+ and A_1^- can be determined the boundary conditions at the source position. However, in order to determine R_{12} and T_{12}, it just need to be applied the boundary conditions at the interface.

For the TE^z wave, when applying the boundary condition (3-43) at the interface, the azimuthal component of the electric field of both layers must be continuous, because there are no sources in that region. However, due the translational invariance of the medium in the ρ-direction, the condition (3-43) can be satisfied if the z-component of the azimuthal electric field of both layers are continuous at the interface. Then,

$$A_1^+ T_{12}^{TE} e^{ik_{2z}(z-d_1)} e^{ik_{1z}(d_1-z')}\Big|_{z=d_1} = A_1^+ e^{ik_{1z}(z-z')} \left[1 + R_{12}^{TE} e^{-2ik_{1z}(z-d_1)}\right]\Big|_{z=d_1}, \tag{4-11}$$

which conducts to

$$A_1^+ T_{12}^{TE} e^{ik_{2z}(d_1-d_1)} e^{ik_{1z}(d_1-z')} = A_1^+ e^{ik_{1z}(d_1-z')} \left[1 + R_{12}^{TE} e^{-2ik_{1z}(d_1-d_1)}\right]. \tag{4-12}$$

After some manipulation in the above equation, it can be obtained

$$T_{12}^{TE} = 1 + R_{12}^{TE} \tag{4-13}$$

The application of the boundary condition (3-46) at the interface between the media conducts to

$$-(i\omega\mu_{2\rho})^{-1}\frac{\partial E_\phi^2}{\partial z}\Big|_{z=d_1}+(i\omega\mu_{1\rho})^{-1}\frac{\partial E_\phi^1}{\partial z}\Big|_{z=d_1}=0. \tag{4-14}$$

A similar analysis of the translational invariance in the ρ-direction can be done for the above equation, which allows to reduce the above equation to

$$\begin{aligned}&(i\omega\mu_{2\rho})^{-1}\frac{\partial}{\partial z}\left\{A_1^+T_{12}^{TE}e^{ik_{2z}(z-d_1)}e^{ik_{1z}(d_1-z')}\right\}\Big|_{z=d_1}\\ =&(i\omega\mu_{1\rho})^{-1}\frac{\partial}{\partial z}\left\{A_1^+e^{ik_{1z}(z-z')}\left[1+R_{12}^{TE}e^{-2ik_{1z}(z-d_1)}\right]\right\}\Big|_{z=d_1}.\end{aligned} \tag{4-15}$$

After the application of the z-derivative and evaluating at $z=d_1$ in last equation, it is obtained

$$(i\omega\mu_{2\rho})^{-1}\left\{ik_{2z}A_1^+T_{12}^{TE}e^{ik_{1z}(d_1-z')}\right\}=(i\omega\mu_{1\rho})^{-1}\left\{ik_{1z}A_1^+e^{ik_{1z}(d_1-z')}\left[1-R_{12}^{TE}\right]\right\}. \tag{4-16}$$

Last equation can be reduced to

$${\mu_{2\rho}}^{-1}(k_{2z})T_{12}={\mu_{1\rho}}^{-1}(k_{1z})\left(1-R_{12}^{TE}\right). \tag{4-17}$$

The substitution of (4-13) into the above allows to determine the local reflection coefficient for the transversal electric mode. As a result

$$R_{12}^{TE}=\frac{k_{1z}\mu_{2\rho}-k_{2z}\mu_{1\rho}}{k_{1z}\mu_{2\rho}+k_{2z}\mu_{1\rho}}. \tag{4-18}$$

Consequently, the transmission coefficient takes the form of

$$T_{12}^{TE}=\frac{2k_{1z}\mu_{2\rho}}{k_{1z}\mu_{2\rho}+k_{2z}\mu_{1\rho}}. \tag{4-19}$$

For the TM^z fields, a similar procedure can be applied, and the local reflection and transmission coefficients results in

$$R_{12}^{TM}=\frac{k_{1z}\epsilon_{2\rho}-k_{2z}\epsilon_{1\rho}}{k_{1z}\epsilon_{2\rho}+k_{2z}\epsilon_{1\rho}}, \tag{4-20}$$

$$T_{12}^{TM}=\frac{2k_{1z}\epsilon_{2\rho}}{k_{1z}\epsilon_{2\rho}+k_{2z}\epsilon_{1\rho}}. \tag{4-21}$$

4.3 Construction of the Complete Solution

Once the intrinsic local reflection and transmission coefficients are determined, the generalized coefficients can be calculated using (4-4). This equation can be manipulated to obtain a more simplified approach,

$$\tilde{R}^s_{n,n+1} = R^s_{n,n+1} + T^s_{n,n+1}T^s_{n+1,n}\tilde{R}^s_{n+1,n+2}\ e^{2ik_{n+1,z}(d_{n+2}-d_{n+1})} \cdot \sum_{p=1}^{\infty}\left[R^s_{n+1,n}\tilde{R}^s_{n+1,n+2}\ e^{2ik_{n+1,z}(d_{n+2}-d_{n+1})}\right]^{p-1}, \tag{4-22}$$

where $s = \{\text{TE, TM}\}$.

In the above equation, the summation represents a geometric series because the ratio of each two consecutive terms is a constant function of the summation index p. This series converge if the absolute value of the ratio is less than unity. In order to guarantee this, it must been analyzed the terms into square brackets.

The k_z functions of (3-66) were chosen with the imaginary part bigger than zero in order to satisfy the radiation condition. Therefore, the absolute value of the exponential function in the term between square brackets in (4-22) will conduct to a fraction of unity. Also, when a wave impacts a passive interface, and part of its energy is transfered across the interface, the reflected wave must be weaker than the incident one, and as a consequence, the reflection coefficient must be less than unity.

These characteristics make the ratio of the summation series be less than unity, and therefore, the series converge. According to this, equation (4-22) can be reduced to

$$\tilde{R}^s_{n,n+1} = R^s_{n,n+1} + \frac{T^s_{n,n+1}T^s_{n+1,n}\tilde{R}^s_{n+1,n+2}\ e^{2ik_{n+1,z}(d_{n+2}-d_{n+1})}}{1 - R^s_{n+1,n}\tilde{R}^s_{n+1,n+2}\ e^{2ik_{n+1,z}(d_{n+2}-d_{n+1})}}. \tag{4-23}$$

Consequently, for the region m, where $m < 0$, the generalized reflection coefficient takes the form of:

$$\tilde{R}^s_{m,m-1} = R^s_{m,m-1} + \frac{T^s_{m,m-1}T^s_{m-1,m}\tilde{R}^s_{m-1,m-2}\ e^{2ik_{m-1,z}(d_{m-2}-d_{m-1})}}{1 - R^s_{m-1,m}\tilde{R}^s_{m-1,m-2}\ e^{-2ik_{m-1,z}(d_{m-2}-d_{m-1})}}. \tag{4-24}$$

For the layers $n = N$ and $m = -M$, it is established the condition that only outgoing waves are permissible. They are considered semi-infinite layers which produce no reflected waves, and as a consequence, $\tilde{R}^s_{N,N+1} = \tilde{R}^s_{M,M-1} = 0$. It can be appreciated that the generalized reflection coefficient can be calculated recursively, starting with the outermost layers to the source.

In a similar way, the generalized transmission coefficient described in (4-5) can be reduced to a more compact form

$$\tilde{T}^s_{n,n+1} = \frac{T^s_{n,n+1}}{1 - R^s_{n,n+1}\tilde{R}^s_{n,n-1}\ e^{2ik_{n,z}(d_{n+1}-d_n)}}, \text{and} \tag{4-25}$$

$$\tilde{T}^s_{m,m-1} = \frac{T^s_{m,m-1}}{1 - R^s_{m,m-1}\tilde{R}^s_{m,m+1}\ e^{2ik_{m,z}(d_{m-1}-d_m)}}. \tag{4-26}$$

In [33], the authors proposed the solution to the wave equation (3-29) for an isotropic multilayered medium using the separation of variable method, which solutions for the z-component have the form of

$$h^s_n(k_{n,z}z) = C^s_n e^{ik_{n,z}(z)}\left[1 + \tilde{R}^s_{n,n+1}e^{-ik_{n,z}(z-2d_{n+1})}\right], \tag{4-27}$$

for $n > 0$, and

$$h^s_m(k_{m,z}z) = C^s_m e^{-ik_{mz}(z)}\left[1 + \tilde{R}^s_{m,m-1}e^{ik_{mz}(z-2d_{m-1})}\right], \tag{4-28}$$

for $m < 0$.

This solution can be adapted to include the anisotropic characteristics of the media. However, its numerical implementation leaded to an overburden in the integration for the solution of (3-40). In order to provide an stable form with no overburden problems, the previous equations were rearranged, and the proposed solutions for the z-component were defined as

$$h^s_n(k_{n,z}z) = C^s_n e^{ik_{n,z}(z-z')}\left[1 + \tilde{R}^s_{n,n+1}e^{-2ik_{n,z}(z-d_{n+1})}\right], \tag{4-29}$$

for $n > 0$, and

$$h^s_m(k_{m,z}z) = C^s_m e^{-ik_{mz}(z-z')}\left[1 + \tilde{R}^s_{m,m-1}e^{2ik_{mz}(z-d_{m-1})}\right], \tag{4-30}$$

for $m < 0$.

Therefore, the solution for the Helmholtz equation at each layer for the azimuthal component of the electric or magnetic field according to (3-29) can be expressed as:

$$A^s_{n\phi} = \int_{k_\rho} dk_\rho\ g(k_\rho)\left[\frac{J_1(k_\rho\rho) + BY_1(k_\rho\rho)}{\sqrt{1+B^2}}\right]\left\{C^s_n e^{ik_{n,z}(z-z')} \times \left[1 + \tilde{R}^s_{n,n+1}e^{-2ik_{n,z}(z-d_{n+1})}\right]\right\}, \tag{4-31}$$

for $n > 0$, and

$$A^s_{m\phi} = \int_{k_\rho} dk_\rho\ g(k_\rho)\left[\frac{J_1(k_\rho\rho) + BY_1(k_\rho\rho)}{\sqrt{1+B^2}}\right]\left\{C^s_m e^{-ik_{mz}(z-z')} \times \left[1 + \tilde{R}^s_{m,m-1}e^{2ik_{mz}(z-d_{m-1})}\right]\right\}, \tag{4-32}$$

for $m < 0$.

The unknowns constants C_n^s and C_m^s can be found by imposing constraint conditions at the interfaces between the media. It can be noticed that when the source is placed inside a layer, each interface defines a free-source region, and as a consequence, the tangential components of the electric and magnetic fields across the interface between two media, must be continuous.

If the transmission antenna is an electric current loop as in (3-25), the azimuthal electric field for the superior layers ($n > 0$) must accomplish (3-43), which results in

$$E_{n+1,\phi}\Big|_{z=d_{n+1}} = E_{n\phi}\Big|_{z=d_{n+1}}. \tag{4-33}$$

Substituting (4-31) into the above equation leads to

$$\begin{aligned} &C_{n+1}^{TE} e^{ik_{n+1,z}(d_{n+1}-z')}\left[1+\tilde{R}_{n+1,n+2}^{TE} e^{-2ik_{n+1,z}(d_{n+1}-d_{n+2})}\right] \\ &= C_n^{TE} e^{ik_{n,z}(d_{n+1}-z')}\left[1+\tilde{R}_{n,n+1}^{TE} e^{-2ik_{n,z}(d_{n+1}-d_{n+1})}\right]. \end{aligned} \tag{4-34}$$

After some manipulation, the previous equation can be reduced to

$$C_{n+1}^{TE} = \frac{C_n^{TE}\left[1+\tilde{R}_{n,n+1}^{TE}\right] e^{i(k_{n,z}-k_{n+1,z})(d_{n+1}-z')}}{\left[1+\tilde{R}_{n+1,n+2}^{TE} e^{-2ik_{n+1,z}(d_{n+1}-d_{n+2})}\right]}. \tag{4-35}$$

Similarly, the coefficients for the inferior layers are related by the following equation

$$C_{m-1}^{TE} = \frac{C_m^{TE}\left[1+\tilde{R}_{m,m-1}^{TE}\right] e^{-i(k_{m,z}-k_{m-1,z})(d_{m-1}-z')}}{1+\tilde{R}_{m-1,m-2}^{TE}\, e^{-2ik_{m-1,z}(d_{m-2}-d_{m-1})}}. \tag{4-36}$$

From the previous equation it can be deduced that any coefficient can be determined recursively from the intermediately inferior one (related to the source). However, in order to determinate the coefficients at the source layer, the boundary conditions at the source position ($z = z'$) must be imposed. In a similar form to the procedure employed in Section 3.4.1.1, the application of the boundary condition of (3-43) at $z = z'$ in the source-layer results in

$$C_{0^+}^{TE} = C_{0^-}^{TE}\frac{\left[1+\tilde{R}_{0,-1}^{TE} e^{2ik_{0z}(z'-d_{-1})}\right]}{\left[1+\tilde{R}_{0,+1}^{TE} e^{-2ik_{0,z}(z'-d_{+1})}\right]}. \tag{4-37}$$

On the other hand, employing the boundary condition of (3-46) at $z = z'$ in the source position leads to

$$\left\{C_{0^+}^{TE}\left[1-\tilde{R}_{0,+1}^{TE} e^{-2\imath k_{0,z}(z'-d_{+1})}\right] + C_{0^-}^{TE}\left[1-\tilde{R}_{0,-1}^{TE} e^{2\imath k_{0z}(z'-d_{-1})}\right]\right\} = 2. \tag{4-38}$$

Then, substituting (4-37) into the above equation, the coefficients for the upper and lower sides of the source-layer can be determined with independence

of each other.

$$C_{0^-}^{TE} = \frac{\left[1 + \tilde{R}_{0,+1}^{TE} e^{-2ik_{0,z}(z'-d_{+1})}\right]}{\left[1 - \tilde{R}_{0,+1}^{TE}\tilde{R}_{0,-1}^{TE} e^{2ik_{0,z}(d_{+1}-d_{-1})}\right]}, \tag{4-39}$$

$$C_{0^+}^{TE} = \frac{\left[1 + \tilde{R}_{0,-1}^{TE} e^{2ik_{0z}(z'-d_{-1})}\right]}{\left[1 - \tilde{R}_{0,+1}^{TE}\tilde{R}_{0,-1}^{TE} e^{2ik_{0,z}(d_{+1}-d_{-1})}\right]}. \tag{4-40}$$

For the TM^z mode, the coefficients C_n^{TM}, C_m^{TM}, $C_{0^+}^{TM}$ and $C_{0^+}^{TM}$ present the same format than C_n^{TE}, C_m^{TE}, $C_{0^-}^{TE}$ and $C_{0^+}^{TE}$ in (4-35), (4-36), (4-39), and (4-40), respectively.

Furthermore, as a consequence of the translational invariance of the media in the ρ-direction, the radial source constant $g(k_\rho)$ can be obtained in a similar form as in Section 3.4.1.1, and its result corresponds with the one achieved in (3-62). Therefore, the complete solution for the azimuthal electric (magnetic) field component produced by a uniform and azimuthally independent electric (magnetic) current loop, in a biaxially anisotropic media with one-dimensional piecewise inhomogeneity, can be expressed as

$$A_{n\phi} = -\frac{\omega p_{0\rho}\rho' I}{2}\int_0^\infty dk_\rho \frac{k_\rho}{k_{0z}}\hat{F}_1(k_\rho\rho)\hat{F}_1(k_\rho\rho')\Bigg\{C_n^s e^{ik_{n,z}(z-z')} \times \left[1 + \tilde{R}_{n,n+1}^s e^{-2ik_{n,z}(z-d_{n+1})}\right]\Bigg\}, \tag{4-41}$$

$$A_{m\phi} = -\frac{\omega p_{0\rho}\rho' I}{2}\int_0^\infty dk_\rho \frac{k_\rho}{k_{0z}}\hat{F}_1(k_\rho\rho)\hat{F}_1(k_\rho\rho')\Bigg\{C_m^s e^{-ik_{mz}(z-z')} \times \left[1 + \tilde{R}_{m,m-1}^s e^{2ik_{mz}(z-d_{m-1})}\right]\Bigg\}. \tag{4-42}$$

where $\hat{F}_1(k_\rho\rho)$ is defined as in (3-37), and $A_\phi = E_\phi$, $p = \mu$, $s = \{TE\}$, and $I = I_e$ is the electric current for the TE^z mode. In contrast, $A_\phi = H_\phi$, $p = \epsilon$, $s = \{TM\}$, and $I = I_m$ is the magnetic current for the TM^z mode.

Based on the above formulation, the procedure employed in order to determine the azimuthal components of the field is presented in the flowchart depicted in Fig. 4.5.

It is important to highlight that the inclusion of the conductive cylinder will just modify the radial function $\hat{F}_1(k_\rho\rho)$, which solution corresponds to the one obtained in (3-119).

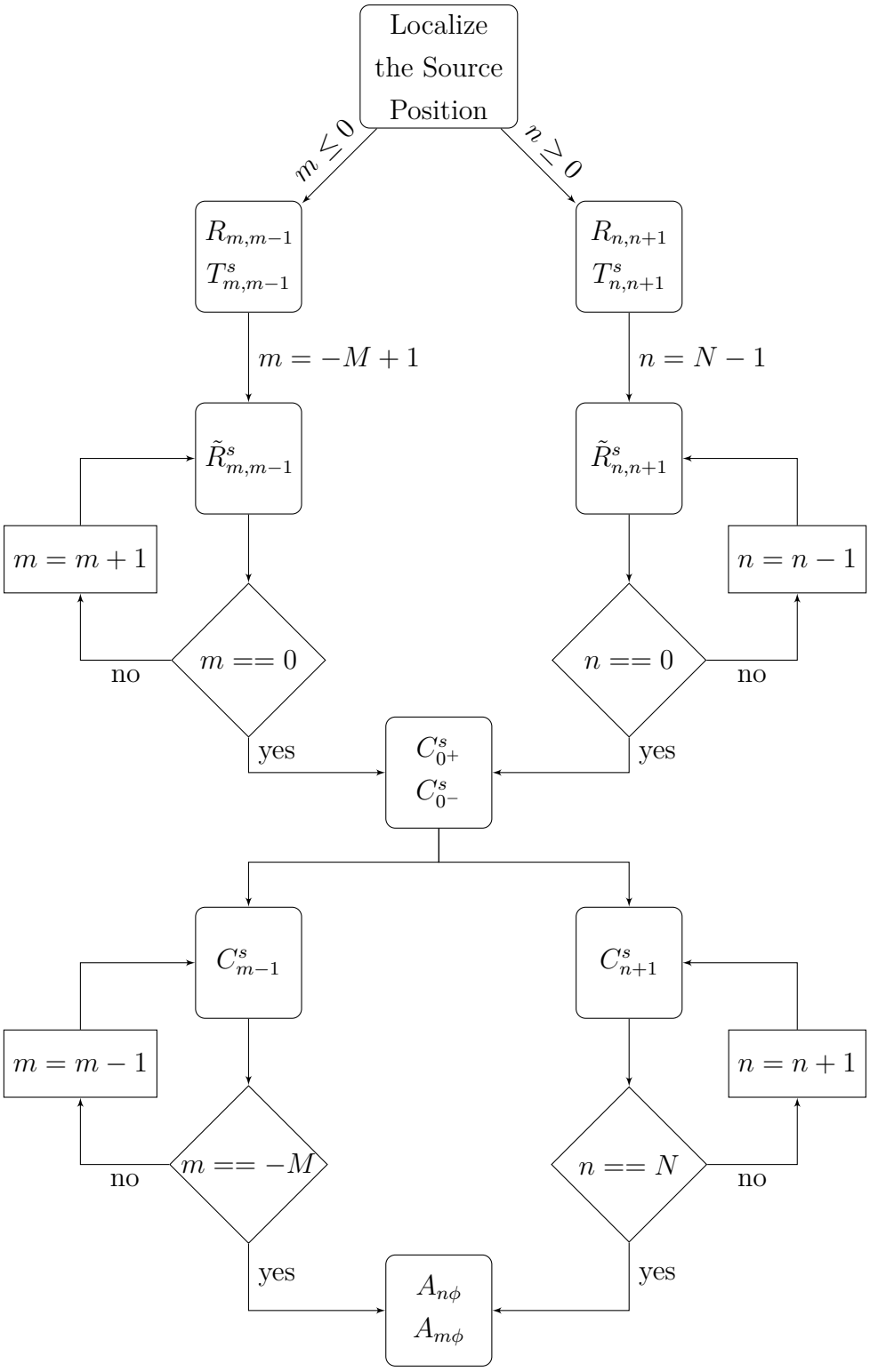

Figure 4.5: Flowchart for the proposed algorithm.

4.4 Numerical Implementation and Analysis

Some simulation were done in order to compare the effects of layer stratification for the wave propagation. Also some cases were considered to

analyze high contrast interfaces and verify the efficiency of the solution. To verify the accuracy of the method under this scenario, it was benchmark the programmed code (via Matlab) against solutions obtained using COMSOL first. Then, some analyses of the results were done.

4.4.1 Half-Space Isotropic Formation

First, consider the lossy isotropic medium with half-space homogeneity, as in Fig. 4.6. The relative dielectric permittivity and relative magnetic permeability in each layer are unity, while the electric conductivity for the media 1 and 2 are 0.5 S/m and 0.1 S/m, respectively. The source, an electric (magnetic) loop of 10 [in] of radio with a constant electric (magnetic) current of 1 A (1 V) is working at 200 kHz, is placed 50 m below the interface. Away from the interface, both media extends to infinity.

In Fig. 4.7 and Fig. 4.8 are presented the amplitude and attenuation, respectively, of the azimuthal component of the electric (magnetic) field E_ϕ (H_ϕ) obtained in Comsol and with the proposed algorithm (identified by the label "Matlab"). It can be appreciated how the computed electric (magnetic) field distribution along axial direction is in excellent agreement with the corresponding results obtained by COMSOL. In both graphs, the slope of the curves changes tends to approach to a parallel line to the horizontal axis. This occurs because the wave encounters a medium with conductivity lower than the one where it is propagating, and as a consequence, its phase velocity increases.

This increment in the phase velocity of the wave also has an impact in the attenuation, as it is shown in Fig. 4.9, which also reduces its values in comparison with the one of the homogeneous medium. If a zoom is applied near the interface, as in Fig. 4.10, it can be seen that before the interface, the attenuation for both modes stays the same. However, when the wave gets closer to the interface, the TM^z field has a considerable increment of the attenuation just before the interface and after the interface it continuous with its linear behavior, but with a reduced slope. On the other side, the TE^z field also

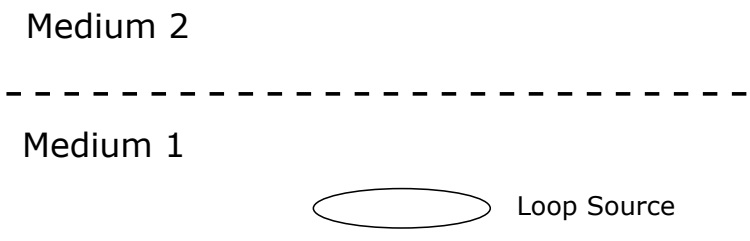

Figure 4.6: Reflection and transmission of a plane wave at an interface

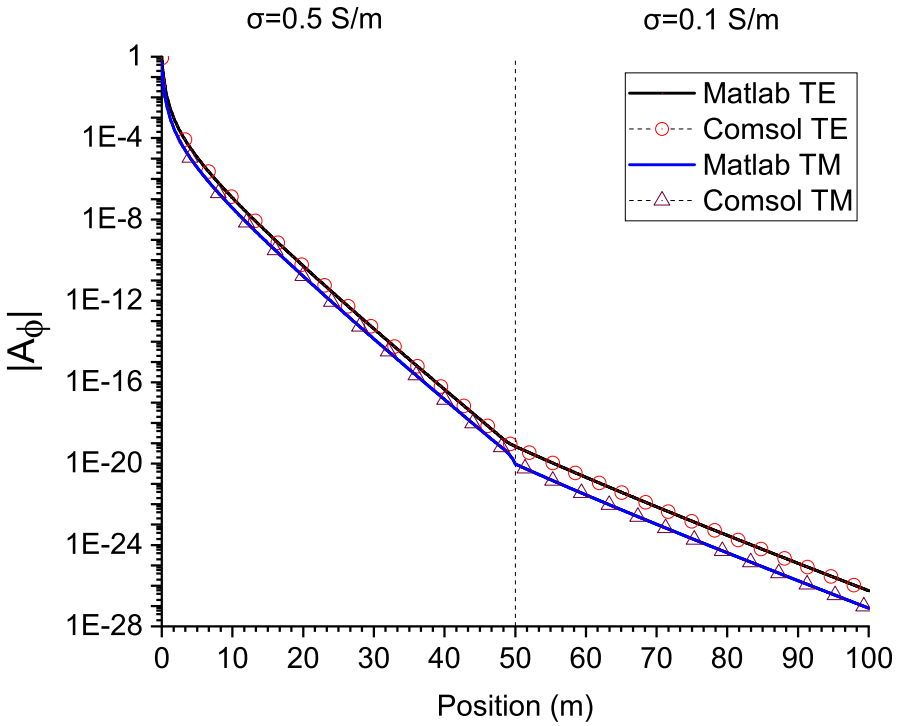

Figure 4.7: Absolute values of the azimuthal components of the electric (magnetic) field E_ϕ (H_ϕ) in a half-space homogeneous isotropic formation (200 kHz) [$\sigma_1 = 0.5$ S/m, $\sigma_2 = 0.1$ S/m)].

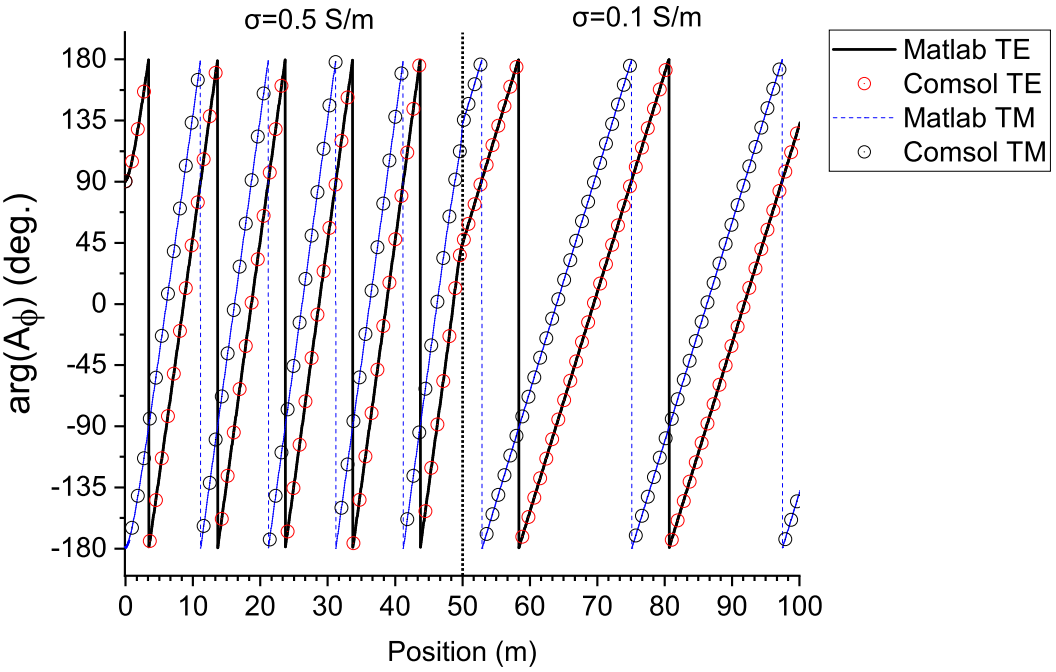

Figure 4.8: Phase values of the azimuthal components of the electric (magnetic) field E_ϕ (H_ϕ) in a half-space homogeneous isotropic formation (200 kHz) [$\sigma_1 = 0.5$ S/m, $\sigma_2 = 0.1$ S/m)].

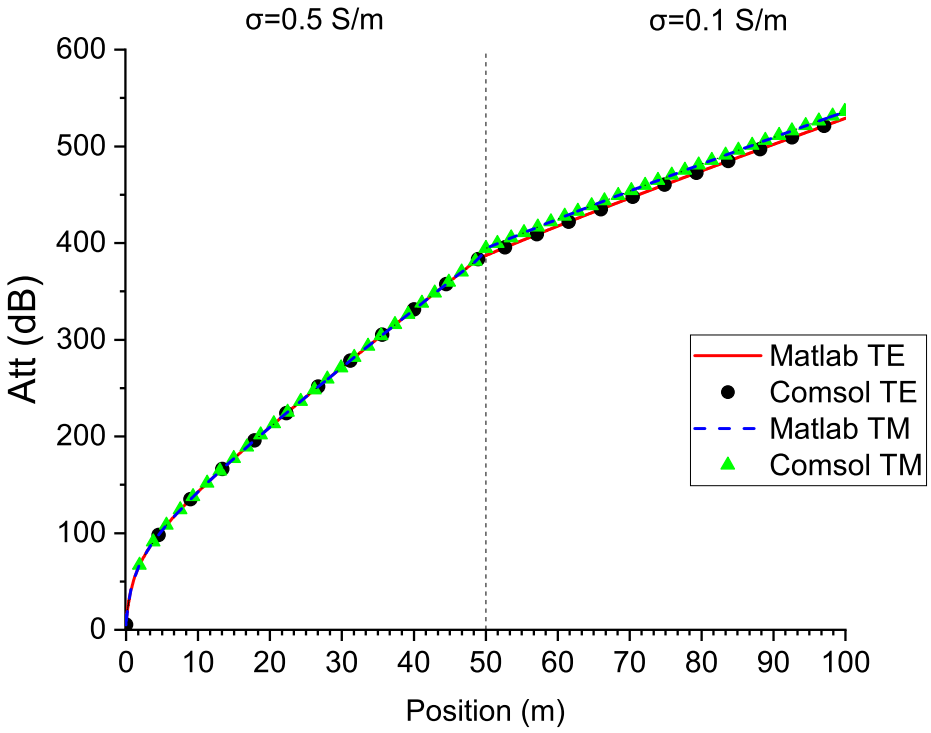

Figure 4.9: Attenuation experimented by the azimuthal components of the electric (magnetic) field E_ϕ (H_ϕ) in a half-space homogeneous isotropic formation (200 kHz) [$\sigma_1 = 0.5$ S/m, $\sigma_2 = 0.1$ S/m].

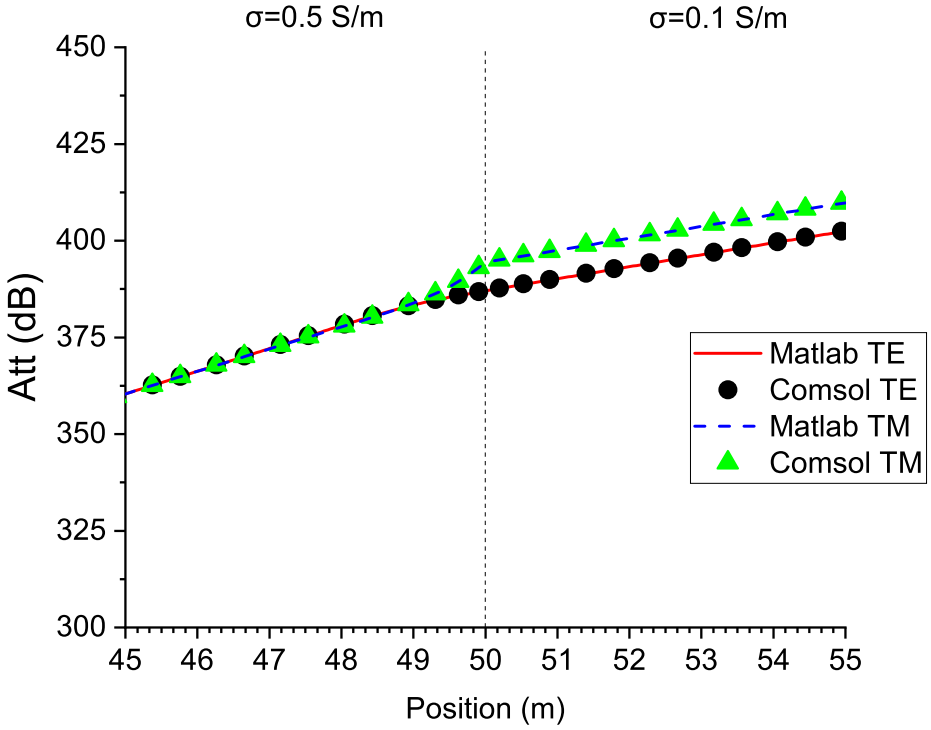

Figure 4.10: Attenuation experimented by the azimuthal components of the electric (magnetic) field E_ϕ (H_ϕ) in a half-space homogeneous isotropic formation (200 kHz) [$\sigma_1 = 0.5$ S/m, $\sigma_2 = 0.1$ S/m].

experiments a reduction in the attenuation but it is more well behaved near the interface.

If the results in Fig. 4.9 are compared with the homogeneous case of Fig. 3.10, it can be appreciated how the attenuation line deviates from its course as the wave enter in the medium with lower attenuation, as in Fig. 4.11,

Table 4.1 compares the computational costs for COMSOL and the employed solution, from which it can be seen that the provided solution is more computationally efficient. It is important to mention that the solution obtained with COMSOL uses a two-dimensional (2D) axisymmetric modeling, which is less computationally intense when compared with the three-dimensional (3D) model.

To verify the accuracy of the implemented solution, a similar scenario was considered, but with the values of conductivities exchanged, to analyze the behavior of a wave that transverse from one medium to another with lower conductivity. Now, the electrical conductivity for the media 1 and 2 are 0.1 S/m

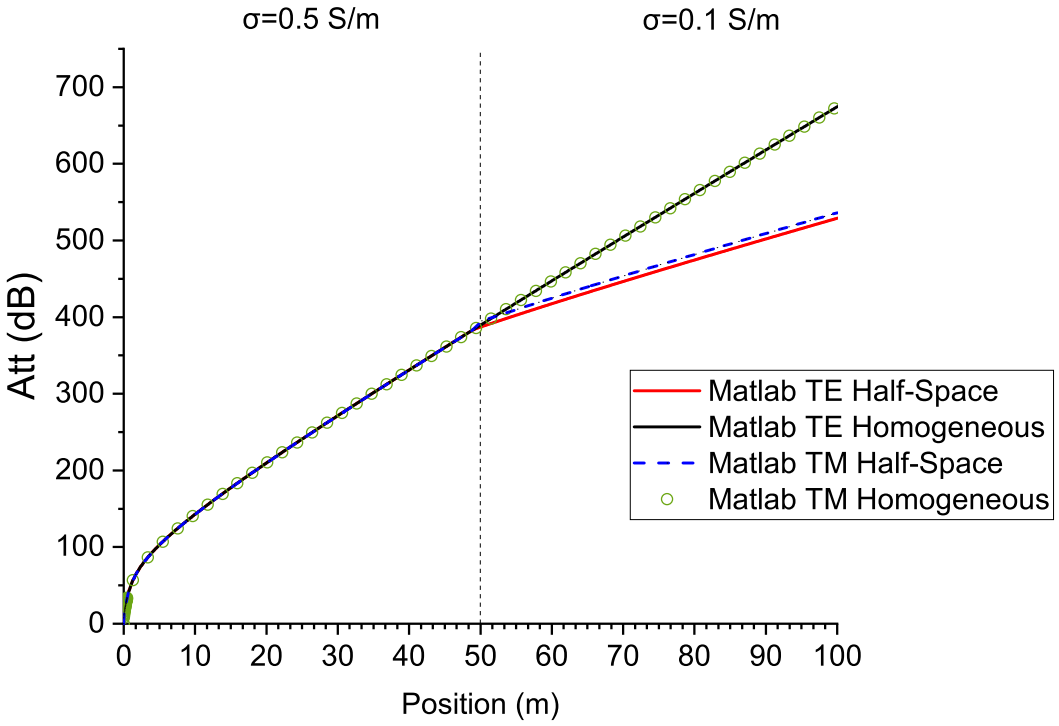

Figure 4.11: Attenuation experimented by the azimuthal components of the electric (magnetic) field E_ϕ (H_ϕ) in a half-space homogeneous isotropic formation [$\sigma_1 = 0.5$ S/m, $\sigma_2 = 0.1$ S/m]. Comparison with the homogeneous case.

	Implemented Solution	COMSOL
Memory cost	20.45 MB	77.24 GB
CPU time	35.27 s	183.7 s

Table 4.1: Computational costs for modeling a half-space isotropic formation.

and 0.5 S/m, respectively.

The results for amplitude, phase and attenuation of the azimuthal component of the electric (magnetic) field E_ϕ (H_ϕ) are shown in Fig. 4.12, Fig. 4.13, and Fig. 4.14, respectively.

If a zoom is applied near the interface, as in Fig. 4.15, it can be seen that in the first layer after the interface, the attenuation for both modes stays the same. However, when the wave gets closer to the interface, the TM^z field has a slight reduction in the attenuation slope, and then, after the interface, the slope is incremented to a value higher than the one that had in the first medium. On the other side, the TE^z field also experiments an increment in the attenuation but its change is more well behaved near the interface.

As in the homogeneous formation the variations in the electromagnetic characteristics at both sides of the interface for different operation frequencies have an important effect in the propagation characteristics. From Fig. 4.16 and Fig. 4.17, it can be noticed that when the values of conductivity at both sides of the interface are of the same order, the attenuation for both modes stays

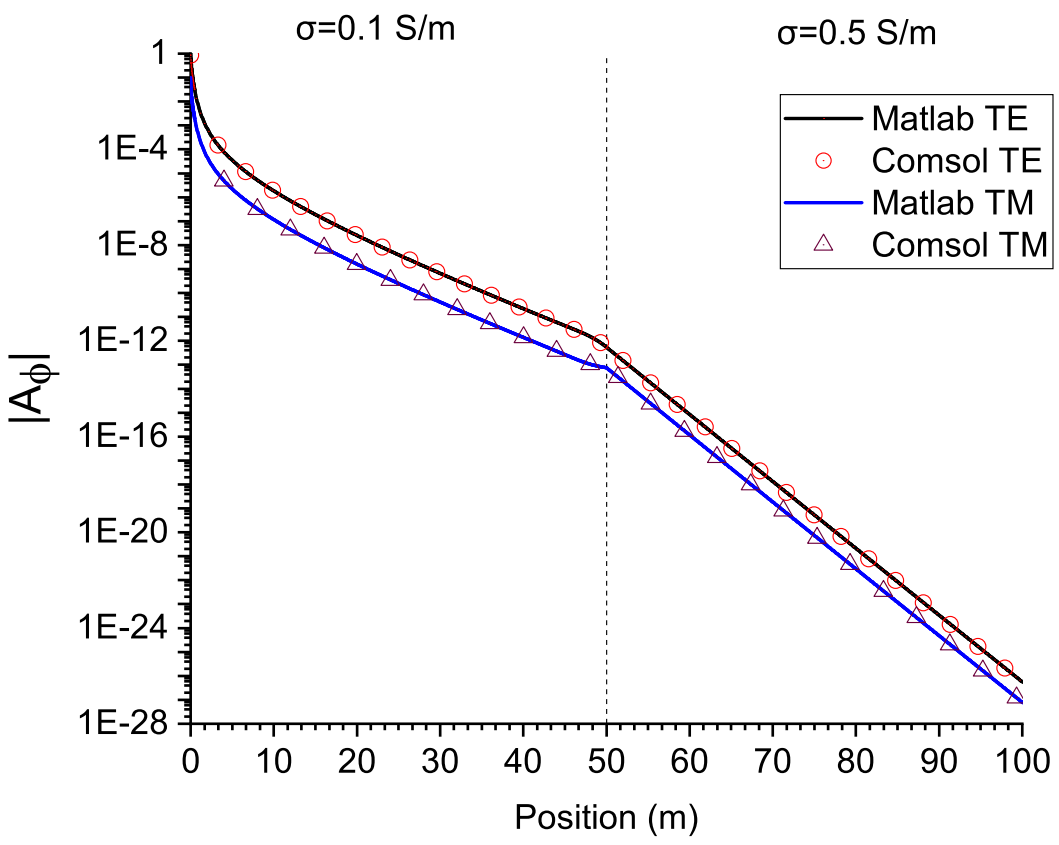

Figure 4.12: Absolute values of the azimuthal components of the electric (magnetic) field E_ϕ (H_ϕ) in a half-space homogeneous isotropic formation (200 kHz) [$\sigma_1 = 0.1$ S/m, $\sigma_2 = 0.5$ S/m].

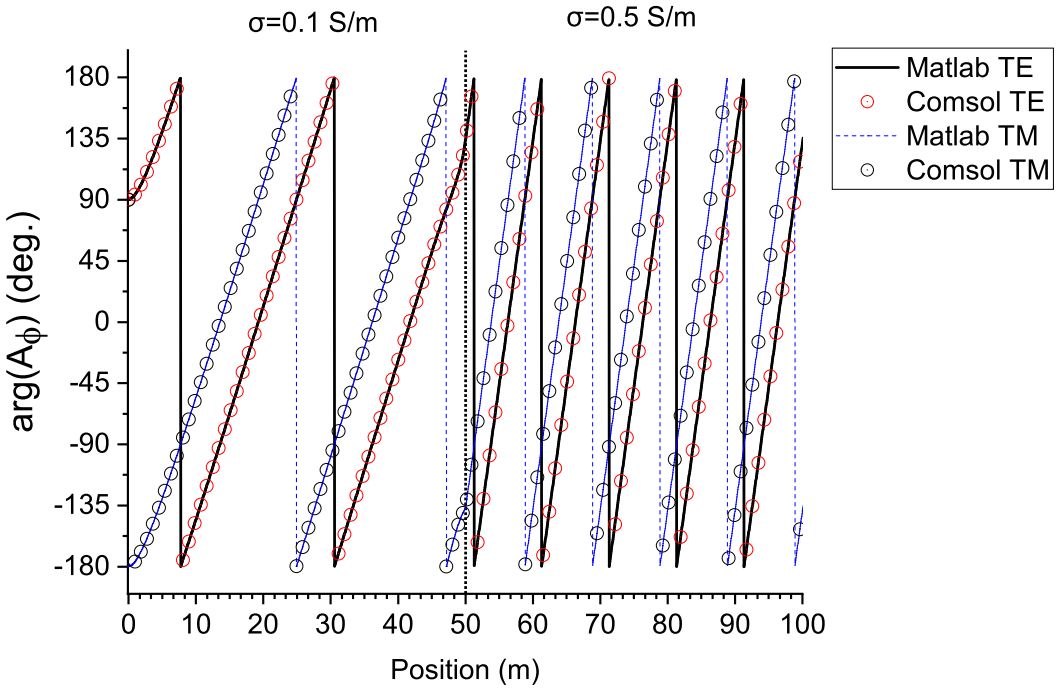

Figure 4.13: Phase values of the azimuthal components of the electric (magnetic) field E_ϕ (H_ϕ) in a half-space homogeneous isotropic formation (200 kHz) [$\sigma_1 = 0.1$ S/m, $\sigma_2 = 0.5$ S/m].

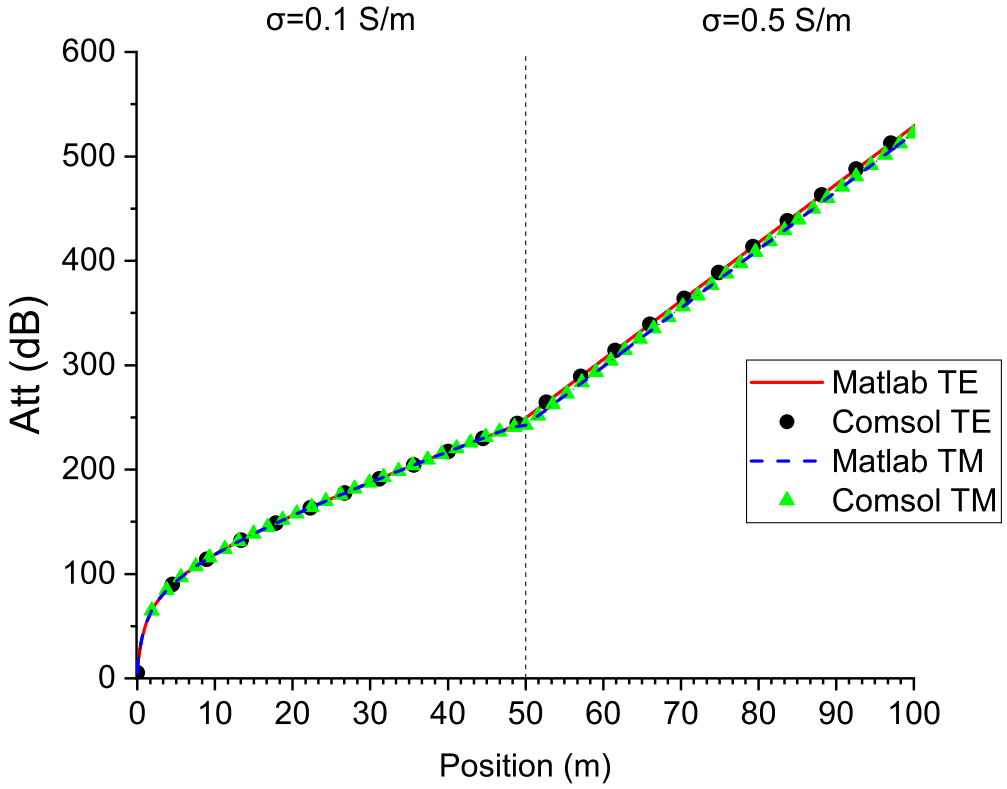

Figure 4.14: Attenuation experimented by the azimuthal components of the electric (magnetic) field E_ϕ (H_ϕ) in a half-space homogeneous isotropic formation (200 kHz) [$\sigma_1 = 0.1$ S/m, $\sigma_2 = 0.5$ S/m].

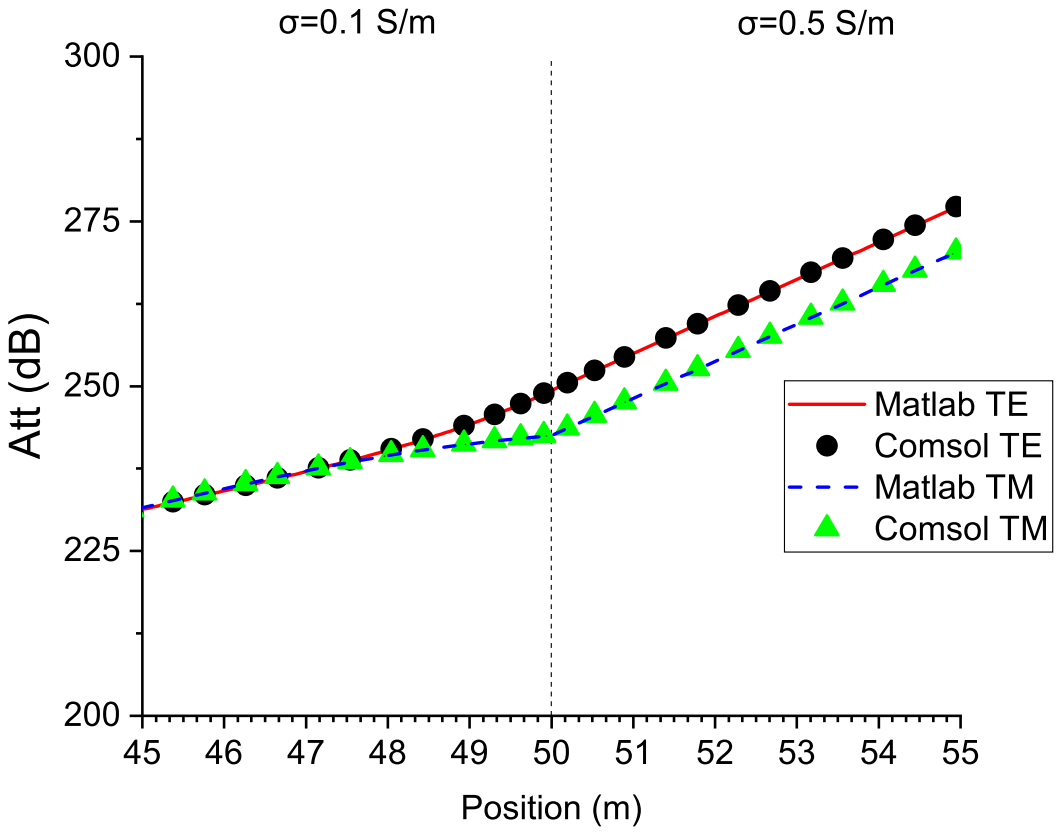

Figure 4.15: Attenuation experimented by the azimuthal components of the electric (magnetic) field E_ϕ (H_ϕ) in a half-space homogeneous isotropic formation at the interface position (200 kHz) [$\sigma_1 = 0.1$ S/m, $\sigma_2 = 0.5$ S/m)].

with the same slope after passing the interface. However, when the contrast of conductivity at both sides of the interface is higher, it can be observed that, for the TM^z mode, the slope of the attenuation curve reduces considerably compared to the TE^z mode for high frequencies.

If the antenna is positioned in the medium with the lower conductivity, with independence of the strength level of the contrast between both media, the attenuation of the TM^z mode stays slightly lower than the TE^z mode, as is shown in Fig. 4.18 and Fig. 4.19.

4.4.1.1 Effects over High Contrast Interfaces

So far, as it is shown in Fig. 4.14, Fig. 4.15, 4.18 and Fig. 4.19, when a wave travels to a medium with higher conductivity, the TE^z field will experiment an attenuation higher than the TM^z field, with a well behavior near the interface. However, when the wave travels to a medium with lower conductivity, as in Fig. 4.9, Fig. 4.10, Fig. 4.16 and Fig. 4.17, the attenuation behavior in the TM^z scenario is quite dependent of the operation frequency and the level of contrast of the conductivity at both sides of the interface.

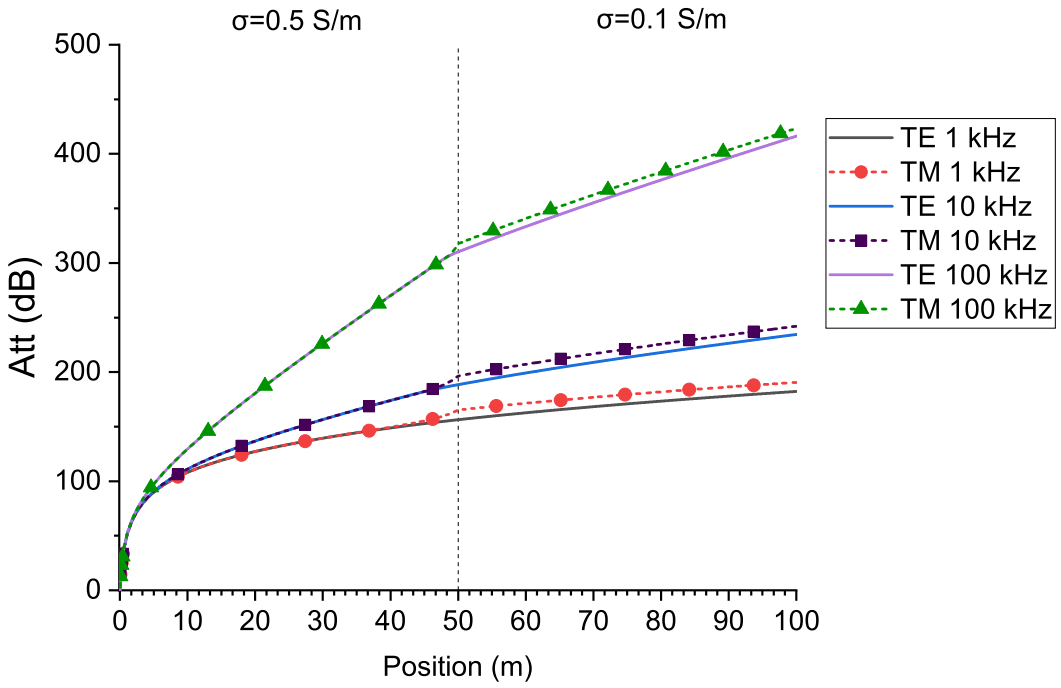

Figure 4.16: Attenuation experimented by the azimuthal components of the electric (magnetic) field E_ϕ (H_ϕ) in a half-space homogeneous isotropic formation as a function of the frequency [$\sigma_1 = 0.5$ S/m, $\sigma_2 = 0.1$ S/m)].

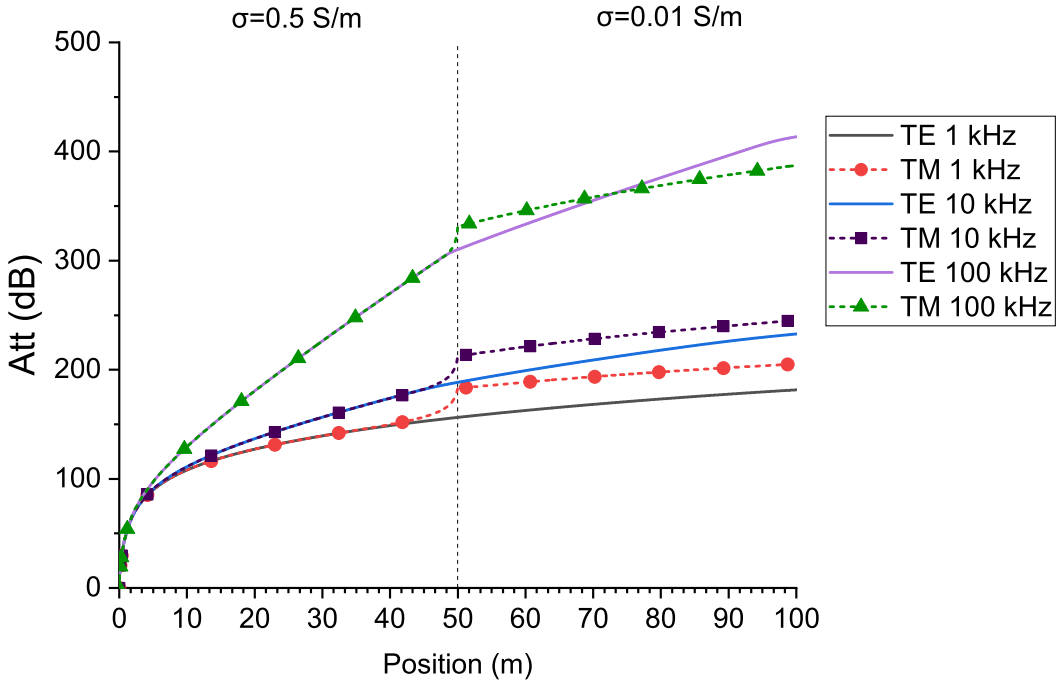

Figure 4.17: Attenuation experimented by the azimuthal components of the electric (magnetic) field E_ϕ (H_ϕ) in a half-space homogeneous isotropic formation as a function of the frequency [$\sigma_1 = 0.5$ S/m, $\sigma_2 = 0.01$ S/m)].

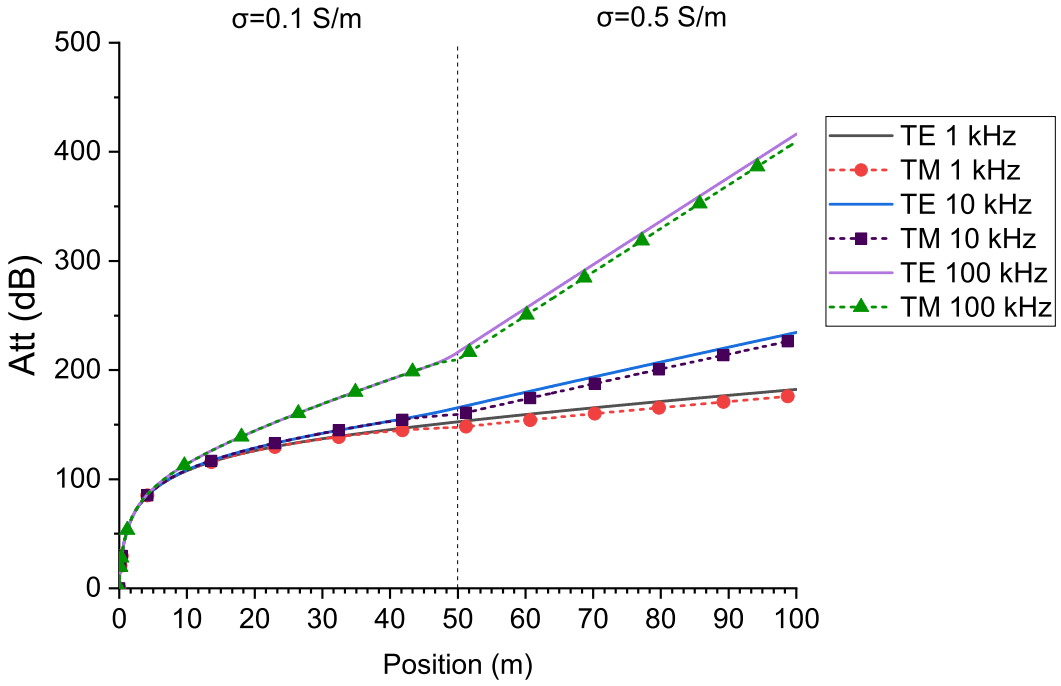

Figure 4.18: Attenuation experimented by the azimuthal components of the electric (magnetic) field E_ϕ (H_ϕ) in a half-space homogeneous isotropic formation as a function of the frequency [$\sigma_1 = 0.1$ S/m, $\sigma_2 = 0.5$ S/m)].

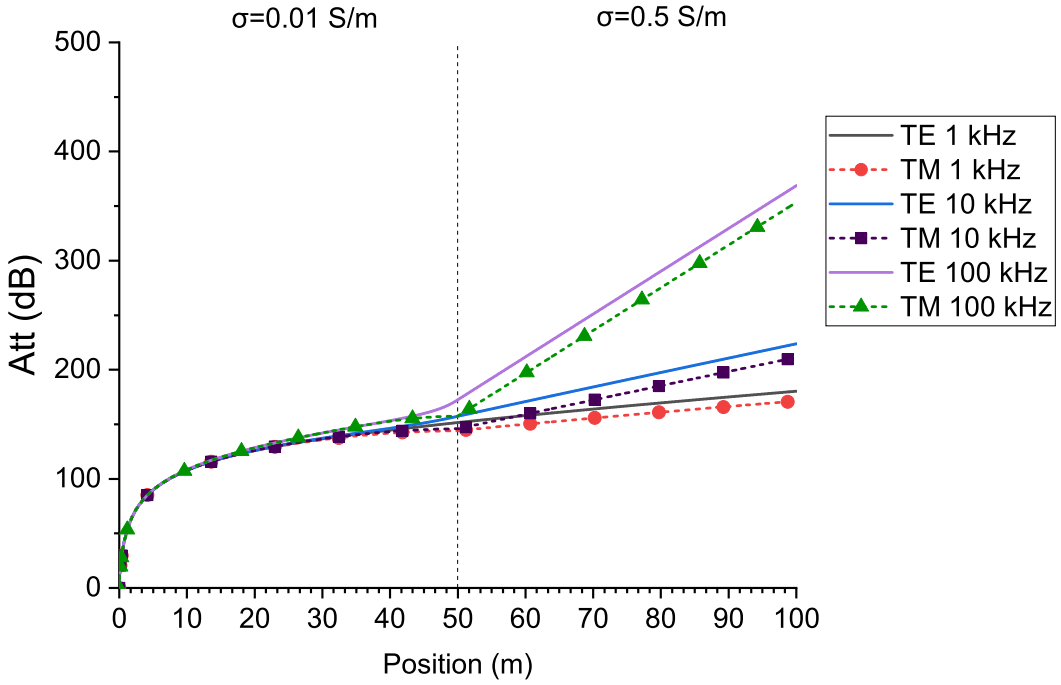

Figure 4.19: Attenuation experimented by the azimuthal components of the electric (magnetic) field E_ϕ (H_ϕ) in a half-space homogeneous isotropic formation as a function of the frequency [$\sigma_1 = 0.01$ S/m, $\sigma_2 = 0.5$ S/m)].

In order to analyze the effects near the interfaces that occur when a TM^z wave propagates to a medium with lower conductivity, some simulations were done with high contrast media and varying the operation frequency. The distance away from the source and the position of the interface were extended, in order to have no source effect involved at the interface position.

In Fig. 4.20 is presented a comparison between the half-space homogeneous scenario and an homogeneous (considering the conductivity for the whole formation as the value at the source layer), for different operation frequencies. For these scenarios with a longer propagation path, and highly conductive media, the obtained results showed an extremely high attenuation of the fields. In order to analyze the electromagnetic effects near the interface, the vertical scale was reduced to concentrate just the values near the interface.

A close look at the interface, as in Fig. 4.21, shows that despite the wave conductivity in the second layer is lower, there is a distance where the attenuation for the half-space homogeneity is higher than for the fully homogeneous medium, as a consequence of the effects or the reflection at the interface. In order to guarantee the continuity equations of the field at both sides of the interface, the azimuthal component of the TM^z reduces drastically when getting close to the interface, and consequently, the attenuation increase over the value it would experiment if there were no interface. It can be noticed that this effect has more repercussion for lower frequencies.

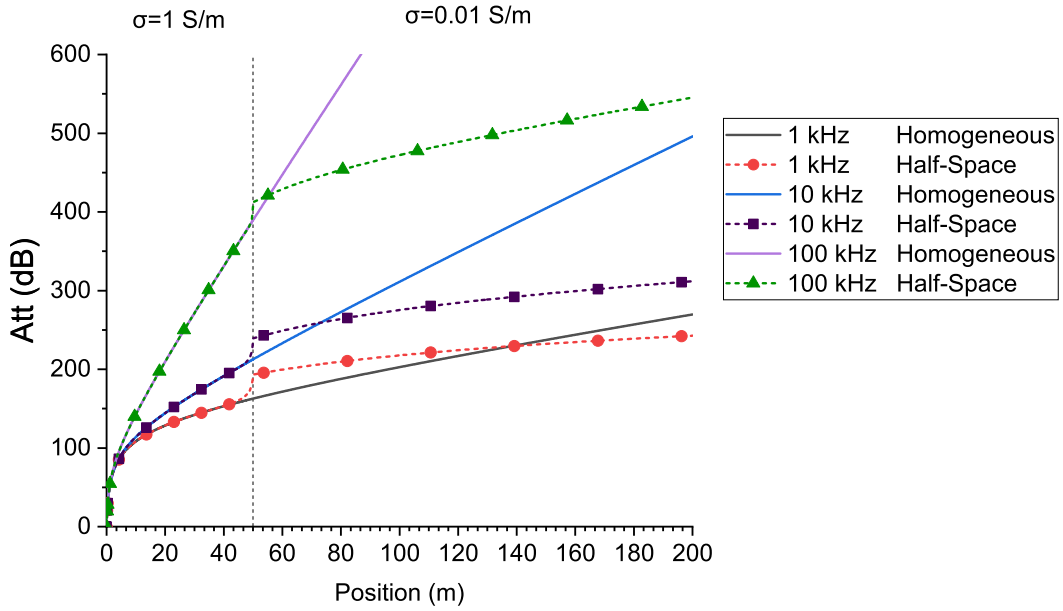

Figure 4.20: Attenuation experimented by the azimuthal components of the magnetic field H_ϕ in a half-space homogeneous isotropic formation as a function of the frequency [$\sigma_1 = 1$ S/m, $\sigma_2 = 10^{-2}$ S/m]. Comparison with the homogeneous case.

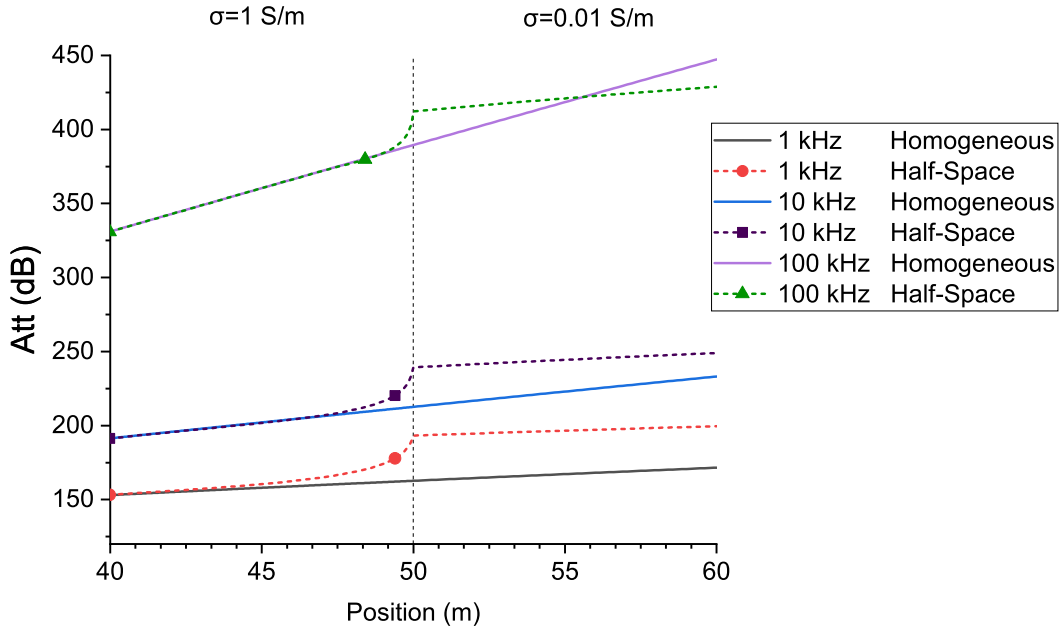

Figure 4.21: A closer look to the attenuation experimented by the azimuthal components of the magnetic field H_ϕ in a half-space homogeneous isotropic formation as a function of the frequency [$\sigma_1 = 1$ S/m, $\sigma_2 = 10^{-2}$ S/m]. Comparison with the homogeneous case.

When the conductivity value of the second layer is reduced, as in Fig. 4.22, the electromagnetic contrast between both media increases. Consequently, it can be appreciated that the distance the wave travels in the second medium until achieve a lower level of attenuation that in the homogeneous scenario also increases. This distance reaches 10 m and 130 m for 100 kHz and 1 kHz, respectively. A fast calculation can be done to determine this distance, as in

$$\Delta Z \approx \frac{\ln |T_{ij}|}{k''_{2z} - k''_{1z}}. \tag{4-43}$$

where ΔZ is the distance away from the interface where both curves (fully homogeneous and half-space homogeneous media) intersect, T_{ij} is the transmission coefficient from medium i to j, and k''_{iz} represents the imaginary part of the axial wave number at the i layer.

4.4.2 Multi-Layer Isotropic Formation

The provided solution can be applied to a media with several layers, without increasing considerable the computational requirements. In Fig. 4.23 is presented a media with three layers, where the conductivity value is reducing from one layer to another. The operation frequency is 1 kHz. It can be appreciated how the TM^z mode is the most affected due to the reflections

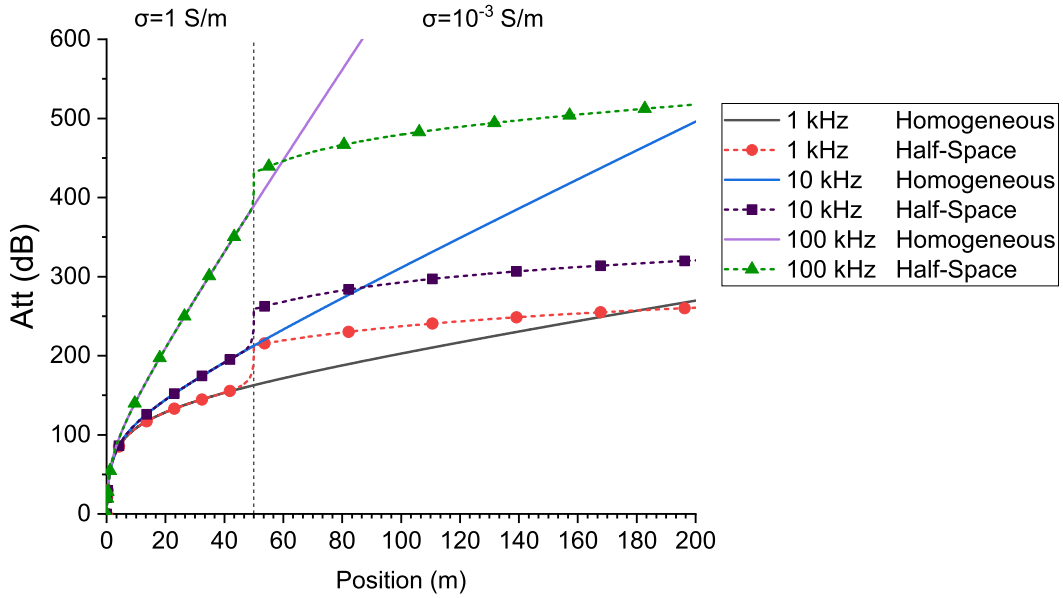

Figure 4.22: Attenuation experimented by the azimuthal components of the magnetic field H_ϕ in a half-space homogeneous isotropic formation as a function of the frequency [$\sigma_1 = 1$ S/m, $\sigma_2 = 10^{-3}$ S/m]. Comparison with the homogeneous case.

at the interfaces.

Also, an scenario considering two layers with the same characteristics, and between them a layer with a reduced conductivity value was considered. It can be observed in Fig. 4.24 how in the first interface the value of attenuation for the TM^z mode jumps high until it get more stable, but when getting close to the second interface reduce slightly, and after the interface starts growing again.

In Fig. 4.24 the attenuation curve of the TM^z along the three layer formation has the same behavior as the homogeneous case for the regions before and after the interface. In order to verify with more precision the previous scenario, a longer distance was considered, as in Fig. 4.25. It can be observed how the attenuation approximates to the homogeneous case, but it is not the same. This occurred as a consequence of the second interface be placed at a distance near the ΔZ. If the second interface is placed farther from the source, as in Fig. 4.26, it can be clearly appreciated how the attenuation is not following the curve of the homogeneous case after the wave go through a transition to a layer with lower conductivity and then through another layer with the same conductivity as the first one.

Further scenarios were analyzed considering the presence of the metallic rod into the formation, and including the effects of the anisotropy.

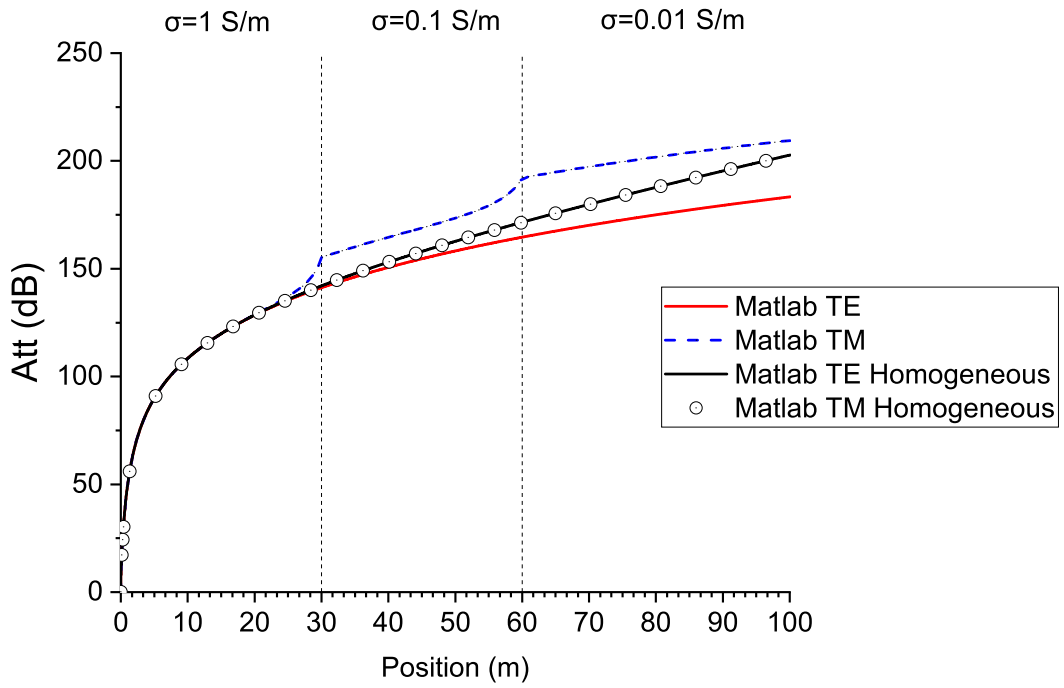

Figure 4.23: Attenuation experimented by the azimuthal components of the electric (magnetic) field E_ϕ (H_ϕ) in a three-layer isotropic formation [$\sigma_1 = 1$ S/m, $\sigma_2 = 10^{-1}$ S/m, $\sigma_3 = 10^{-2}$ S/m] (1 kHz). Comparison with the homogeneous case.

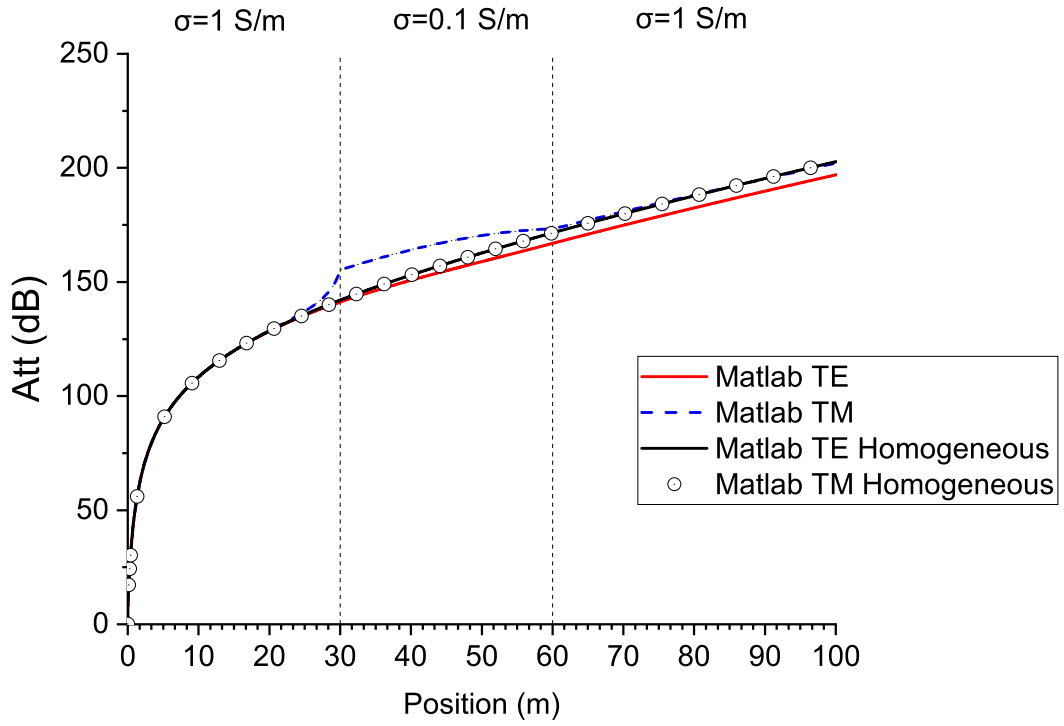

Figure 4.24: Attenuation experimented by the azimuthal components of the magnetic field H_ϕ in a three-layer isotropic formation [$\sigma_1 = 1$ S/m, $\sigma_2 = 10^{-1}$ S/m, $\sigma_3 = 1$ S/m] (1 kHz). Comparison with the homogeneous case.

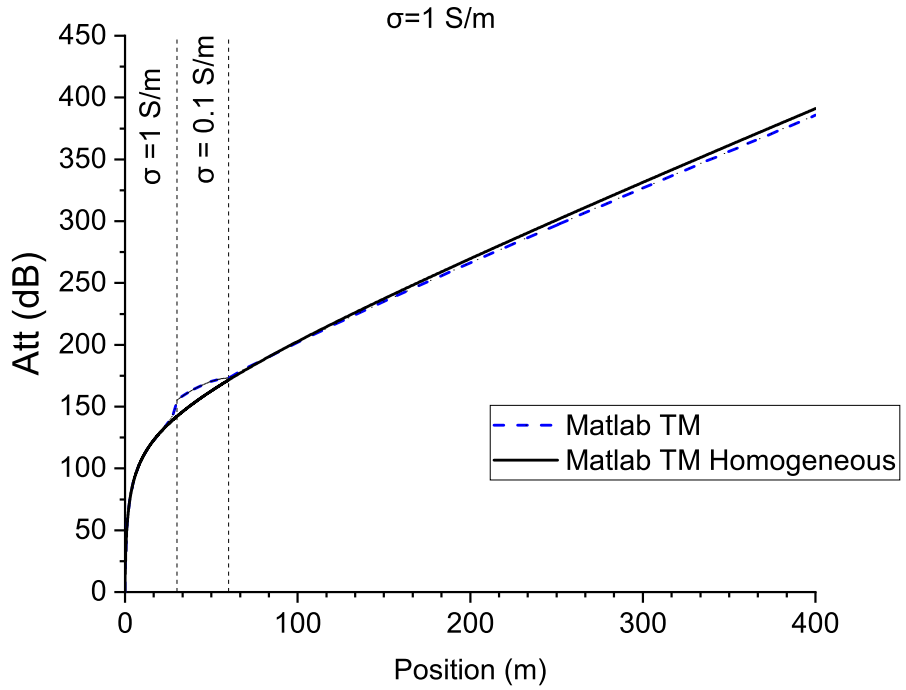

Figure 4.25: Attenuation experimented by the azimuthal components of the magnetic field H_ϕ in a three-layer isotropic formation [$\sigma_1 = 1$ S/m, $\sigma_2 = 10^{-1}$ S/m, $\sigma_3 = 1$ S/m] (1 kHz). Comparison with the homogeneous case.

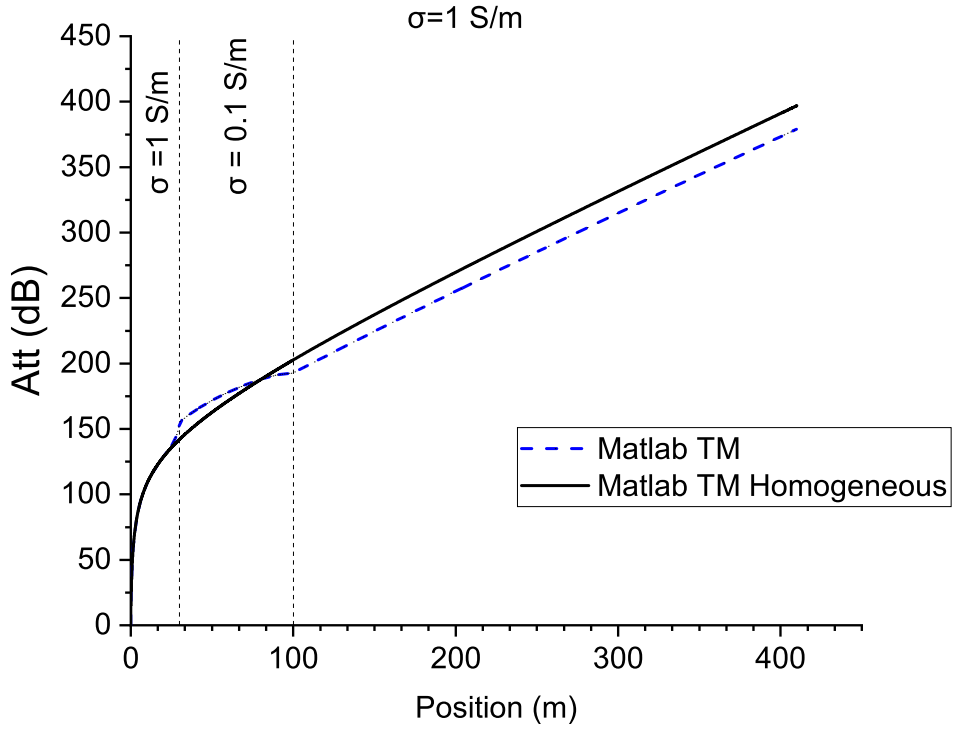

Figure 4.26: Attenuation experimented by the azimuthal components of the magnetic field H_ϕ in a three-layer isotropic formation [$\sigma_1 = 1$ S/m, $\sigma_2 = 10^{-1}$ S/m, $\sigma_3 = 1$ S/m] (1 kHz). Comparison with the homogeneous case.

4.4.3
Multi-Layer Biaxial Anisotropic Formation

In this section, a more complex media is analyzed. For this scenario, the media contains three biaxially anisotropic layers with a metal pipe of radio $a = 9$ [in]. The metal pipe is modeled as a PEC, without loss of generality. The operation frequency is 1 kHz. For simplicity, as in the previous sections, the relative dielectric and magnetic constants are unity. The conductivity tensors for the layers $1, 2, 3$ take the values of:

$$\bar{\bar{\sigma}}_1 = \begin{bmatrix} 0.5 & 0 & 0 \\ 0 & 0.3 & 0 \\ 0 & 0 & 0.1 \end{bmatrix}, \; \bar{\bar{\sigma}}_2 = \begin{bmatrix} 0.3 & 0 & 0 \\ 0 & 0.1 & 0 \\ 0 & 0 & 0.5 \end{bmatrix}, \; \bar{\bar{\sigma}}_3 = \begin{bmatrix} 0.1 & 0 & 0 \\ 0 & 0.5 & 0 \\ 0 & 0 & 0.3 \end{bmatrix}, \quad (4\text{-}44)$$

respectively.

The absolute value, phase, and attenuation, for the azimuthal component of the electrical E_ϕ (magnetic H_ϕ) for this scenario, are shown in Fig. 4.27, Fig. 4.28, and Fig. 4.29, respectively.

The results obtained from the three graphs are almost the same, except

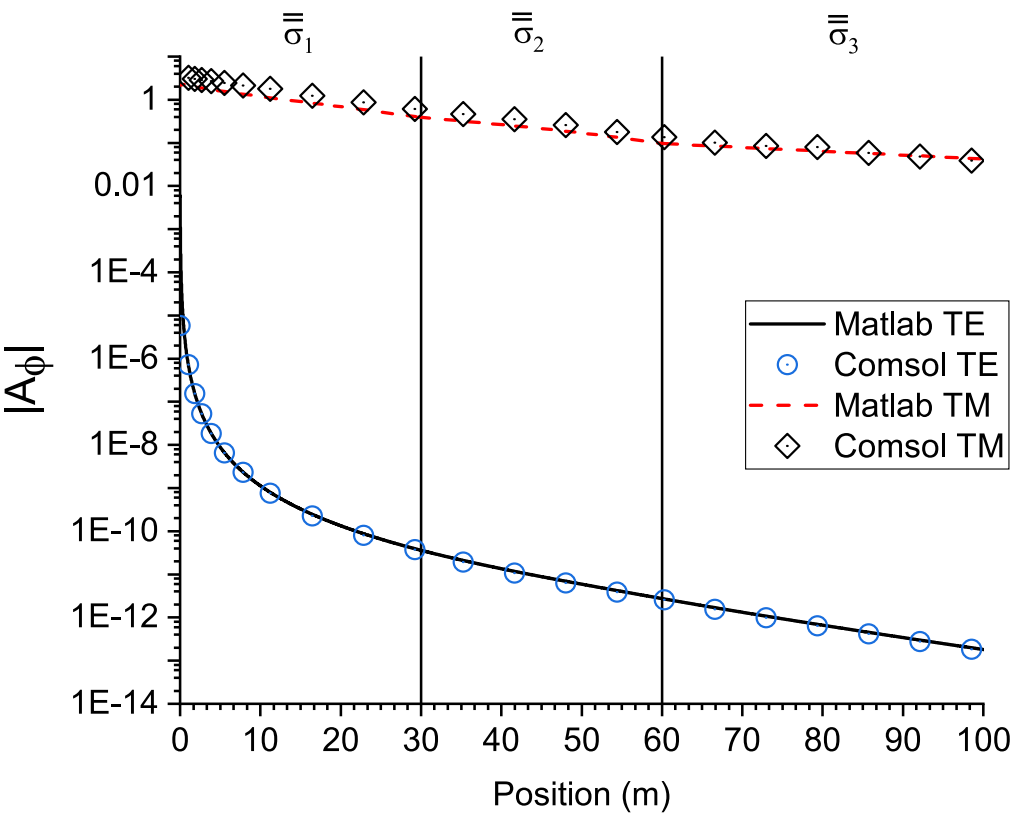

Figure 4.27: Absolute values of the azimuthal components of the electric (magnetic) field E_ϕ (H_ϕ) in a three-layer biaxially anisotropic formation (1 kHz).

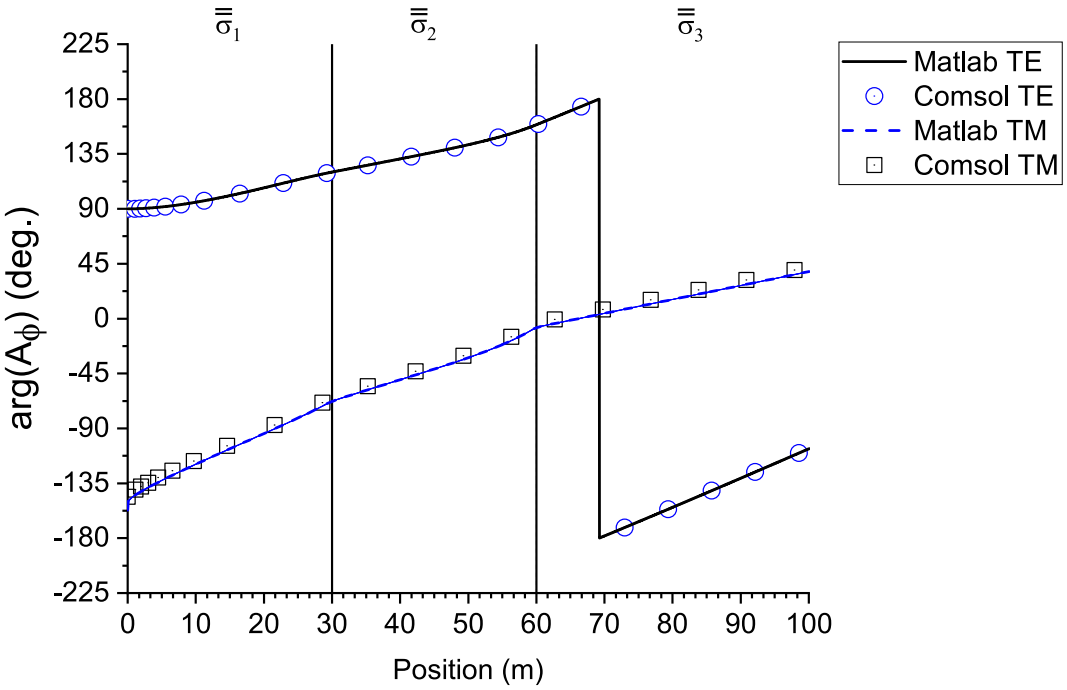

Figure 4.28: Phase values of the azimuthal components of the electric (magnetic) field E_ϕ (H_ϕ) in a three-layer biaxially anisotropic formation (1 kHz).

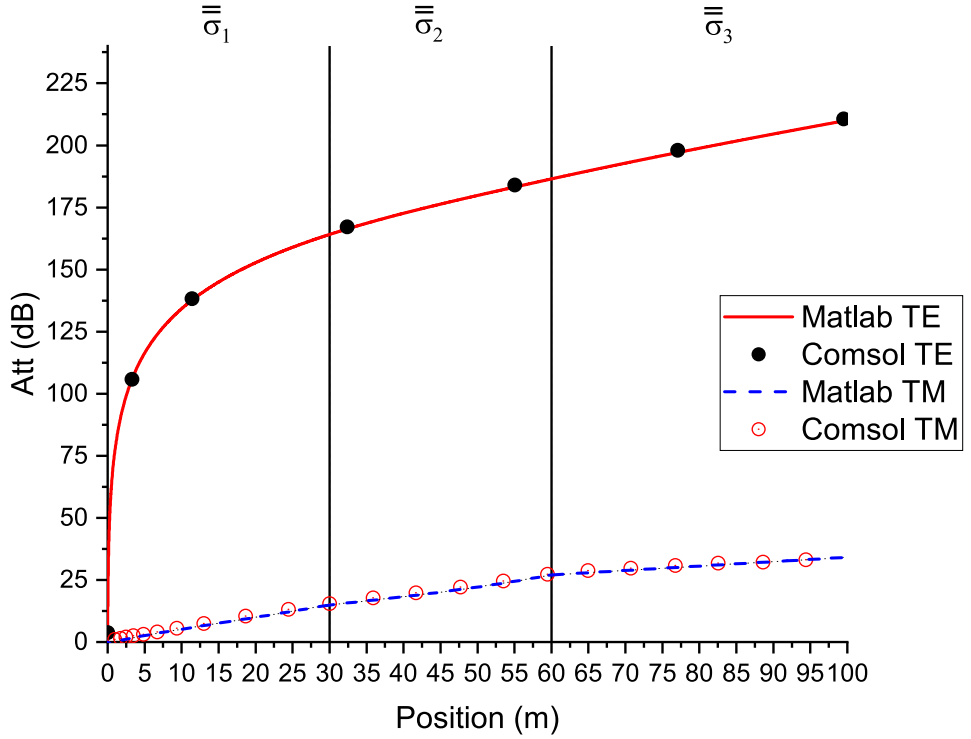

Figure 4.29: Attenuation experimented by the azimuthal components of the magnetic field H_ϕ in a three-layer biaxially anisotropic formation (1 kHz).

for the absolute value of the magnetic field (TM^z mode) whose solution in COMSOL is slightly higher (0.8 A/m) near the source than the solution obtained with MATLAB. This discrepancy must be due to the construction

of the grid in COMSOL, as a consequence of the extreme variations in the conductivity, the inhomogeneity, anisotropy and the presence of a metallic rod (PEC) with small radius. However, away from the source, the behavior of the absolute value of the fields obtained with COMSOL leads to the same results of the proposed solution.

A second configuration scenario was analyzed. In this case, the anisotropy for each layer is characterized by a high contrast of the conductivity values in each direction of the anisotropic tensor. In order to test the efficiency of the proposed solution, the anisotropic tensor for the layers above the source are formed by a permutation of the conductivity values from the conductivity tensor in the source layer, as follows

$$\bar{\bar{\sigma}}_1 = \begin{bmatrix} 1 & 0 & 0 \\ 0 & 0.1 & 0 \\ 0 & 0 & 0.01 \end{bmatrix}, \; \bar{\bar{\sigma}}_2 = \begin{bmatrix} 0.01 & 0 & 0 \\ 0 & 1 & 0 \\ 0 & 0 & 0.1 \end{bmatrix}, \; \bar{\bar{\sigma}}_3 = \begin{bmatrix} 0.1 & 0 & 0 \\ 0 & 0.01 & 0 \\ 0 & 0 & 1 \end{bmatrix}. \quad (4\text{-}45)$$

The absolute value, phase, and attenuation, for azimuthal component of the electrical E_ϕ (magnetic H_ϕ) for this example, are shown in Fig. 4.30, Fig. 4.31, and Fig. 4.32, respectively. It is observed that although totally

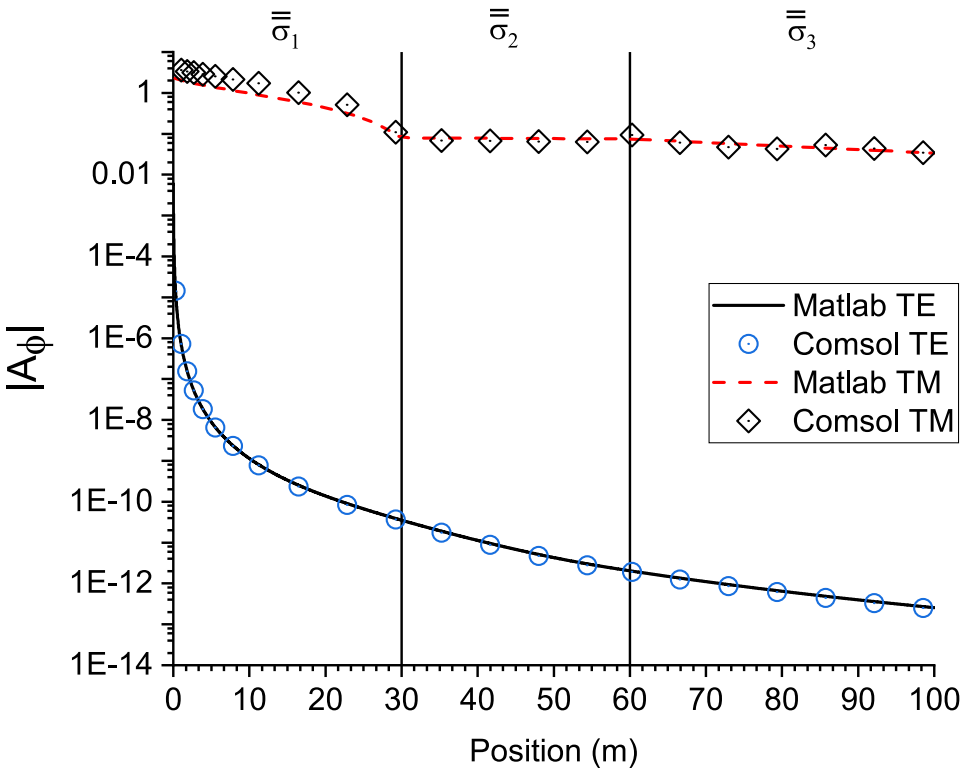

Figure 4.30: Absolute values of the azimuthal components of the electric (magnetic) field E_ϕ (H_ϕ) in a three-layer biaxially anisotropic formation (1 kHz).

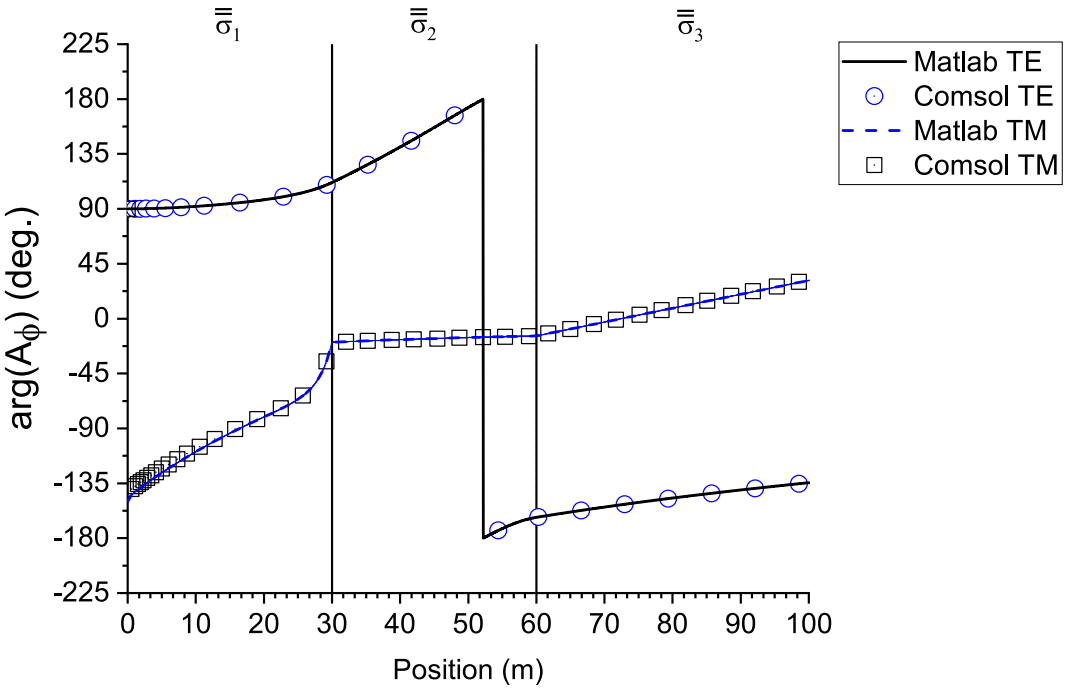

Figure 4.31: Phase values of the azimuthal components of the electric (magnetic) field E_ϕ (H_ϕ) in a three-layer biaxially anisotropic formation (1 kHz).

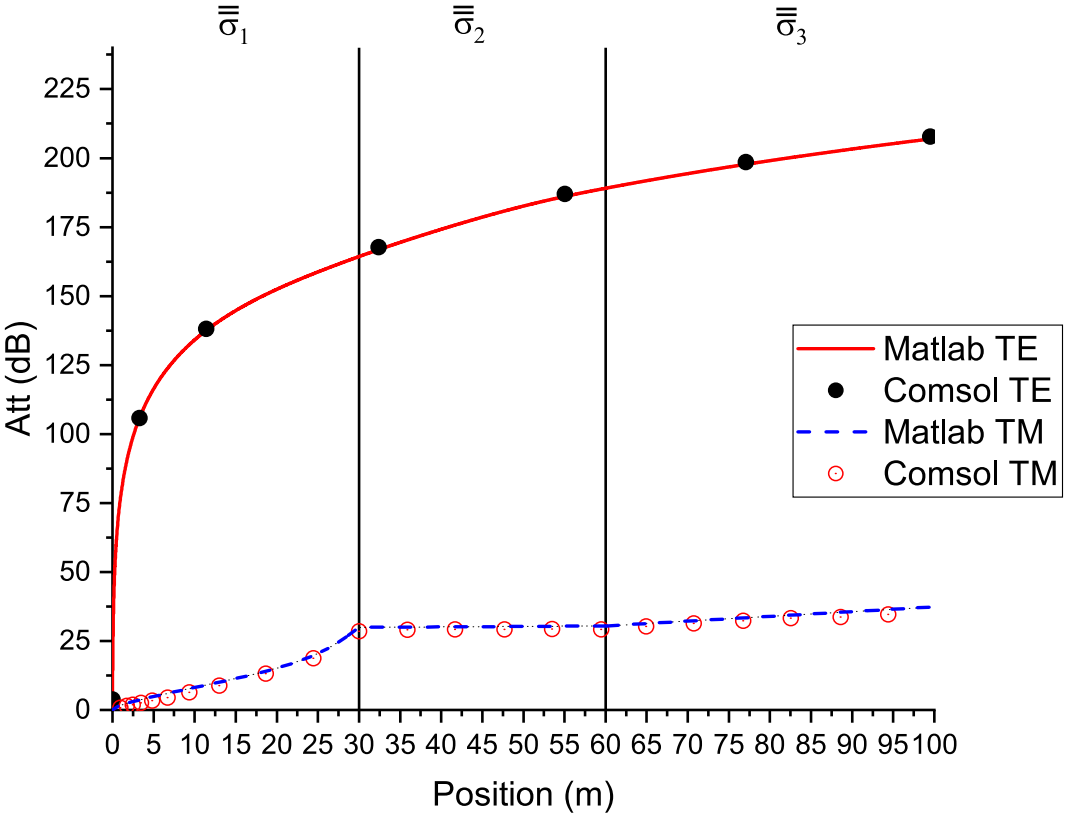

Figure 4.32: Attenuation experimented by the azimuthal components of the magnetic field H_ϕ in a three-layer biaxially anisotropic formation (1 kHz).

different methods are used, both solution converge to almost the same results, except for the region near the source. For the regions away from the source

the fields tend to approximate to the solution achieved, which validates the presented formulation.

4.5 Conclusions

In this chapter, a stable semi-analytical algorithm was formulated to model the effects of wave propagation in inhomogeneous anisotropic formation with axial stratifications. This algorithm is an extended version of the one presented in Chapter 3 to include the effects of multiple interfaces, which lead to multiple reflections and transmission of waves along the formation. This has important applications for modeling stratified media such as oil well formations.

It was analyzed the effect of high-contrast interfaces, its frequency-dependent characteristics, and its different behavior for TE^z and TM^z waves. TE^z mode showed to have a smooth well behavior near the interface, while, for TM^z mode, the field experiments a fast variation (in order to guarantee the continuity of the fields) at the interface.

Several validation cases were presented in order to verify the accuracy and efficiency of the proposed solution when compared with finite-element solver. A very good agreement was observed, and also, the solution proposed in this work requires just a fraction of the computational resources used by the FEM Comsol solver. As an important contribution for modeling telemetry in deep oil well, it was observed that the propagation of TM^z fields is advised when a metallic cylinder (representing the casing of the oil well) is present.

5
Impedance Boundary Condition Modeling

5.1
Introduction

The analysis of the electromagnetic field incidence on an object, considered as a perfect metal requires considerable simplification on the initial problem. The previous analysis in Section 3.5 using a PEC boundary condition is a simple approximation and easy to implement. However, it is also very restrictive by the assumption of planar surfaces and semi-infinite thickness. Considering the PEC as the limiting case of a real conductor, it is natural to expect that the PEC condition is also a particular case of a more general approximate boundary condition, relating electromagnetic quantities at conductor/dielectric interfaces [58].

In this chapter is presented an analysis and the mathematical formulation of the electromagnetic field responses assessing the lossy characteristics of real metallic tubes by means of the modeling of an approximated impedance boundary condition. Some numerical results are presented in order to verify the accuracy and efficiency of the proposed solution.

5.2
Implementing the Impedance Boundary Condition

Approximate boundary conditions can be very helpful in simplifying the analytical and numerical solution of scattering problems, avoiding the need to calculate the fields within the body, and therefore, reducing the computational efforts. The surface impedance boundary condition of first order attributed to Mykola Leontovych in [60] is widely used to simulate the material properties of a scatterer, and even for a non-planar surface of a material it is customary to use the boundary condition derived from a consideration of an homogeneous half space.

Leontovych boundary condition for a metallic cylindric embedded in a homogeneous medium may be written in the form of [60]

$$\hat{n} \times (\hat{n} \times \mathbf{E}) = -Z_c \, \hat{n} \times \mathbf{H}, \tag{5-1}$$

where the components of the electric and magnetic fields tangential to the surface are related by the surface impedance Z_c of the conductor. This surface impedance is equal to the wave impedance in the conductor, and can be expressed as

$$Z_c = \sqrt{\frac{\mu_c}{\epsilon_c}} = \sqrt{\frac{\mu_c}{\epsilon_0 \epsilon_{r,c} + i\sigma_c/\omega}}. \tag{5-2}$$

Most of practical conductors have a very high conductivity at the frequency of interest, and therefore, the real and imaginary parts of the permittivity of the conductor achieve the condition

$$\frac{\sigma_c}{\omega \epsilon_0 \epsilon_{r,c}} >> 1. \tag{5-3}$$

Under this approximation, (5-2) can be reduced to

$$Z_c \approx (1-i)\sqrt{\frac{\omega \mu_c}{2\sigma_c}}. \tag{5-4}$$

The most significant parameter characterizing the propagation in the conductor is the skin depth, which can be expressed as in (3-107), in terms of which, the wave impedance is given by

$$Z_c \approx (1-i)\frac{\omega \mu_c \delta}{2}. \tag{5-5}$$

The use of (5-1) for the TE^z mode, leads to

$$E_\phi\Big|_{\rho=a} = -Z_c H_z\Big|_{\rho=a}, \tag{5-6}$$

meanwhile for TM^z mode, (5-1) reduces to

$$E_z\Big|_{\rho=a} = Z_c H_\phi\Big|_{\rho=a}. \tag{5-7}$$

After substituting the axial component of the magnetic field and the azimuthal component of the electric field of (3-97) into (5-6) for the TE^z and evaluating for $\rho = a$, it is obtained

$$\begin{aligned} -\frac{\omega \mu_\rho \rho' I_e}{2} \int_0^\infty dk_\rho \frac{k_\rho}{k_z} \hat{F}_1(k_\rho a)\hat{F}_1(k_\rho \rho') e^{ik_z|z-z'|} \\ = -Z_c \frac{i\rho' \mu_\rho I_e}{2\mu_z} \int_0^\infty dk_\rho \, \frac{k_\rho^2}{k_z} \hat{F}_0(k_\rho a)\hat{F}_1(k_\rho \rho') e^{ik_z|z-z'|}. \end{aligned} \tag{5-8}$$

After some manipulations in the above equation, a more simplified form

can be achieved

$$\int_0^\infty dk_\rho \frac{k_\rho}{k_z}\left[\omega\hat{F}_1(k_\rho a) - Z_c\frac{ik_\rho}{\mu_z}\hat{F}_0(k_\rho a)\right]\hat{F}_1(k_\rho\rho')e^{ik_z|z-z'|} = 0. \tag{5-9}$$

In order to satisfy the last equation with independence of the z-component, the terms between the square brackets must vanish, as in

$$\left[\omega\hat{F}_1(k_\rho a) - Z_c\frac{ik_\rho}{\mu_z}\hat{F}_0(k_\rho a)\right] = 0. \tag{5-10}$$

When substituting (3-99) into the above equation,

$$\left[\frac{J_1(k_\rho a) + BY_1(k_\rho a)}{\sqrt{1+B^2}} - Z_c\frac{ik_\rho}{\omega\mu_z}\frac{J_0(k_\rho a) + BY_0(k_\rho a)}{\sqrt{1+B^2}}\right] = 0. \tag{5-11}$$

Resolving last equation for B, leads to obtain the restriction that guarantee the impedance boundary condition, that is

$$B^{TE} = -\frac{J_1(k_\rho a) - Z_c\frac{ik_\rho}{\omega\mu_z}J_0(k_\rho a)}{Y_1(k_\rho a) - Z_c\frac{ik_\rho}{\omega\mu_z}Y_0(k_\rho a)}. \tag{5-12}$$

Similarly, solving (5-7) for the TM^z mode following the last procedure, the radial constant B takes the form of

$$B^{TM} = -\frac{J_0(k_\rho a) - Z_c\frac{\omega\epsilon_z}{ik_\rho}J_1(k_\rho a)}{Y_0(k_\rho a) - Z_c\frac{\omega\epsilon_z}{ik_\rho}Y_1(k_\rho a)}. \tag{5-13}$$

The solutions for the fields components still have the form of (3-97) and (3-98) for the TE^z and TM^z modes, respectively. In order to ensure the Leontovych boundary condition at the conductor surface, the radial function described by (3-99), must be defined with the radial constant B specified by (5-12) and (5-13) for each mode.

It can be noticed from (5-12) and (5-13) that in cases when considering the conductor as a PEC, for which Z_s vanishes, it is obtained the solutions of (3-112) and (3-117) for the TE^z and TM^z modes, respectively. This ensures consistency between the solution formulated with the Leontovych boundary condition and the one obtained previously for the PEC case.

Equations (5-12) and (5-13) can be reduced to a more compact form

$$B = -\frac{J_1(k_\rho a) - Z_g J_0(k_\rho a)}{Y_1(k_\rho a) - Z_g Y_0(k_\rho a)}. \tag{5-14}$$

where the generalized impedance coefficient Z_g can be defined as

$$Z_g^{TE} = Z_c \frac{ik_\rho}{\omega \mu_z}, \tag{5-15}$$

for the TE^z mode, and

$$Z_g^{TM} = \frac{ik_\rho}{Z_c \omega \epsilon_z}, \tag{5-16}$$

for the TM^z mode.

5.3 Numerical Implementation and Analysis

In this subsection, a few examples are presented to analyze the algorithm discussed in Section 5.2. In these scenarios, the surface of the metallic mandrel is modeled by an impedance boundary condition. In these scenarios, the source is modeled as a 10-in-radius electric (magnetic) coil with a constant electric (magnetic) current of 1 A (1 V) placed surrounding a lossy metal pipe with radio $a = 9$ [in]. The lossy metallic cylinder is characterized by its electrical conductivity (σ_c). The relative dielectric and magnetic constants are unity, i.e., the vacuum dielectric and magnetic constants.

The modeling in COMSOL of the surface boundary condition was implemented with the transition boundary condition (TBC) function. This BC is appropriated for metallic structures with a thickness relatively smaller than the characteristic size and curvature of the objects being modeled [44].

5.3.1 Homogeneous Isotropic Formation

Consider first an electric (magnetic) coil operating at 1 kHz in a lossy homogeneous medium described by its electrical conductivity with value 0.5 S/m.

In Fig. 5.1, Fig. 5.2 and Fig. 5.3, are presented the amplitude, phase and attenuation, respectively, of the azimuthal component of the electric (magnetic) field E_ϕ (magnetic H_ϕ) obtained using Comsol and the implemented solution (identified by the label "Matlab"). In the figures, two values for the electrical conductivity (σ_c) of the metallic cylinder are presented for comparison. The high concentration of samples in the COMSOL solution near the source is a consequence of the reduced grid size selected.

The agreement between the results obtained by using the two methods is satisfactory. It can be noticed that the increment on the value of the conductivity of the metallic cylinder slightly alter the behavior of the TM^z solution, while the TE^z vary considerably. For the TE^z mode, it can be

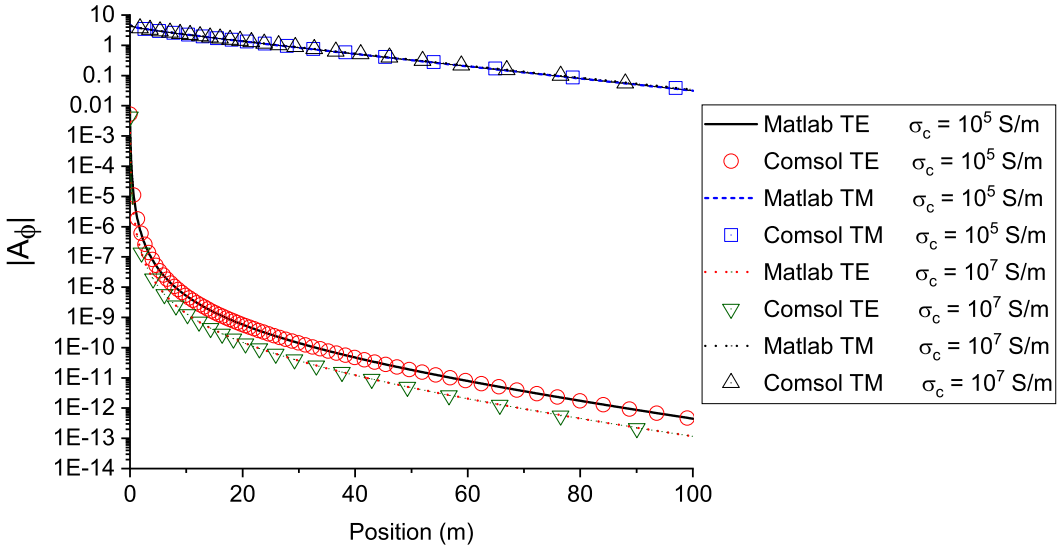

Figure 5.1: Absolute values of the azimuthal components of the electric (magnetic) field E_ϕ (H_ϕ) in an isotropic formation with an embedded lossy metallic cylinder (1 kHz).

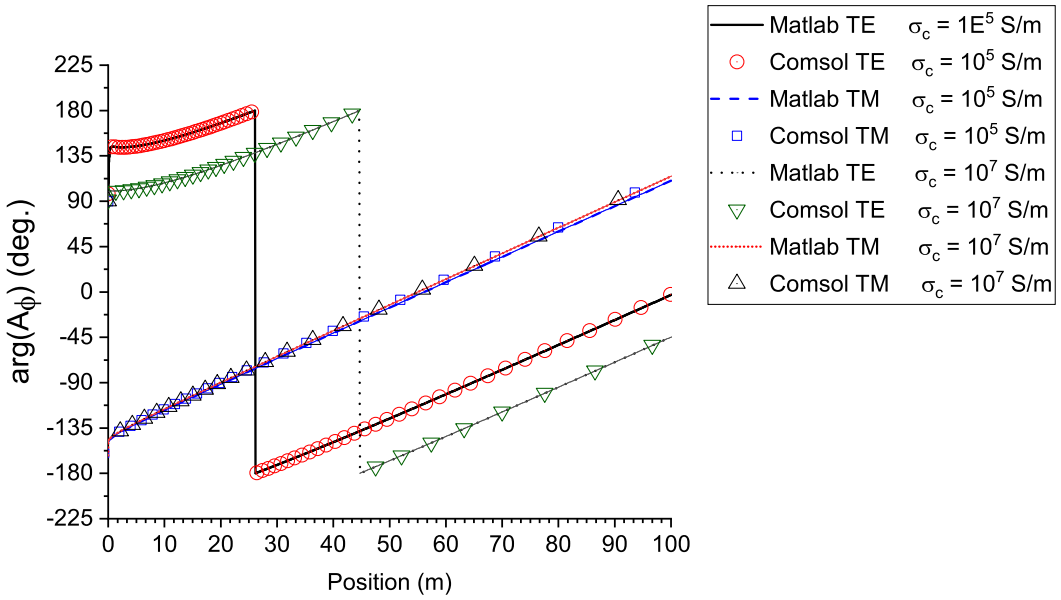

Figure 5.2: Phase values of the azimuthal components of the electric (magnetic) field E_ϕ (H_ϕ) in an isotropic formation with an embedded lossy metallic cylinder (1 kHz).

observed that the experimented attenuation increases with the increase of the conductivity of the metallic surface. This agree with the concluded in Section 3.5, where the TE^z mode is more attenuated with the presence of the embedded cylinder (PEC). As the conductivity of the cylinder reduces, it approximates to the conductivity of the surrounding media, wich favor the propagation for TE^z waves.

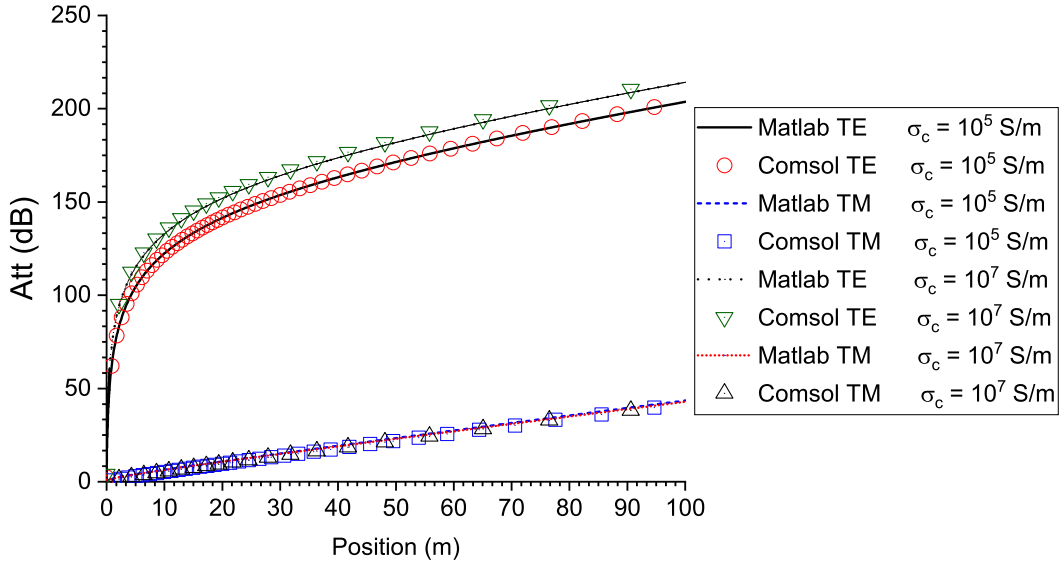

Figure 5.3: Attenuation experimented by the azimuthal components of the electric (magnetic) field E_ϕ (H_ϕ) in an isotropic formation with an embedded lossy metallic cylinder (1 kHz).

In Table 5.1 is presented a comparison between the computational costs for COMSOL and the proposed solution. It can be noticed the superior computational performance of the semi-analytical solution proposed in this dissertation. As in the previous chapters, the solution obtained with COMSOL uses a two-dimensional (2D) axisymmetric modeling, which is less computationally intense when compared with the three-dimensional (3D) model.

In order to analyze the frequency-conductivity dependence of the impedance model, different tests were performed, including extreme cases such as high conductivity contrast between mandrel/pipe and formation. In Fig. 5.4, Fig. 5.5, Fig. 5.6, and Fig. 5.7 are shown a comparison for different frequencies and conductivity values of the metallic cylinder. It can be appreciated for the TM^z mode that the attenuation for the different frequencies does not vary with the conductivity of the metallic cylinder, and is very similar to the PEC case. This just holds for conductivity values of the metallic cylinder above 10^4 S/m, under that, the waves experimented an attenuation higher than the PEC scenario. For the TE^z mode, the worst scenario (higher attenuation), is the PEC case. The greater the losses of the metallic cylinder, the lower is the

	Implemented Solution	COMSOL
Memory cost	16.3 MB	58.01 GB
CPU time	25.84 s	125 s

Table 5.1: Computational costs of modeling a homogeneous isotropic formation surrounding a lossy cylindrical metallic rod.

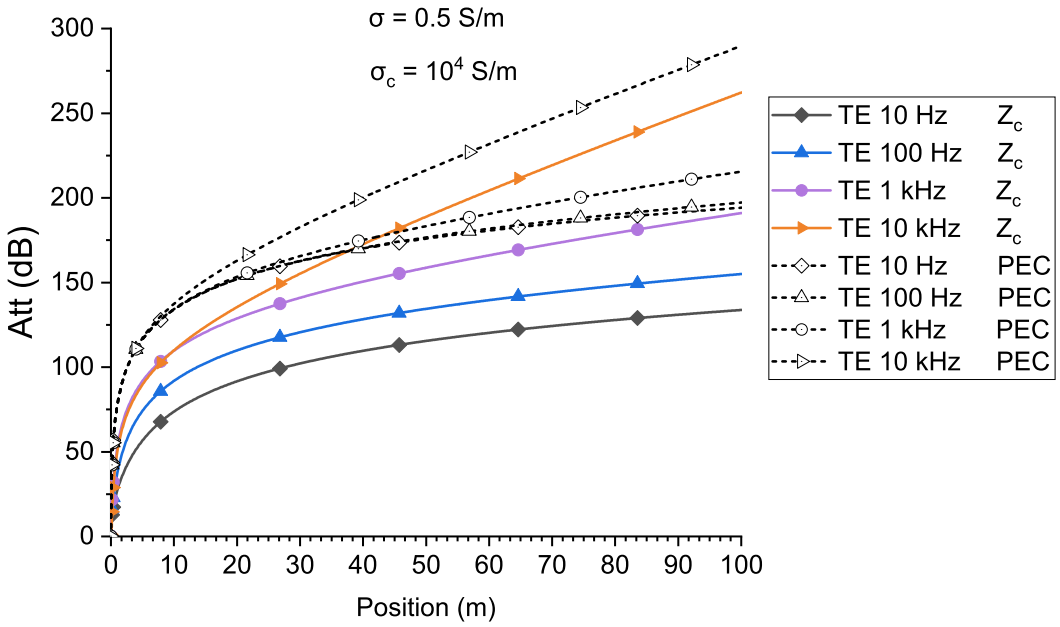

Figure 5.4: Attenuation experimented by the azimuthal component of the electric field E_ϕ in an isotropic formation with an embedded lossy metallic cylinder as a function of the frequency ($\sigma_c = 10^4$ S/m).

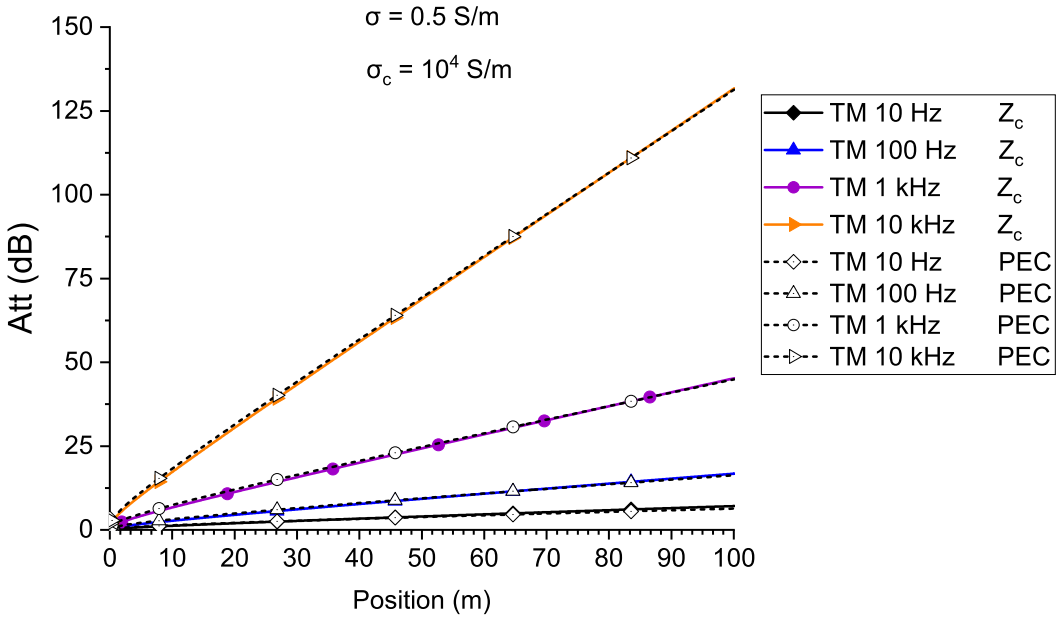

Figure 5.5: Attenuation experimented by the azimuthal component of the magnetic field H_ϕ in an isotropic formation with an embedded lossy metallic cylinder as a function of the frequency ($\sigma_c = 10^4$ S/m).

attenuation experimented. As the conductivity of the metallic cylinder gets higher, the attenuation for the TE^z approximates to the PEC scenario.

Another test was done by setting a smaller value of the conductivity of the medium to 10^{-3} S/m, while keeping $\sigma_c = 10^6$ S/m. The results, presented in Fig. 5.8 and Fig. 5.9, show that the attenuation for the different frequencies

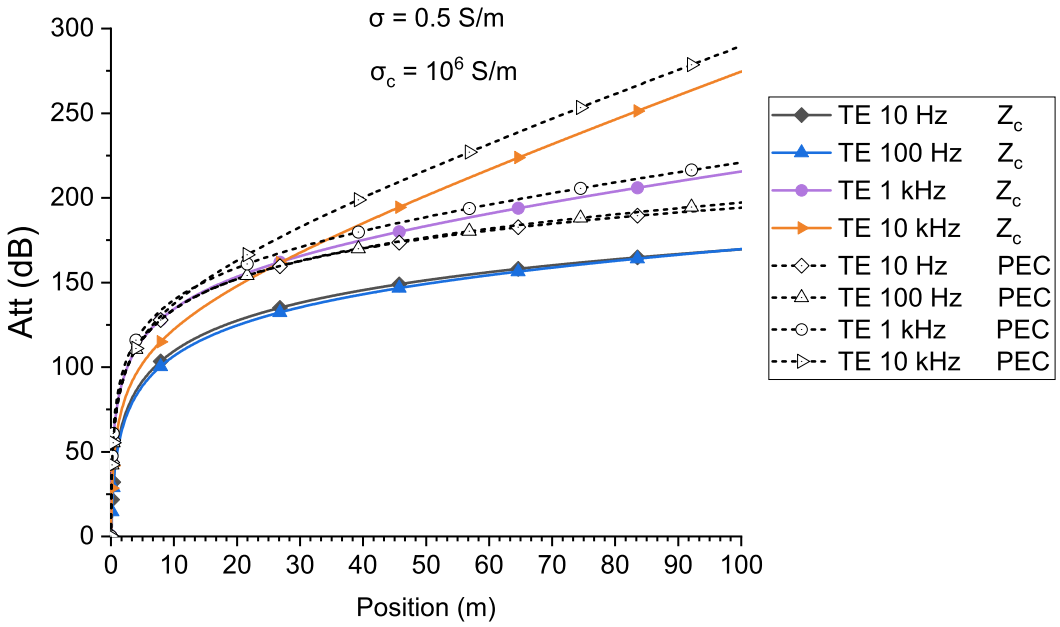

Figure 5.6: Attenuation experimented by the azimuthal component of the electric field E_ϕ in an isotropic formation with an embedded lossy metallic cylinder as a function of the frequency ($\sigma_c = 10^6$ S/m).

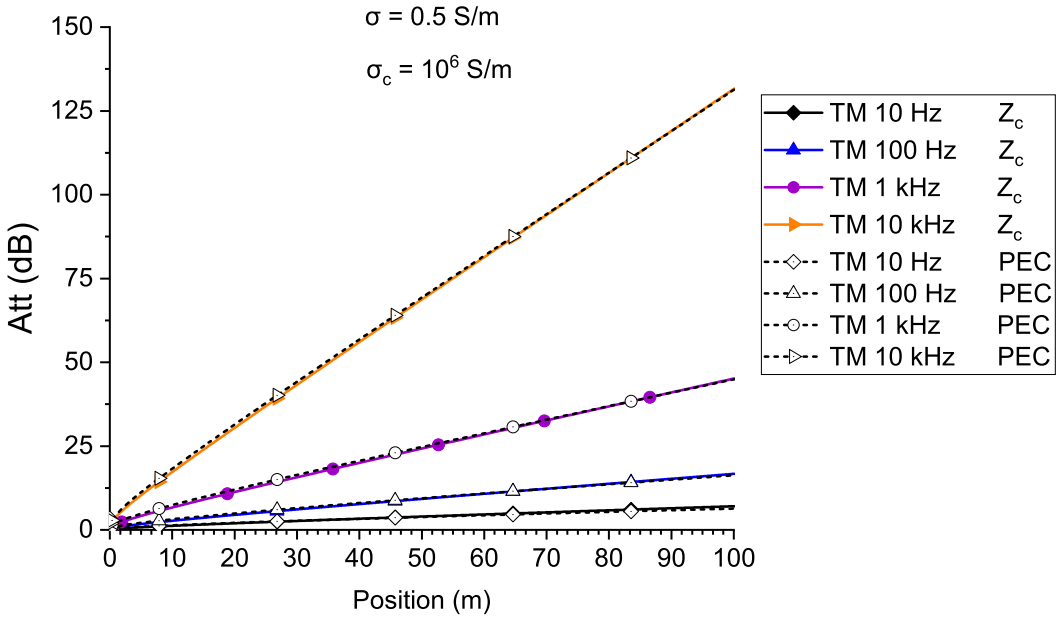

Figure 5.7: Attenuation experimented by the azimuthal component of the magnetic field H_ϕ in an isotropic formation with an embedded lossy metallic cylinder as a function of the frequency ($\sigma_c = 10^6$ S/m).

in the PEC case for the TE^z mode are approximately identical. However, due the lossy characteristic of the metallic cylinder, the attenuation experimented are smaller than those of the PEC scenario.

In contrast to Fig. 5.7, a reduction of the conductivity of the surrounding medium makes the attenuation for the TM^z varies slightly from the PEC

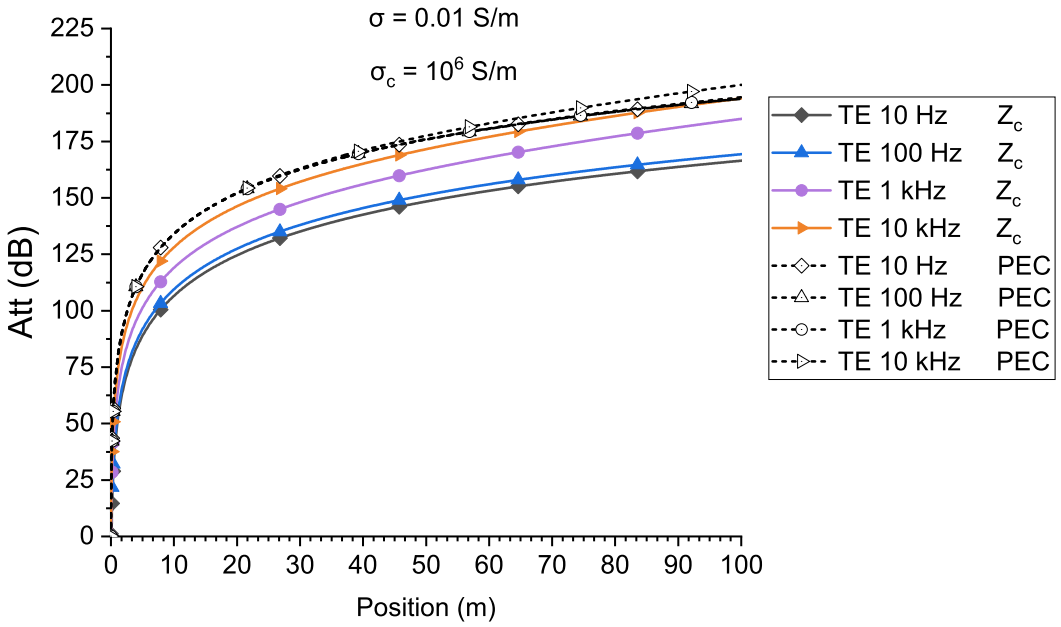

Figure 5.8: Attenuation experimented by the azimuthal component of the electric field E_ϕ in an isotropic formation with an embedded lossy metallic cylinder as a function of the frequency ($\sigma_c = 10^6$ S/m).

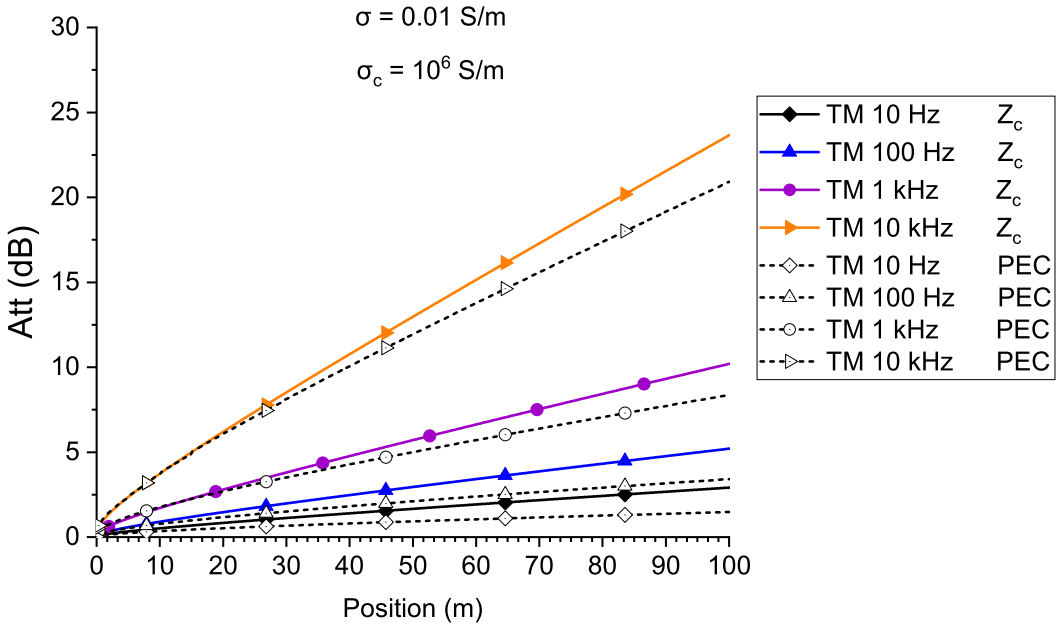

Figure 5.9: Attenuation experimented by the azimuthal component of the magnetic field H_ϕ in an isotropic formation with an embedded lossy metallic cylinder as a function of the frequency ($\sigma_c = 10^6$ S/m).

scenario, as in Fig. 5.9. It can be appreciated how for the TM^z mode, the scenario with the smaller attenuation is the one with a loss-less cylinder (PEC).

5.3.2
Homogeneous Biaxial Anisotropic Formation

The presented solution was also validated for anisotropic formations. Three cases were considered, determined by a permutation of the values in the conductivity tensor, which takes the values of:

$$\bar{\bar{\sigma}}_1 = \begin{bmatrix} 1 & 0 & 0 \\ 0 & 0.1 & 0 \\ 0 & 0 & 0.01 \end{bmatrix}, \; \bar{\bar{\sigma}}_2 = \begin{bmatrix} 0.1 & 0 & 0 \\ 0 & 0.01 & 0 \\ 0 & 0 & 1 \end{bmatrix}, \; \bar{\bar{\sigma}}_3 = \begin{bmatrix} 0.01 & 0 & 0 \\ 0 & 1 & 0 \\ 0 & 0 & 0.1 \end{bmatrix}. \quad (5\text{-}17)$$

The simulations were done for 1 kHz of frequency and the losses of the metallic cylinder was set by specifying $\sigma_c = 10^5$ S/m, which is a commonly value for representing finite conductivity [30]. In Fig. 5.10, Fig. 5.11 and Fig. 5.12, are presented the amplitude, phase and attenuation, respectively, of the azimuthal component of the electric (magnetic) field E_ϕ (magnetic H_ϕ) for the fist conductivity tensor of (5-17). Both solutions converge to the same results, which validates the accuracy of the proposed formulation.

For the second conductivity tensor in (5-17) the amplitude, phase and attenuation, respectively, of the azimuthal component of the electric (magnetic) field E_ϕ (magnetic H_ϕ) are shown in Fig. 5.13, Fig. 5.14 and Fig. 5.15.

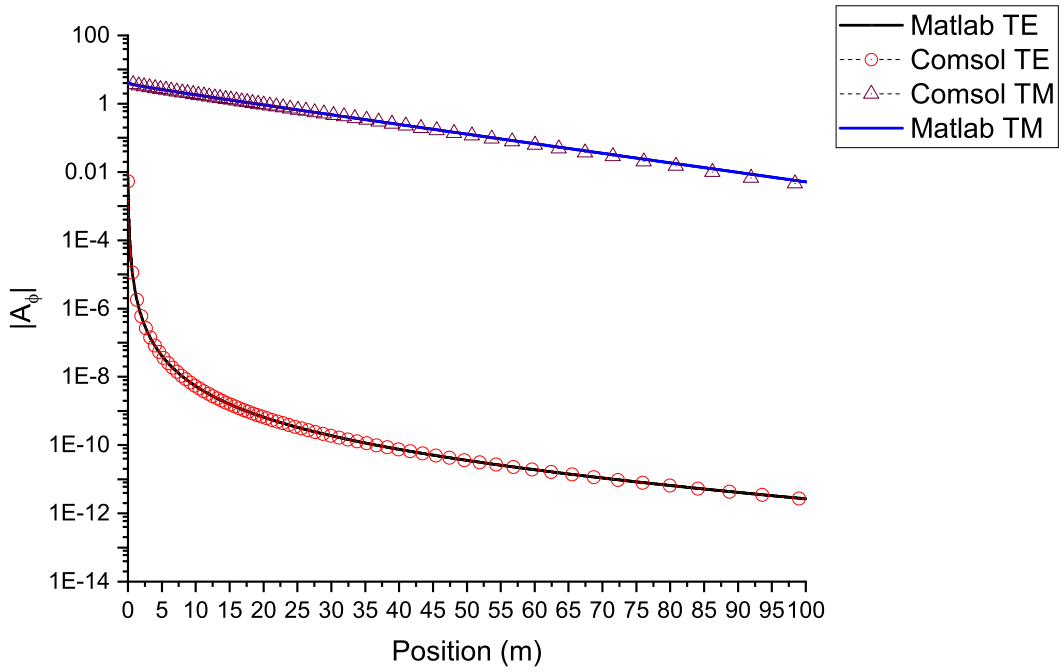

Figure 5.10: Absolute values of the azimuthal components of the electric (magnetic) field E_ϕ (H_ϕ) in an anisotropic formation ($\bar{\bar{\sigma}}_1$).

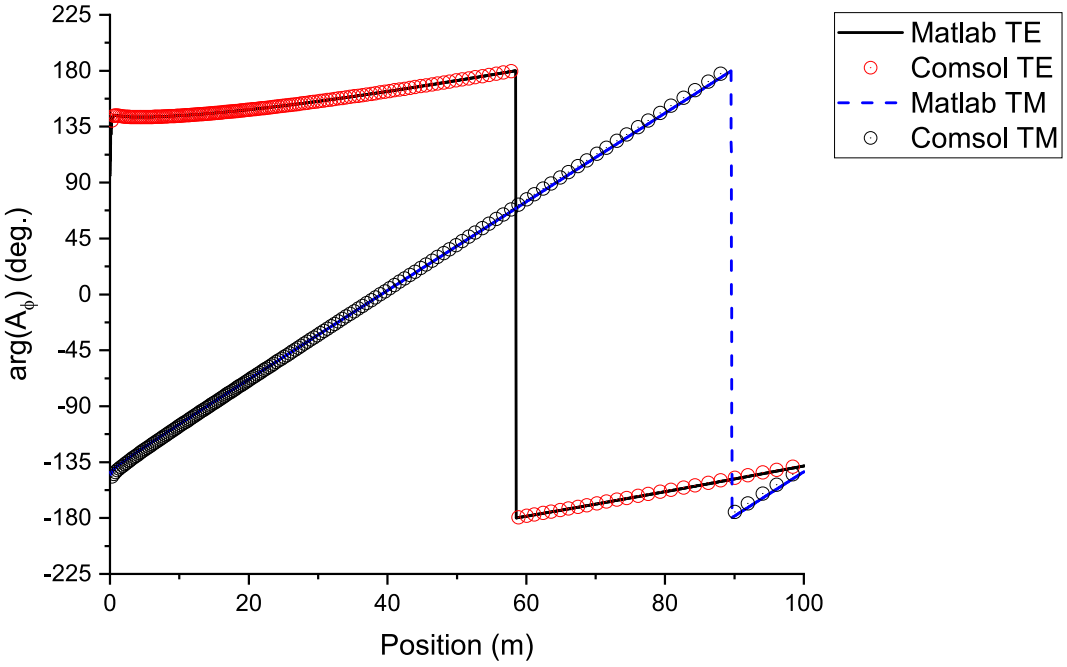

Figure 5.11: Phase values of the azimuthal components of the electric (magnetic) field E_ϕ (H_ϕ) in an anisotropic formation ($\bar{\bar{\sigma}}_1$).

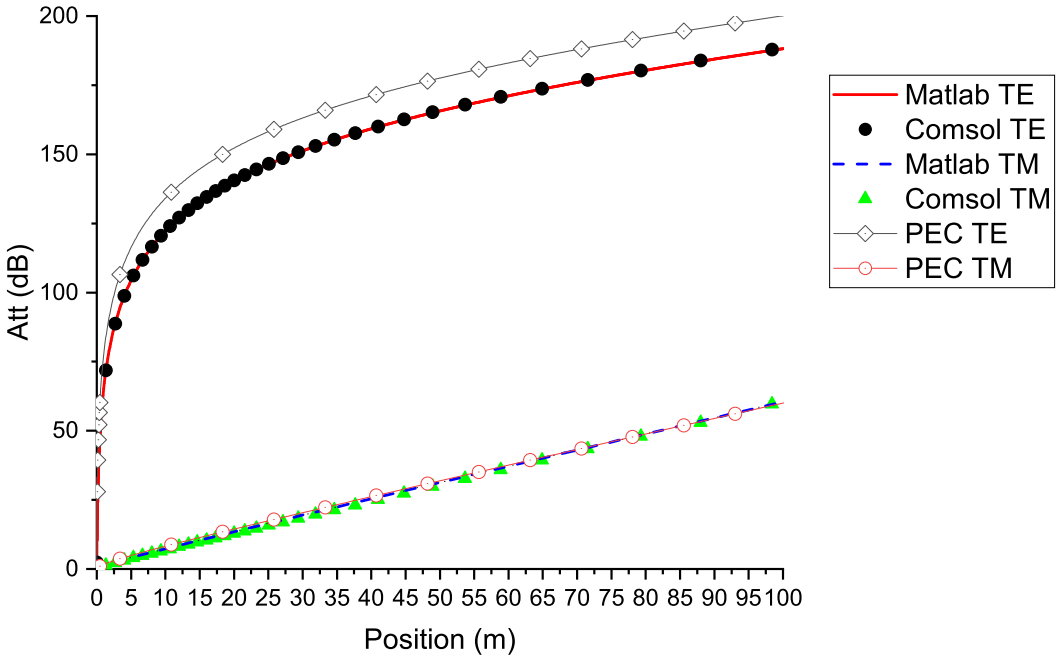

Figure 5.12: Attenuation experimented by the azimuthal components of the electric (magnetic) field E_ϕ (H_ϕ) in an anisotropic formation ($\bar{\bar{\sigma}}_1$). Comparison with the PEC solution.

Finally, the amplitude, phase and attenuation, respectively, of the azimuthal component of the electric (magnetic) field E_ϕ (magnetic H_ϕ) for the third conductivity tensor in (5-17) are presented in Fig. 5.16, Fig. 5.17 and Fig. 5.18.

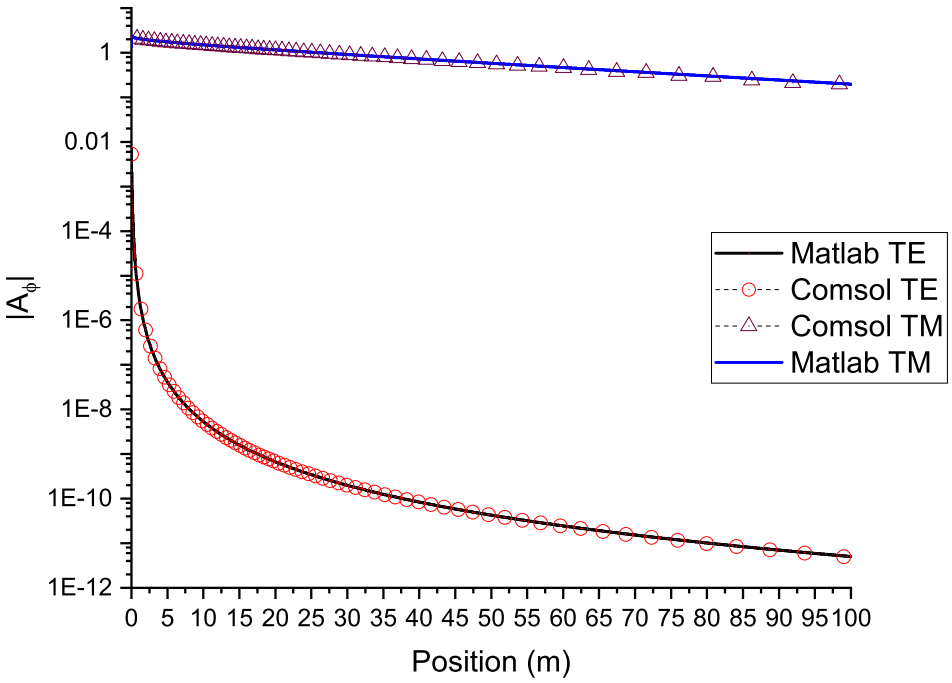

Figure 5.13: Absolute values of the azimuthal components of the electric (magnetic) field E_ϕ (H_ϕ) in an anisotropic formation (200 kHz) ($\bar{\bar{\sigma}}_2$).

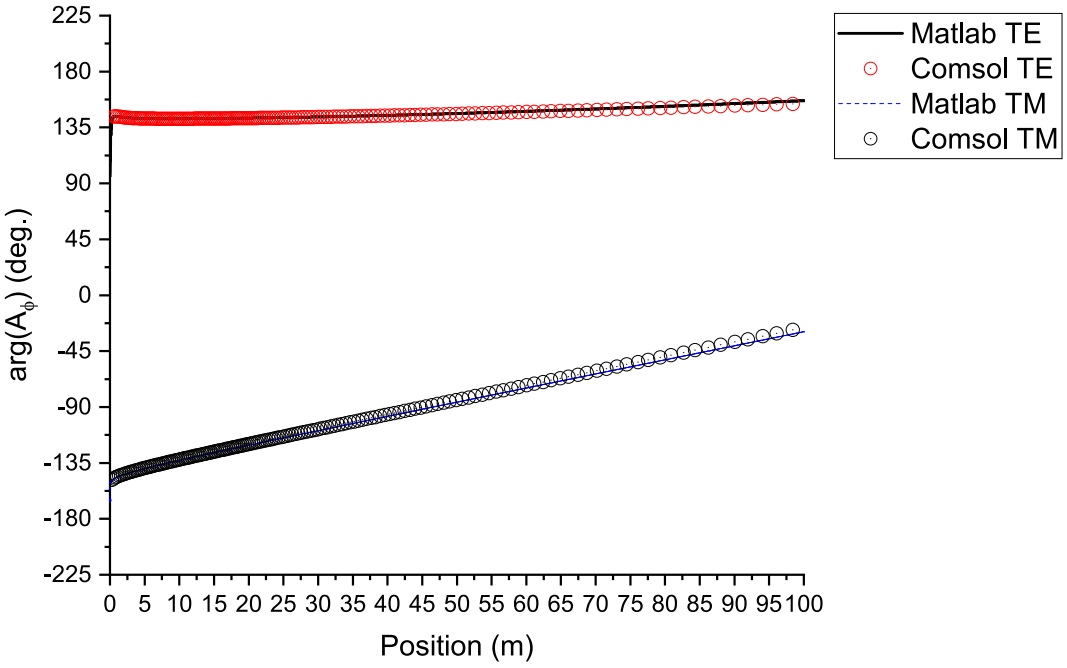

Figure 5.14: Phase values of the azimuthal components of the electric (magnetic) field E_ϕ (H_ϕ) in an anisotropic formation.

From all these results, it can be noticed that the TM^z field is almost not affected with the finite conductivity of the metallic cylinder. However, the TE^z field is lightly affected, and the higher the losses in the cylinder the better the propagation characteristics for this mode.

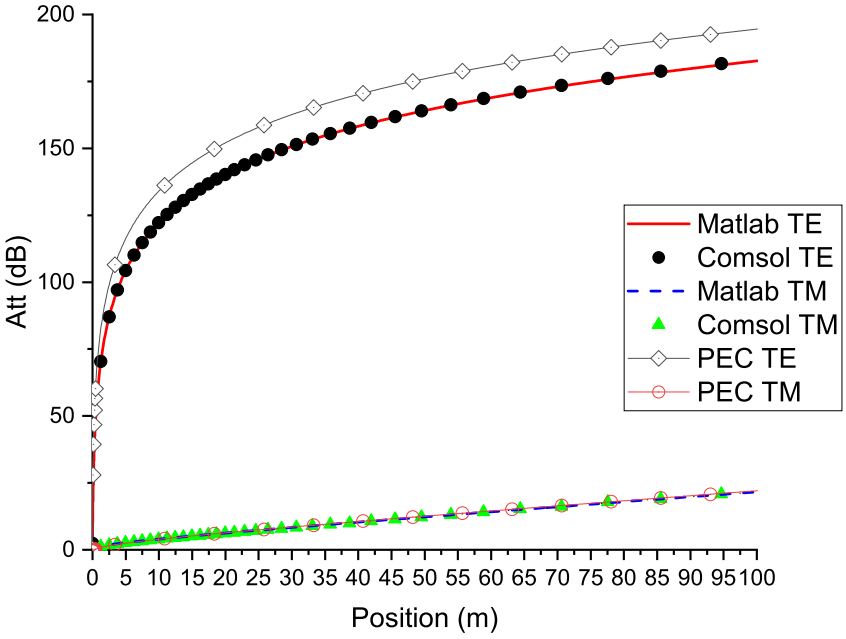

Figure 5.15: Attenuation experimented by the azimuthal components of the electric (magnetic) field E_ϕ (H_ϕ) in an anisotropic formation ($\bar{\bar{\sigma}}_2$). Comparison with the PEC solution.

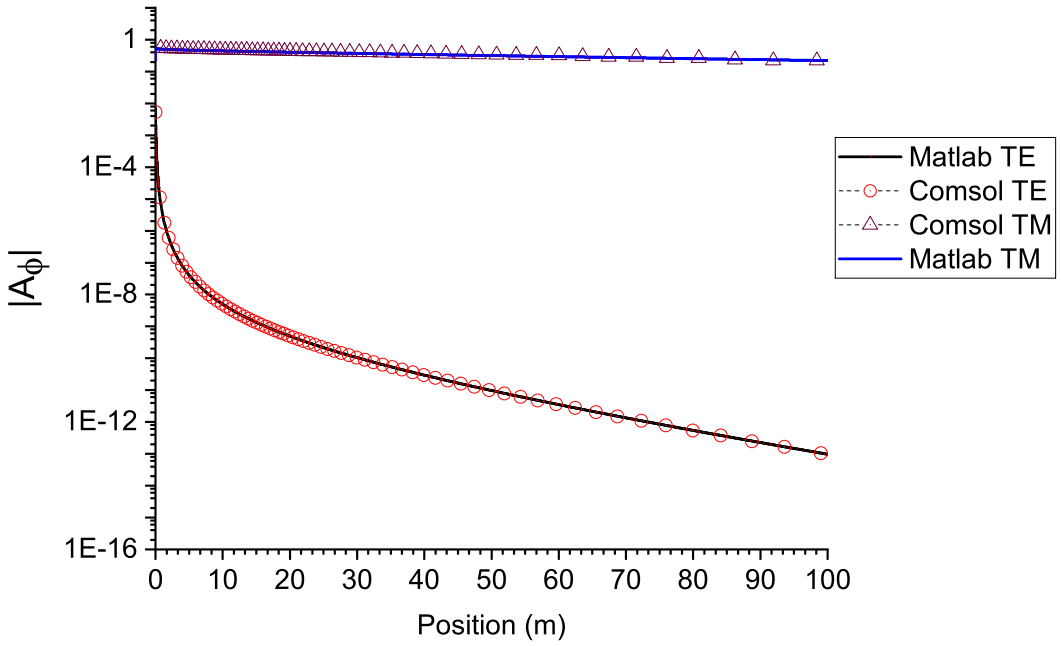

Figure 5.16: Absolute values of the azimuthal components of the electric (magnetic) field E_ϕ (H_ϕ) in an anisotropic formation ($\bar{\bar{\sigma}}_3$).

In Fig. 5.19 is presented a comparison between the previous curves and the isotropic scenario with conductivity value of 1 S/m. As it was presented in Fig. 3.20, the radial component of the conductivity with the highest value is the one that attenuate the most the propagation for the TM^z mode. On the other hand, for the TE^z mode the higher attenuation is experimented by the

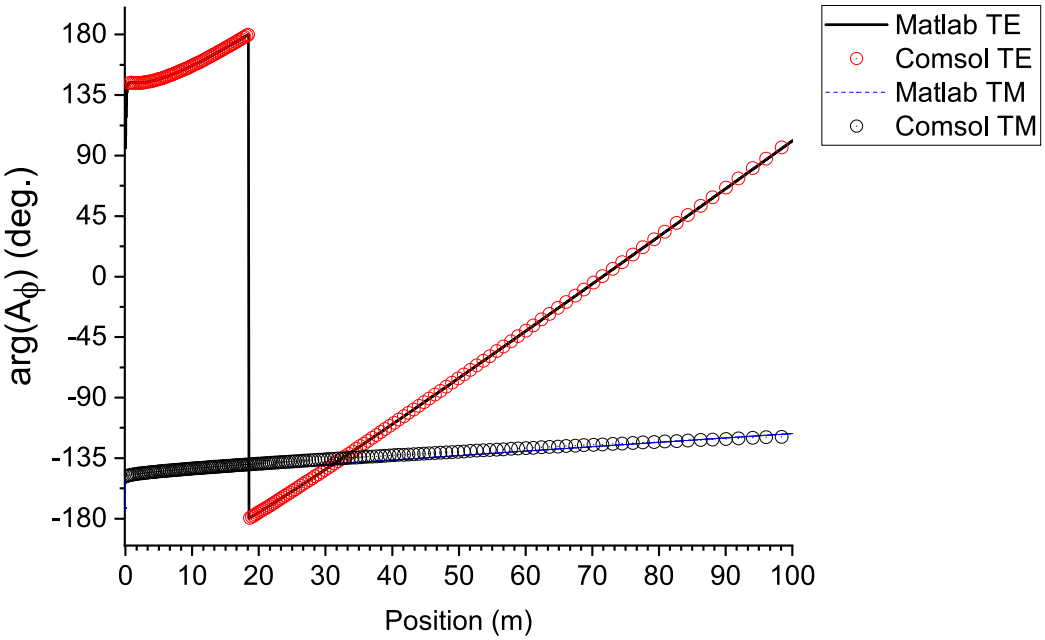

Figure 5.17: Phase values of the azimuthal components of the electric (magnetic) field E_ϕ (H_ϕ) in an anisotropic formation ($\bar{\bar{\sigma}}_3$).

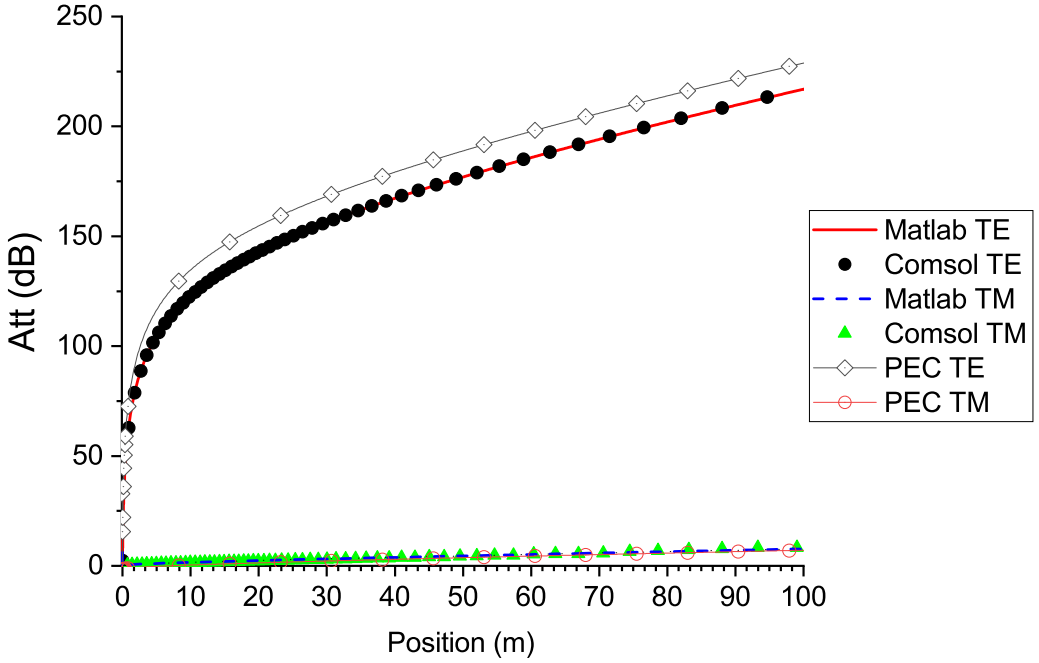

Figure 5.18: Attenuation experimented by the azimuthal components of the electric (magnetic) field E_ϕ (H_ϕ) in an anisotropic formation ($\bar{\bar{\sigma}}_3$). Comparison with the PEC solution.

scenario with the higher azimuthal value in the conductivity tensor.

It can be appreciated that for all the cases discussed, the implemented method lead to the same results that the finite-element solver. According to this, the developed semi-analytical solution can be used for modeling accurately the losses in the metallic cylinder as well.

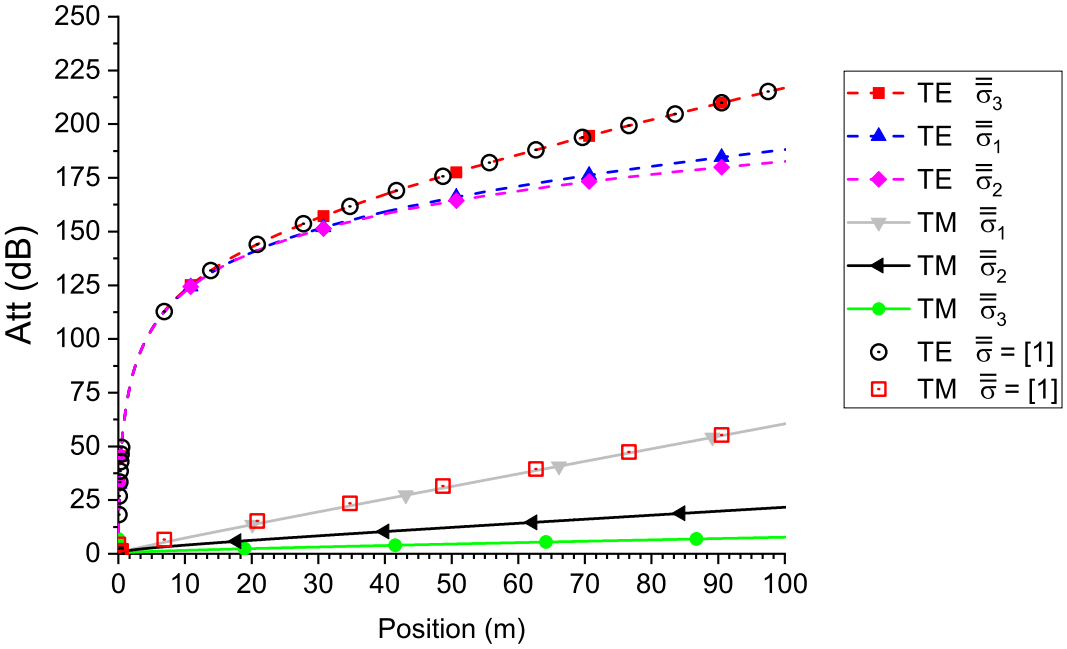

Figure 5.19: Attenuation experimented by the azimuthal components of the electric (magnetic) field E_ϕ (H_ϕ) in an anisotropic formation. Comparison with the isotropic case for $\bar{\bar{\sigma}} = [1]$.

5.4 Conclusions

In this chapter, the solution formulated in Chapter 3 is extended to support the lossy characteristics of real metallic structures. An impedance boundary condition was discussed and several tests were done in order to verify the efficiency of the proposed solution.

The results obtained with the metallic cylinder modeled by an impedance boundary condition showed an improvement for the propagation of TE^z waves, while for the TM^z it get slightly more attenuated when a high contrast between the conductivity of the mandrel and the surrounding medium exists. Despite of this, the TM^z showed again a more promising scenario for surface wave propagation in highly conductive media.

6
Conclusions and Suggestions for Future Research

Modern geophysical exploration demands fast and accurate solutions to simulate electromagnetic telemetry systems. Conventional simulation techniques require a great amount of computational cost to model complex geological formations, which difficult the analysis of wave propagation in those media.

In this dissertation an accurate electromagnetic propagation analysis for complex geophysical formations was performed via a novel spectral domain approach where a Hankel-based integral transform is introduced. This provides a modeling of well-logging tools without requiring expensive simulation solutions. The formulation achieved in Chapter 3 allows to solve Maxwell's equations in a biaxially anisotropic and azimuthal symmetric media excited by azimuthal symmetric sources.

The proposed formulation has been benchmarked against brute-force finite-element solvers, and demonstrate the ability of the technique for analyzing wave propagation in complex media via a numerically stable and robust semi-analytic algorithm. However, it is important to highlight that the solution proposed in this work requires just a fraction of the computational resources used by the FEM Comsol solver.

The model also considered the inclusion of a metallic cylinder in the downhole formation which had an important impact in the wave propagation, allowing surface waves to propagate near the metallic cylinder. Within this configuration, transversal magnetic waves presented a more promising scenario, while transversal electric waves were more attenuated when the metallic cylinder was present.

In Chapter 4, a formulation for the analysis of the electromagnetic field propagation along biaxially anisotropic and lossy horizontal stratified geometries was presented. The differences in the electromagnetic characteristics of these layers cause multiple reflections at the interfaces between them, and consequently, the attenuation experimented by the wave increases. The proposed solution has important applications for modeling and analyzing electromagnetic propagation through geophysical stratified scenarios analogous to those of the Brazilian Pre-Salt.

In Chapter 5, a more rigorous characterization of the metallic cylinder embedded in a biaxially anisotropic medium is presented by modeling its finite electrical conductive via an impedance boundary condition. Several tests were performed in order to verify the efficiency of the proposed solution. This scenario showed an improvement in the propagation characteristics for transversal electric waves while transversal magnetic waves experimented no several variation in highly conductive media. When the surrounding media became less lossy, transversal magnetic waves started to experiment more attenuation that with the ideal PEC modeling.

The presented study in this dissertation has important contributions for modeling downhole telemetry systems with applications for the Brazilian petroleum industry. As future work, it is suggested the extension of the proposed solution to model impedance boundary conditions in horizontal stratified media. This would require a more rigorous mathematical formulation to include the changing in the axial propagation function (as a consequence of the stratifications and multiple reflection) and also a modification in the radial function (due the surface impedance modeling).

Bibliography

[1] ODDONE, D.. **The Oil and Gas Industry in Brazil.** `http://www.anp.gov.br/palestra/`, June 2018.

[2] PETERSOHN, E.. **Brazil's Petroleum Unleashed: Recent Changes and Future Potential.** `http://www.anp.gov.br/palestra/`, Nov. 2018.

[3] LIU, C. R.. **Theory of Electromagnetic Well Logging**. Elsevier, 1st edition, 2017.

[4] ROSA, G. S.; BERGMANN, J. R. ; TEIXEIRA, F. L.. **Mode-matching modeling of low-frequency wireless telemetry in deep oil fields**. In: 2017 11TH EUROPEAN CONFERENCE ON ANTENNAS AND PROPAGATION (EUCAP), p. 1228–1232, Mar. 2017.

[5] SAFINYA, K.; MCBRIDE, R.. **System and method for communicating signals in a cased borehole having tubing**, 1988. European Patent EP0295178A2.

[6] MWACHAKA, S. M.; WU, A. ; FU, Q.. **A review of mud pulse telemetry signal impairments modeling and suppression methods**. Journal of Petroleum Exploration and Production Technology, 9(1):779–792, Mar. 2019.

[7] SAAVEDRA, L.; ROSA, G. S. ; BERGMANN, J. R.. **An accurate technique for modeling realistic well-logging sensors inside complex media**. In: 2019 INTERNATIONAL APPLIED COMPUTATIONAL ELECTROMAGNETICS SOCIETY SYMPOSIUM (ACES), p. 1–2, Apr. 2019.

[8] HUE, Y.-K.. **Analysis of Electromagnetic Well-Logging Tools**. PhD thesis, The Ohio State University, 2006.

[9] BOYER, S.; MARI, J.-L.. **Seismic Surveying And Well Logging: Oil And Gas Exploration Techniques**. Editions Technip, 1st edition, 1997.

[10] JORDEN, J. R.; CAMPBELL, F. L.. **Well Logging II-Electric and Acoustic-SPE Series**. Society of Petroleum Engineers, 1986.

[11] CHESTER LAO, FRANK L. PETERSON, D. C. C.. **Application of electric well logging and other well logging methods in hawaii**. Technical report no. 21, 1969.

[12] GONG, B.. **Study of Downhole Electromagnetic BoundaryDetection Methods Using Numerical Simulations**. PhD thesis, University of Houston, 2014.

[13] DA ROSA, G. S.. **Pseudo-Analytical Modeling for Electromagnetic Well-Logging Tools in Complex Geophysical Formations**. PhD thesis, Pontifical Catholic University of Rio de Janeiro, 2017.

[14] C. CHIN, W.. **Electromagnetic Well Logging: Models for MWD/LWD Interpretation and Tool Design**. J.Wiley and Sons, Inc., 2014.

[15] TIANSHOU, M.; CHEN, P. ; ZHAO, J.. **Overview on vertical and directional drilling technologies for the exploration and exploitation of deep petroleum resources**. Geomechanics and Geophysics for Geo-Energy and Geo-Resources, 2:1–31, Aug. 2016.

[16] WRIGHT, C. J.; GALLUN, R. A.. **Fundamentals of Oil and Gas Accounting**. PennWell Corporation, 5th edition, 2008.

[17] CARRENO, J. D. P.. **Channel modeling for through-the-earth (tte) communication systems**. Master's thesis, University of Brasília, 2016.

[18] RALCHENKO, M.; SVILANS, M.; SAMSON, C.; WALSH, C. ; ROPER, M.. **Optimization of through-the-earth radio communications via mine overburden conductivity estimation**. Mining Engineering, 70:113–120, July 2018.

[19] SHAYDUROV, G. Y.; KUDINOV, D. S.; KOKHONKOVA, E. A. ; SHCHITNIKOV, A. A.. **Through-the-earth communication in underground mines by electromagnetic waves**. In: 2016 INTERNATIONAL SIBERIAN CONFERENCE ON CONTROL AND COMMUNICATIONS (SIBCON), p. 1–6, 2016.

[20] CARREÑO, J.; SILVA, L.; NEVES, S.; AGUAYO, L.; JUDSON BRAGA, A.; BARRETO, A. N. ; UZEDA GARCIA, L. G.. **Through-the-earth (tte) communications for underground mines**. Journal of Communication and Information Systems, 31:164–176, July 2016.

[21] JIANNAN SUN; YANHUI TIAN; WEIZHI GENG ; WEI XUE. **Design of wireless communication system based on conduction current field through the earth**. In: 10TH INTERNATIONAL CONFERENCE ON WIRELESS COMMUNICATIONS, NETWORKING AND MOBILE COMPUTING (WICOM 2014), 2014.

[22] FOROOSHANI, A. E.; BASHIR, S.; MICHELSON, D. G. ; NOGHANIAN, S.. **A survey of wireless communications and propagation modeling in underground mines**. IEEE Communications Surveys Tutorials, 15(4):1524–1545, 2013.

[23] WAIT, J. R.. **Response of a point source embedded in a layered medium**. Journal of Research of the National Bureau of Standards, 61(3), 1958.

[24] JAMES R. WAIT, A. L. CULLEN, V. A. F.; (AUTH.), J. R. W.. **Electromagnetic Waves in Stratified Media. Including Supplemented Material**. Pergamon Press, 2nd edition, 1970.

[25] WAIT, J. R.; HILL, D. A.. **Theory of transmission of electromagnetic waves along a drill rod in conducting rock**. IEEE Transactions on Geoscience Electronics, 17(2):21–24, Apr. 1979.

[26] TITCHENER, J. B.; WILLIS, J. R.. **The reflection of electromagnetic waves from stratified anisotropic media**. IEEE Transactions on Antennas and Propagation, 39(1):35–39, 1991.

[27] LØSETH, L.; URSIN, B.. **Electromagnetic fields in planarly layered anisotropic media**. Geophysical Journal International - GEOPHYS J INT, 170:44–80, July 2007.

[28] R. DINAPOLI, F.; DEAVENPORT, R.. **Theoretical and numerical green's function field solution in a plane multilayered medium**. The Journal of the Acoustical Society of America, 67:92–105, Jan. 1980.

[29] CHEW, W. C.; CHEN, S.-Y.. **Response of a point source embedded in a layered medium**. IEEE Antennas and Wireless Propagation Letters, 2, 2003.

[30] ZENG, S.; LI, D.; R. WILTON, D. ; CHEN, J.. **Fast and accurate simulation of electromagnetic telemetry in deviated and horizontal drilling**. Journal of Petroleum Science and Engineering, 166, Mar. 2018.

[31] SOMMERFELD, A.. **Partial Differential Equations in Physics**, volumen 1. Elsevier Science, 1949.

[32] CHEW, W. C.; BARONE, S.; ANDERSON, B. ; HENNESSY, C.. **Diffraction of axisymmetric waves in a borehole by bed boundary discontinuities**. GEOPHYSICS, 49(10):1586–1595, 1984.

[33] CHEW, W. C.; ANDERSON, B.. **Propagation of electromagnetic waves through geological beds in a geophysical probing environment**. Radio Science, 20(3):611–621, May 1985.

[34] CHEW, W. C.. **Waves and Fields in Inhomogenous Media**. Wiley-IEEE Press, 1995.

[35] WAIT, J.; SPIES, K.. **Subsurface electromagnetic fields of a circular loop of current located above ground**. IEEE Transactions on Antennas and Propagation, 20(4):520–522, 1972.

[36] A. KONG, J.. **Electromagnetic field due to dipole antennas over stratified anisotropic media**. Geophysics, 37, Jan. 1973.

[37] SAINATH, K.; TEIXEIRA, F. ; DONDERICI, B.. **Robust computation of dipole electromagnetic fields in arbitrarily anisotropic, planar-stratified environments**. Physical review. E, Statistical, nonlinear, and soft matter physics, 89:013312, Jan. 2014.

[38] ROSA, G. S.; CANABARRO, M. S.; BERGMANN, J. R. ; TEIXEIRA, F. L.. **A comparison of numerical mode-matching techniques for the analysis of well-logging tools**. In: 2017 INTERNATIONAL APPLIED COMPUTATIONAL ELECTROMAGNETICS SOCIETY SYMPOSIUM - ITALY (ACES), p. 1–2, Jan. 2017.

[39] GUEGUEN, Y.; PALCIAUSKAS, V.. **Introduction to Physics of Rocks**. Princeton University Press, 1st edition, 1994.

[40] MCNEILL, J. D.. **Electrical conductivity of soils and rocks**. Technical note (geonics limited); tn-5., 1980.

[41] K. F. RILEY, M. P. HOBSON, S. J. B.. **Mathematical Methods for Physics and Engineering: A Comprehensive Guide**. Cambridge University Press, 3rd edition, 2006.

[42] GARG, R.. **Analytical and Computational Methods in Electromagnetics**. Artech House Publishers, 1st edition, 2008.

[43] EOM, H. J.. **Electromagnetic wave theory for boundary-value problems: an advanced course on analytical methods**. Springer, 1st edition, 2004.

[44] **Comsol multiphysics**. `http://www.comsol.com`. Accessed: 2019-04-07.

[45] **Ansys hfss—high frequency electromagnetic field simulation**. `http://www.ansys.com/Products/Electronics/ANSYS-HFSS`. Accessed: 2019-04-07.

[46] **Ansys maxwell—low frequency electromagnetic field simulation**. `http://www.ansys.com/Products/Electronics/ANSYS-Maxwell`. Accessed: 2019-04-07.

[47] BALANIS, C. A.. **Antenna Theory Analysis and Design**. J.Wiley and Sons, Inc., 4th edition, 2016.

[48] HARRINGTON, R. F.. **Time-Harmonic Electromagnetic Fields**. Wiley-IEEE Press, 2001.

[49] BALANIS, C. A.. **Advance Engineering Electromagnetics**. J.Wiley and Sons, Inc., 2nd edition, 2012.

[50] PONCE DE LEON, J.. **Revisiting the orthogonality of bessel functions of the first kind on an infinite interval**. European Journal of Physics, 36, Jan. 2015.

[51] MILOVANOVIC, G.; RASSIAS, M.. **Analytic Number Theory, Approximation Theory, and Special Functions: In Honor of Hari M. Srivastava**. Analytic Number Theory, Approximation Theory, and Special Functions: In Honor of Hari M. Srivastava. Springer New York, 2014.

[52] AMJADI, S. M.; SARABANDI, K.. **A compact single conductor transmission line launcher for telemetry in borehole drilling**. IEEE Transactions on Geoscience and Remote Sensing, PP:1–8, Jan. 2017.

[53] GATTI, M.; LIN, H.; LONG, E.; SOSNOWSKI, J. ; JAMNEJAD, V.. **A test-bed validation of electromagnetic surface wave propagation along a dielectric-coated metal pipe**. In: 2016 IEEE AEROSPACE CONFERENCE, p. 1–13, Mar. 2016.

[54] KOTELNIKOV, I.; V. STUPAKOV, G.. **Electromagnetic surface waves on a conducting cylinder**. Physics Letters A, 379, June 2015.

[55] SIEVENPIPER, D.; ZHANG, L.; BROAS, R. F. J. ; NICHOLAS G. ALEXOPOLUS, E. Y.. **High-impedance electromagnetic surfaces forbidden frequency band**. IEEE Transactions n Microwave THeory and Techniques, 47(11), 1999.

[56] JR., J. A. P.; MACKAY, T. G. ; LAKHTAKIA, A.. **Electromagnetic Surfaces Waves: a modern perspective**. Elsevier Science, 1st edition, 2013.

[57] L. OVERFELT, P.. **Review of electromagnetic surface waves, 1960 through 1987**. Final Report, Aug. 1987 - Oct. 1987 Naval Weapons Center, China Lake, CA., Jan. 1988.

[58] SERGEY V. YUFEREV, N. I.. **Surface Impedance Boundary Conditions. A comprehensive Approach**. CRC Press. Taylor and Francis Group, 2010.

[59] SMITH, G. S.. **On the skin effect approximation**. American Journal of Physics, 58(10), 1990.

[60] LEONTOVICH, M.. **On the approximate boundary conditions for the electromagnetic field on the surface of well conducting bodies**. Investigations on Propagation of Radio Waves, 1948.

[61] ABRAMOWITZ, M.; STEGUN, I. A.. **Handbook of Mathematical Functions: With Formulas, Graphs, and Mathematical Tables**. Dover Publications, New York, NY, USA, 1964.

[62] **NIST Digital Library of Mathematical Functions**. `http://dlmf.nist.gov/`. F. W. J. Olver, A. B. Olde Daalhuis, D. W. Lozier, B. I. Schneider, R. F. Boisvert, C. W. Clark, B. R. Miller and B. V. Saunders, eds.

A
Notes on the Orthogonality of Cylindrical Functions Over an Infinity Domain

Consider the integral

$$I = \int_0^\infty d\rho\, \rho\, B_n(k_\rho\, \rho)\, B_n(k'_\rho\, \rho), \tag{A-1}$$

where $B_n(k_\rho\, \rho)$ is a solution (or a linear combination of solutions) for the Bessel differential equation of order n. The above can be solved with the aid of

$$I = \lim_{b\to\infty} I_b, \tag{A-2}$$

where

$$I_b = \int_0^b d\rho\, \rho\, B_n(k_\rho\, \rho)\, B_n(k'_\rho\, \rho). \tag{A-3}$$

If there eigenvalues $\kappa = \{k_\rho, k'_\rho\}$ for $B_n(\kappa\, \rho)$ over the domain $0 \leq \rho < b$, I_b is supported by the closed form solution when n is integer [61, pp. 484–485], namely,

$$I_b = \frac{1}{k_\rho^2 - k_\rho'^2} \left[k'_\rho\, b\, B_n(k_\rho\, b) B_{n-1}(k'_\rho\, b) - k_\rho\, b\, B_n(k'_\rho\, b) B_{n-1}(k_\rho\, b)\right]. \tag{A-4}$$

Before to employ $(\text{A-}4)$, first it is necessary to define a generic function for $B_n(\cdot)$ and its behavior should also evaluated when $b \gg 1$ in order to use that as basis for solving $(\text{A-}2)$. By choosing such function as a linear combination of Bessel functions of first and second kind, it can be written as

$$B_n(x) = A_n\, J_n(x) + B_n\, Y_n(x), \tag{A-5}$$

where A_n and B_n are (in general complex) constants in ρ, but they can be functions of n. In order to simplify the notation, the subscript n in such constants will be temporarily dropped, restoring it later as needed. For $b \gg 1$, it can be obtained from [61, Eqs. 9.2.5 and 9.2.6]

$$J_n(k_\rho\, b) \underset{b\gg 1}{\longrightarrow} \sqrt{\frac{2}{\pi\, k_\rho\, b}}\, \cos\left(k_\rho\, b - \frac{n\pi}{2} - \frac{\pi}{4}\right), \tag{A-6}$$

$$Y_n(k_\rho\, b) \underset{b\gg 1}{\longrightarrow} \sqrt{\frac{2}{\pi\, k_\rho\, b}}\, \sin\left(k_\rho\, b - \frac{n\pi}{2} - \frac{\pi}{4}\right). \tag{A-7}$$

Then, an evaluation of $(\text{A-}4)$ for large b by using $(\text{A-}6)$ and $(\text{A-}7)$ will be

done. First, lets consider the product below when $b \gg 1$:

$$B_n(k_\rho\, b)\, B_{n-1}(k'_\rho\, b) = \sqrt{\frac{2}{\pi\, k_\rho\, b}}\left[A\,\cos\left(k_\rho\, b - \frac{n\pi}{2} - \frac{\pi}{4}\right) + B\,\sin\left(k_\rho\, b - \frac{n\pi}{2} - \frac{\pi}{4}\right)\right] \times \sqrt{\frac{2}{\pi\, k'_\rho\, b}}\left[A\,\cos\left(k'_\rho\, b - \frac{(n-1)\pi}{2} - \frac{\pi}{4}\right) + B\,\sin\left(k'_\rho\, b - \frac{(n-1)\pi}{2} - \frac{\pi}{4}\right)\right]. \tag{A-8}$$

By introducing $\tilde{n} = n\pi/2 + \pi/4$ and after some simplifications, the above reduces to

$$B_n(k_\rho\, b)\, B_{n-1}(k'_\rho\, b) = \frac{2}{\pi\, b}\frac{1}{\sqrt{k_\rho}\sqrt{k'_\rho}}\Big[-A^2\,\cos(k_\rho\, b - \tilde{n})\,\sin(k'_\rho\, b - \tilde{n}) + A\,B\,\cos(k_\rho\, b - \tilde{n})\,\cos(k'_\rho\, b - \tilde{n}) - B\,A\,\sin(k_\rho\, b - \tilde{n})\,\sin(k'_\rho\, b - \tilde{n}) + B^2\,\sin(k_\rho\, b - \tilde{n})\,\cos(k'_\rho\, b - \tilde{n})\Big]. \tag{A-9}$$

Again, in order to further simplify the notation, it will be introduced

$$C = \cos(k_\rho\, b - \tilde{n}), \tag{A-10}$$

$$C' = \cos(k'_\rho\, b - \tilde{n}), \tag{A-11}$$

$$S = \sin(k_\rho\, b - \tilde{n}), \tag{A-12}$$

$$S' = \sin(k'_\rho\, b - \tilde{n}). \tag{A-13}$$

Equation (A-9) now becomes

$$B_n(k_\rho\, b)\, B_{n-1}(k'_\rho\, b) = \frac{2}{\pi\, b}\frac{1}{\sqrt{k_\rho}\sqrt{k'_\rho}}\left[-A^2\,C\,S' + A\,B\,C\,C' - B\,A\,S\,S' + B^2\,S\,C'\right]. \tag{A-14}$$

The above results can be used to simplify the second term in (A-4), namely, $B_n(k'_\rho\, b)\, B_{n-1}(k_\rho\, b)$, by means of the duality $T \rightarrow T'$ and $T' \rightarrow T$ with $T = \{C, S\}$.

By collecting the partial results above, it can now write a solution for (A-4) when $b \gg 1$:

$$I_b = \frac{1}{k_\rho^2 - k_\rho'^2}\left[\frac{2\,k'_\rho}{\pi\,\sqrt{k'_\rho}\,\sqrt{k_\rho}}\left(-A^2\,C\,S' + A\,B\,C\,C' - B\,A\,S\,S' + B^2\,S\,C'\right) - \frac{2\,k_\rho}{\pi\,\sqrt{k_\rho}\,\sqrt{k'_\rho}}\left(-A^2\,C'\,S + A\,B\,C'\,C - B\,A\,S'\,S + B^2\,S'\,C\right)\right], \tag{A-15}$$

or, in a more compact form:

$$I_b = \frac{2}{\pi}\,\frac{1}{k_\rho^2 - k_\rho'^2}\,\frac{1}{\sqrt{k_\rho'}\,\sqrt{k_\rho}}\,\left[k_\rho'\,G_1 - k_\rho\,G_2\right], \tag{A-16}$$

where

$$G_1 = -A^2\,C\,S' + A\,B\,C\,C' - B\,A\,S\,S' + B^2\,S\,C', \tag{A-17}$$

and where G_2 is given by means of the duality $T \rightarrow T'$ and $T' \rightarrow T$ with $T = \{C, S\}$.

Before evaluate the limit when $b \rightarrow \infty$ in (A-2), first $G_{1,2}$ need to be carefully simplified by using the trigonometric identities

$$C\,S' = \frac{1}{2}\,\left[\sin(\kappa + \kappa') - \sin(\kappa - \kappa')\right], \tag{A-18}$$

$$C\,C' = \frac{1}{2}\,\left[\cos(\kappa + \kappa') + \cos(\kappa - \kappa')\right], \tag{A-19}$$

$$S\,S' = \frac{1}{2}\,\left[\cos(\kappa + \kappa') - \cos(\kappa - \kappa')\right], \tag{A-20}$$

where $\kappa = k_\rho\,b - \tilde{n}$ and $\kappa' = k_\rho'\,b - \tilde{n}$. As a result, after some simplifications, it is obtained

$$G_1 = -\frac{1}{2}\,(A^2 - B^2)\,\sin(\kappa + \kappa') + \frac{1}{2}\,(A^2 + B^2)\,\sin(\kappa - \kappa') + AB\,\cos(\kappa + \kappa'), \tag{A-21}$$

$$G_2 = -\frac{1}{2}\,(A^2 - B^2)\,\sin(\kappa + \kappa') - \frac{1}{2}\,(A^2 + B^2)\,\sin(\kappa - \kappa') + AB\,\cos(\kappa + \kappa'). \tag{A-22}$$

Now, when placing the simplified forms of G_1 and G_2 back into (A-16), results in

$$\begin{aligned} I_b = {} & \frac{1}{\pi}\,\frac{1}{k_\rho^2 - k_\rho'^2}\,\frac{1}{\sqrt{k_\rho'}\,\sqrt{k_\rho}} \\ & \times \Big\{k_\rho'\left[(-A^2 + B^2)\,\sin(\kappa + \kappa') + (A^2 + B^2)\,\sin(\kappa - \kappa') + 2A\,B\,\cos(\kappa + \kappa')\right] \\ & -k_\rho\left[(-A^2 + B^2)\,\sin(\kappa + \kappa') - (A^2 + B^2)\,\sin(\kappa - \kappa') + 2A\,B\,\cos(\kappa + \kappa')\right]\Big\}. \end{aligned} \tag{A-23}$$

Reordering the terms inside $\{\cdot\}$ such that the three kind of trigonometric dependences becomes evident, i.e.,

$$\begin{aligned} I_b = {} & \frac{1}{\pi}\,\frac{1}{(k_\rho - k_\rho')(k_\rho + k_\rho')}\,\frac{1}{\sqrt{k_\rho'}\,\sqrt{k_\rho}}\Big\{(-A^2 + B^2)\,(k_\rho' - k_\rho)\,\sin(\kappa + \kappa') \\ & + (A^2 + B^2)\,(k_\rho' + k_\rho)\,\sin(\kappa - \kappa') + 2A\,B\,(k_\rho' - k_\rho)\,\cos(\kappa + \kappa')\Big\}. \end{aligned} \tag{A-24}$$

The above can be further simplified to

$$I_b = \frac{1}{\pi}\frac{1}{\sqrt{k'_\rho}\sqrt{k_\rho}}\left\{-\frac{(-A^2+B^2)}{k_\rho+k'_\rho}\sin(\kappa+\kappa') + \frac{(A^2+B^2)}{k_\rho-k'_\rho}\sin(\kappa-\kappa') - \frac{2A\,B}{k_\rho+k'_\rho}\cos(\kappa+\kappa')\right\}. \quad \text{(A-25)}$$

Before proceed,lets recover the initial k_ρ and k'_ρ dependences into κ and κ' by using

$$\kappa+\kappa' = (k_\rho+k'_\rho)\,b - n\pi - \pi/2, \quad \text{(A-26)}$$

$$\kappa-\kappa' = (k_\rho-k'_\rho)\,b, \quad \text{(A-27)}$$

that allows us to rewrite $(\text{A-}25)$ as

$$I_b = \frac{1}{\sqrt{k'_\rho}\sqrt{k_\rho}}\left\{(-A^2+B^2)\frac{\cos[(k_\rho+k'_\rho)\,b-n\pi]}{\pi\,(k_\rho+k'_\rho)} + (A^2+B^2)\frac{\sin[(k_\rho-k'_\rho)\,b]}{\pi\,(k_\rho-k'_\rho)} - 2A\,B\,\frac{\sin[(k_\rho+k'_\rho)\,b-n\pi]}{\pi\,(k_\rho+k'_\rho)}\right\}, \quad \text{(A-28)}$$

where it has been used the trigonometric identities $\sin(x-\pi/2) = -\cos(x)$ and $\cos(x-\pi/2) = \sin(x)$. Finally, it will be taken the limit of $b\to\infty$ in $(\text{A-}28)$ in order to solve I, cf. $(\text{A-}2)$. This will be done by analyzing three cases:

(a) $k_\rho \neq \pm k'_\rho$,

(b) $k_\rho = +k'_\rho$,

(c) $k_\rho = -k'_\rho$.

The scenario (a) represents an orthogonality condition,and there is no contribution as $b\to\infty$. Cases (b) and (c) can be seen as an consequence of the symmetry of the cylinder functions of integer orders. As $b\to\infty$, the contribution of the cosine term in $(\text{A-}28)$ vanish, whereas the sine terms become nonzero only for $k_\rho = \pm k'_\rho$. For positive defined (with respect to the imaginary part) spectral eigenvalues, only case (b) is of interest. Then, it can obtained

$$I_b = \frac{A^2+B^2}{\sqrt{k'_\rho}\sqrt{k_\rho}}\,\delta_b[(k_\rho-k'_\rho)b], \quad \text{(A-29)}$$

where the delta-like function in the form

$$\delta_b(x) = \frac{\sin(x\,b)}{\pi x}. \quad \text{(A-30)}$$

It is well know that $\delta_b(x)$ becomes an ordinary Dirac delta for $b \to \infty$, i.e.,

$$\lim_{b\to\infty} \delta_b(x) = \delta(x). \tag{A-31}$$

By using $(\text{A-}29)$ into $(\text{A-}2)$, we obtain

$$I = \frac{A^2 + B^2}{\sqrt{k'_\rho}\,\sqrt{k_\rho}}\,\delta(k_\rho - k'_\rho). \tag{A-32}$$

If it is integrated the above over k_ρ, it is obtained

$$\int_0^\infty dk_\rho \int_0^\infty d\rho\,\rho\,B_n(k_\rho\,\rho)\,B_n(k'_\rho\,\rho) = \frac{A^2 + B^2}{k'_\rho}. \tag{A-33}$$

An orthonormality function can be derived based on $B_n(\cdot)$ in the form

$$\hat{B}_n(k_\rho\,\rho) = \sqrt{\frac{1}{A^2 + B^2}}\,\left[A\,J_n(k_\rho\,\rho) + B\,Y_n(k_\rho\,\rho)\right]. \tag{A-34}$$

As a consequence, it can be written

$$\delta(k_\rho - k'_\rho) = k'_\rho \int_0^\infty d\rho\,\rho\,\hat{B}_n(k_\rho\,\rho)\,\hat{B}_n(k'_\rho\,\rho) \tag{A-35}$$

and

$$\delta(\rho - \rho') = \rho' \int_0^\infty dk_\rho\,k_\rho\,\hat{B}_n(k_\rho\,\rho)\,\hat{B}_n(k_\rho\,\rho'). \tag{A-36}$$

In general,

$$\delta(x - a) = x \int_0^\infty dt\,t\,\hat{B}_n(x\,t)\,\hat{B}_n(a\,t). \tag{A-37}$$

Notice that when $B_n(\cdot) = J_n(\cdot)$, it can be seen clearly that $\hat{B}_n(\cdot) = B_n(\cdot)$ and then $(\text{A-}37)$ reduces to the well-known result in [62, eq. 1.17.E13].